Thermal Emission Control with Periodic Microstructures

A THESIS
SUBMITTED TO THE FACULTY OF THE GRADUATE SCHOOL
OF THE UNIVERSITY OF MINNESOTA
BY

Sang Eon Han

IN PARTIAL FULFILLMENT OF THE REQUIREMENTS
FOR THE DEGREE OF
DOCTOR OF PHILOSOPHY

February, 2009

Thermal Emission Control with Periodic Microstructures

by Sang Eon Han

ABSTRACT

In this thesis, the control of thermal emission with periodic microstructures is investigated. An important class of these structures, known as photonic crystals, are considered and Kirchhoff's law for photonic crystal films is discussed. Using fluctuational electrodynamics and a Green's function formalism, it is proved that Kirchhoff's law is obeyed for any photonic crystal films. This formalism allows the calculation of optical coherence for periodic structures. Moreover, a generalized form of Kirchhoff's law is derived for non-uniform temperatures. Using this, the control of thermal emission by selective heating of periodic structures is explored. It is found that local periodic heating allows control over which peaks appear in the thermal emission spectrum. The modification of thermal emission using a self-assembled metallic photonic crystal called inverse opal is also discussed. Despite its simplicity in fabrication, strong absorption in inverse opals prevents any influence of the periodicity. The origin of this effect is considered and it is shown how to tailor both the absorption and the surface coupling in experimentally realizable metallic inverse opals. The results show that the optical properties of tailored tungsten inverse opals can be similar to the tungsten woodpile, where modified thermal emission is already seen. In addition to these structures, structured metal surfaces, which are even easier to fabricate, are discussed. In particular, thermal emission from the surfaces of metal films that are patterned with a series of circular concentric grooves (a bull's eye pattern) is examined. Due to thermal excitation of surface polaritons, theory predicts that a single beam of light can be emitted from these films in the normal direction that is amazingly narrow, both in terms of its spectrum and its angular divergence. Experiments of tungsten bull's eyes verify this effect in the infrared. This shows that metallic films can generate laser-like beams of infrared light by a simple thermal process.

Acknowledgements

I am greatly indebted to many people who have supported me in various ways over the last five years. It is a delight to acknowledge those who have helped me during the course of this degree.

I wish to express my greatest appreciation and thanks to my thesis advisor, David Norris, whose encouragement, guidance, and thoughtful insight have always been invaluable. I have very much enjoyed working on the problems discussed in this thesis, which would not have been possible if he as an experimentalist had not recognized my theoretical orientation and guided me in that direction. He challenged and sharpened my understanding with his views at various perspectives. His support has not been limited to research. He also taught me writing and presentation skills. All the papers were written only after long discussions about an effective and clear presentation of the flow of thoughts, from which I learned a lot.

I would also like to particularly thank Andreas Stein for the discussions during the regular meetings which broadened my scientific horizon. Discussions during the meetings with Prashant Nagpal, Nick Denny, and Won Cheol Yoo were helpful and raised experimental challenges that were not dealt with in my theoretical work. I also thank my former group members, Yoonho Jun, Hong Wei, Sangjin Han, and Linli Meng, for discussions about the fabrication and characterization of inverse opals. With their help,

I was able to do some experiments. In particular, Yoonho, as a dad of twins, has been a good counselor and helper in various important areas such as "bottle-feeding twin babies at the same time." I also enjoyed having lunch with my current members, Andy Wills, Moon Sung Kang, Prashant Nagpal, Kurtis Leschkies, Lejun Qi, and Ayash Sahu, but I would courteously refuse Andy's marshmallow shots.

I am deeply indebted to my previous advisor in my Master's course, Seung Jong Lee, without whom I would not be what I am today. He has been an invaluable mentor for me and I learned a lot of scientific knowledge and computational techniques from him. I also thank Gang Chen, who will be my postdoctoral advisor, for encouraging me to publish Chapter 2 of this thesis.

This work was supported by the US Department of Energy and used resources at the University of Minnesota Supercomputing Institute. I also thank Samsung Scholarship Foundation for financial support for 4 years.

My dearest wife, Ji Hyun, deserves special mention for all her love and support, the thought of which is always a joy. Leaving her parents and friends behind and standing by me, she has endured lots of hardships in this foreign country. I thank my little twin kids, Johanna and Joseph, for giving me five. I also thank my best friend, Sun Wook, for his encouragement. Finally, my love and gratitude go to my mother who loved me so much throughout my life.

Dedication

To
Ji Hyun, Johanna, and Joseph

Contents

List of Tables

List of Figures

Chapter 1

Introduction

"Reason must take the lead with principles for its judgments according to constant laws and compel nature to answer its questions."

Immanuel Kant

Energy efficiency is an important engineering issue in the design of devices. In certain devices which work with thermal emission, the frequency of radiation needs to be optimized to increase the energy efficiency. For example, incandescent light bulbs utilize the thermal radiation of visible wavelengths from a heated tungsten filament. However, typical light bulbs radiate only around 12% of the light into the visible range [1]. If the filament is designed to enhance the emission of visible light and suppress the other frequencies, the efficiency of the light bulb can be increased. This is an example where the frequency of thermal emission needs to be optimized. In other devices, both the frequency and the direction of thermal emission needs to be optimized. For example, thermophotovoltaic systems convert thermal energy into electrical energy. Heat in the form of solar radiation or industrial waste heat is used to increase the temperature of an object. Then the thermal emission from this object is directed onto a photovoltaic

cell and converted into electricity. Typically, the photocell is a semiconductor p-n junction that has an electronic energy gap. Thus, only the frequencies of thermal emission well-matched to the energy gap are efficiently converted into electricity. Consequently, although this process has been discussed for many decades, the energy efficiency of these systems has been limited by the emission properties of the heated object. If the thermal emission spectrum could be engineered, the efficiency could be increased. In addition, the thermal emission needs to be directed to hit the photovoltaic cell. Because the photovoltaic cell must remain at room temperature, it must be separated from the hot emitting object. Therefore, the directional control of thermal emission is also important in thermophotovoltaics. In this thesis, with these problems in mind, we wish to control the thermal emission by engineering the structure of the radiating material on an optical length scale. In particular, we explore the possible solutions to control the frequency and the direction of thermal emission using microstructured materials called photonic crystals.

1.1 Photonic Crystals

1.1.1 Definition and Applications

Photonic crystals are solids that are periodically structured on a micrometer length scale. The idea of photonic crystals originally came from an analogy to atomic crystals [2]. Just as electronic band structures can have electronic bandgaps due to the periodicity of the potential, photonic crystals can also have photonic bandgaps due to periodically placed dielectric materials. These photonic bandgaps, which are frequency regions where photons cannot exist in the photonic crystal, open due to the diffraction of the electromagnetic waves. For this, the length scale of the periodicity must be of the order of the optical wavelength, which typically is in the visible or the infrared range. For the realization of a photonic bandgap, which is omnidirectional by definition, photons should not propagate in any directions. This requires three-dimensional

periodicity of dielectric functions. Accordingly, photonic crystals were defined initially as a solid that is three-dimensionally patterned. However, even though one- and two-dimensional periodic structures do not have omnidirectional bandgaps, they also lead to optical diffraction and have demonstrated a variety of interesting physics and applications. Therefore, the definition of photonic crystals was expanded to include structures that are periodic in one- and two-dimensions [3, 4]. In this thesis, we will use this more general definition of photonic crystals.

The ability of photonic crystals to control light propagation finds various applications in optical devices. If a point defect is present inside a photonic crystal, the light within the bandgap frequencies can be trapped at the defect site [3, 4, 5, 6, 7]. Such a defect serves as a resonant cavity which is an important component of laser systems. If a line defect is created inside the structure, light is guided along the line defect. Thus, a waveguide can be fabricated using photonic crystals with a line defect. The photonic crystal waveguides can be used in optoelectronic circuits especially when sharp bends are present. By using materials with negligible optical losses, photonic crystals can also be used as optical fibers in telecommunications.

These interesting applications utilize the response of photonic crystals to externally supplied light. Photonic crystals may also be used as a light generator with interesting optical properties. Cornelius *et al.* proposed on theoretical grounds that the blackbody radiation spectrum can be dramatically modified by exploiting photonic bandgaps [7]. This modification of the radiation spectrum was demonstrated subsequently by experiments [8, 9, 10, 11]. This suggests that photonic crystals may be useful for various applications where thermal emission is utilized, such as incandescent light bulbs [12] and thermophotovoltaic devices [9, 13]. In incandescent light bulbs, photonic crystals could suppress the emission of wavelengths outside the visible range, which lead to energy inefficiencies. In thermophotovoltaic systems, the emission wavelength could be matched to the photovoltaic cell to minimize energy losses. A nearly monochromatic thermal emission could also be achieved by using electromagnetic modes at the surfaces

of photonic crystals [14].

For photonic bandgaps, the size of the photonic crystals should be much larger than the structural periodicity. They should also have negligible absorption in the frequency range of interest. Otherwise, the photons will be absorbed before they interact with the long range periodicity in structure. Indeed, in many cases, photonic crystals employ dielectric or semiconductor materials that exhibit low absorption. However, metals which absorb light more strongly have also been used for photonic crystals. The interaction of light with metallic photonic crystals is quite different than dielectric photonic crystals. Thus, in the following, we will describe the optical properties of dielectric [Section 1.1.2] and metallic [Section 1.1.3] photonic crystals separately.

1.1.2 Basic Theory

Dielectric Photonic Crystals

By dielectric materials, we mean materials whose dielectric function is nearly a real and positive constant over the frequency range of interest. The dielectric function is a fundamental macroscopic quantity that describes the electromagnetic response of a nonmagnetic material. It is determined by the response of the electrons to the electric field. When the electrons oscillate in phase with the electric field, the dielectric function takes a large positive or a large negative value. Near the resonance frequency, the kinetic energy of the electrons is dissipated. This leads to finite imaginary part in the dielectric function. On the other hand, far from the resonance, the dielectric function assumes a modest value which, in general, is a positive constant over a wide range of frequencies. This is the case with a dielectric material. Because the frequency is far from the resonance, dielectric materials show negligible absorption and this is represented by an extremely small value of the imaginary part of the dielectric function.

Dielectric photonic crystals consists of a periodic arrangement of dielectric materials. When light is incident on the photonic crystal, the light is scattered at every

interface between materials with different dielectric functions. The scattering from periodic structures is called *Bragg-like multiple scattering* [15, 16]. It is a special kind of *optical diffraction* occurring in periodic structures. Due to the wave nature of light, the scattered light interferes both with itself and with the incident wave. The periodicity of the dielectric function generates various interference patterns depending on the optical frequency. Thus, the light inside the photonic crystal has a well defined wavevector called the *Bloch wavevector*. The state of photons in periodic structures can be described by the wavevector, the frequency, and the polarization. The relation between the frequency and the wavevector is called the *dispersion relation*. The dispersion relation for a photonic crystal can be obtained by solving Maxwell's equations for a structure with a periodic dielectric function. Because of the periodicity of the dielectric function, photonic crystals have a discrete translational symmetry and satisfy the *Bloch theorem* [3, 15, 16]. The Bloch theorem states that the solution of Maxwell's equations for photonic crystals can be expressed by a function with the crystal periodicity multiplied by a plane wave phase factor:

$$\boldsymbol{\psi_k}(\boldsymbol{r}) = \boldsymbol{u_k}(\boldsymbol{r})\exp(i\boldsymbol{k}\cdot\boldsymbol{r}), \tag{1.1}$$

where $\boldsymbol{\psi_k}(\boldsymbol{r})$ represents an electric or magnetic field vector with wavevector $\boldsymbol{k}$ at the position $\boldsymbol{r}$ and $\boldsymbol{u_k}(\boldsymbol{r})$ is a periodic vector function with the periodicity of the lattice vector $\boldsymbol{R}$ of the photonic crystal, *i.e.*

$$\boldsymbol{u_k}(\boldsymbol{r}) = \boldsymbol{u_k}(\boldsymbol{r}+\boldsymbol{R}). \tag{1.2}$$

In Eqs. (1.1) and (1.2), the frequency dependence of the functions $\boldsymbol{\psi_k}$ and $\boldsymbol{u_k}$ is suppressed. The Bloch theorem can be expressed in an alternative form by combining Eqs. (1.1) and (1.2) as

$$\boldsymbol{\psi_k}(\boldsymbol{r}+\boldsymbol{R}) = \boldsymbol{\psi_k}(\boldsymbol{r})\exp(i\boldsymbol{k}\cdot\boldsymbol{R}). \tag{1.3}$$

In solid state physics, the wavevectors $\boldsymbol{G}$ which satisfy

$$\exp(i\boldsymbol{G}\cdot\boldsymbol{R}) = 1 \tag{1.4}$$

are called the *reciprocal lattice vectors*. From Eq. (1.4), it follows that the $\boldsymbol{G}$ is an integer multiple of a vector:

$$\boldsymbol{G} = n\boldsymbol{g}, \tag{1.5}$$

where n's are positive integers and $\boldsymbol{g}$ is chosen as the smallest of $\boldsymbol{G}$'s. The range in the wavevector space bounded by $\boldsymbol{g}$ is called the *first Brillouin zone* (BZ) and n is called the *band number*. Since any wavevector $\boldsymbol{k}' = \boldsymbol{k} + \boldsymbol{G}$ satisfies Eq. (1.3), the Bloch theorem can also be written as

$$\boldsymbol{\psi}_{n\boldsymbol{k}}(\boldsymbol{r} + \boldsymbol{R}) = \boldsymbol{\psi}_{n\boldsymbol{k}}(\boldsymbol{r})\exp(i\boldsymbol{k} \cdot \boldsymbol{R}), \tag{1.6}$$

where $\boldsymbol{k}$ is in the first Brillouin zone. Therefore, the Bloch function $\boldsymbol{\psi}_{n\boldsymbol{k}}$ is periodic in the wavevector space with periodicity $\boldsymbol{g}$ for a given band n. Accordingly, the frequency $\omega_{n\boldsymbol{k}}$ corresponding to the wavefunction $\boldsymbol{\psi}_{n\boldsymbol{k}}$ is also periodic in $\boldsymbol{k}$. For convenience, the dispersion relation for photonic crystals can be restricted to the first Brillouin zone and this construction is called the *reduced zone scheme*. The dispersion relation contains the information on the photon states that can exist in the photonic crystal and this information is called the *photonic band structure*. In Bragg-like multiple scattering, a certain frequency range of light can undergo destructive interference for all directions. This range is called the *photonic bandgap*. Because all crystal structures are be anisotropic, the dispersion relation will depend on the direction. Some frequencies will destructively interfere only in certain directions. In this case, the frequency span is called the *photonic stop gap*. When light impinges on the lossless photonic crystal in a direction where the stop gap is open, it will be totally reflected because there are no electromagnetic modes inside the structure. In general, the size of the photonic gaps increases as the dielectric contrast at the interfaces increases. As a note, the photonic band structure does not account for any surface effect because it assumes an infinite, lossless structure.

An important parameter that can be extracted from photonic band structure is the photonic *density of states* (DOS). The photonic DOS, $\rho(\omega)$, is the number of electromagnetic modes per unit frequency and unit volume and can be expressed mathematically

as [16, 17, 18]

$$\begin{aligned}\rho(\omega) &= \frac{1}{V}\sum_{n\boldsymbol{k}}\delta(\omega-\omega_{n\boldsymbol{k}}) \\ &= \frac{1}{(2\pi)^3}\sum_{n}\int_{BZ} d\boldsymbol{k}\delta(\omega-\omega_{n\boldsymbol{k}}),\end{aligned} \tag{1.7}$$

where V is the photonic crystal volume, ω the frequency, and $\omega_{n\boldsymbol{k}}$ the frequency of n^{th} photonic band with wavevector $\boldsymbol{k}$ in the first BZ. From this definition, the DOS in vacuum can be easily obtained as

$$\begin{aligned}\rho_{vac}(\omega) &= 2\times\frac{1}{(2\pi)^3}\frac{4\pi k^2}{d\omega/dk} \\ &= \frac{\omega^2}{\pi^2 c^3},\end{aligned} \tag{1.8}$$

where c is the light velocity in vacuum and the factor of 2 accounts for the two polarizations of the electromagnetic wave [15, 16, 17, 19, 20]. Thus, the photonic DOS in vacuum is a smooth function. The DOS for a photonic crystal is strikingly different. For example, the DOS is zero in the frequency range of the bandgap where no modes exist. In wavevector space, a constant frequency surface can be drawn for a photonic crystal. Let $S_n(\omega)$ be the portion of the isofrequency surface $\omega_{n\boldsymbol{k}}=\omega$ within the first BZ. Then the photonic DOS can be expressed as

$$\rho(\omega)=\frac{1}{(2\pi)^3}\sum_{n}\int_{S_n(\omega)}\frac{dS}{d\omega_{n\boldsymbol{k}}/d\boldsymbol{k}}. \tag{1.9}$$

Here $d\omega_{n\boldsymbol{k}}/d\boldsymbol{k}$ is called the *group velocity*. Physically, the group velocity is the velocity with which the electromagnetic energy moves. The group velocity can be defined only when the absorption is negligible as in the case with the photonic band structure. With significant dissipation, the velocity of energy could not rationally be defined. For any photonic crystal, there should be a region in wavevector space where the group velocity vanishes because $\omega_{n\boldsymbol{k}}$ is a periodic function of $\boldsymbol{k}$ as implied in Eq. (1.6). This will be observed for every band n because $\omega_{n\boldsymbol{k}}$ is periodic for every n. When the group velocity vanishes, the DOS becomes very large according to Eq. (1.9). This can happen for

any wavevector but, typically, the group velocity vanishes at the first BZ boundaries. In this case, the light is a standing wave and its interaction with the material will be maximized. Even with slight absorption, the photon life time can be very small. Then the light wave cannot have a definite frequency, which is the Fourier transform of the life time. Accordingly, a finite DOS is created in the bandgap. Thus, reflection or transmission spectra smoothen or broaden near the first BZ boundary if absorption is present. This behavior of line broadening in the spectrum can be an important issue for thermal emission when the photonic bands become flat, *i.e.* the frequency $\omega_{n\boldsymbol{k}}$ does not change much with the wavevector $\boldsymbol{k}$.

Metallic Photonic Crystals

(a) Uniform metal The optical properties of metallic photonic crystals are quite different from those of dielectric photonic crystals because of the strong dependence of the metallic dielectric function on the frequency. The dielectric function of a metal, $\varepsilon(\omega)$, can be approximated by the Drude model [16] as

$$\varepsilon(\omega) = 1 + \frac{i\sigma(\omega)}{\varepsilon_0 \omega}, \tag{1.10}$$

where ε_0 is the permittivity of free space and the frequency dependent electrical conductivity $\sigma(\omega)$ is given by

$$\sigma(\omega) = \frac{\sigma_0}{1 - i\omega\tau_e} \tag{1.11}$$

with the DC conductivity σ_0 expressed by

$$\sigma_0 = \frac{Ne^2\tau_e}{m}. \tag{1.12}$$

Here, τ_e is the electron relaxation time, N the electron number concentration, e the charge of an electron, and m the mass of an electron. Substituting Eq. (1.11) into Eq. (1.10) and using Eq. (1.12), we have

$$\varepsilon(\omega) = 1 - \frac{\omega_p^2}{\omega(\omega + i\gamma_e)}, \tag{1.13}$$

where $\gamma_e (= 1/\tau_e)$ is the electron collision frequency representing the dissipation of energy and the *plasma frequency* ω_p is given by

$$\omega_p^2 = \frac{Ne^2}{\varepsilon_0 m}. \tag{1.14}$$

The plasma frequency is the frequency at which the dielectric function becomes zero for a lossless metal as can be seen in Eq. (1.13). At this frequency, the polarization field becomes exactly out of phase with the electric field. Far below the plasma frequency, the real part of the dielectric function becomes large negative. An ideal metal with $\varepsilon = -\infty$ is called the perfect metal. Perfect metals are dispersionless and have no absorption. Usually, γ_e of a real metal is of the order of 1% of ω_p [12, 21]. Figure 1.1 shows the frequency dependence of the dielectric function given by Eq. (1.13). It is convenient to scale the frequencies by ω_p and define dimensionless variables:

$$\begin{aligned} \Omega &\equiv \frac{\omega}{\omega_p} \\ K &\equiv \frac{ck}{\omega_p} \\ \Gamma_e &\equiv \frac{\gamma_e}{\omega_p}. \end{aligned} \tag{1.15}$$

For a uniform, isotropic material, the dispersion relation is given by

$$\Omega = \frac{K}{\sqrt{\varepsilon(\omega)}}. \tag{1.16}$$

The dispersion relation for a uniform metal with negligible γ_e is obtained by substituting the dimensionless form of Eq. (1.13) with $\gamma_e = 0$ into Eq. (1.16) as

$$\Omega = \sqrt{1 + K^2}. \tag{1.17}$$

Equation (1.17) shows that there are no photon states below the plasma frequency. It is interesting to compare the dispersion relation with the absorptance spectrum. The *absorptance* or *absorptivity* A is the fraction of absorbed power for a unit incident light.

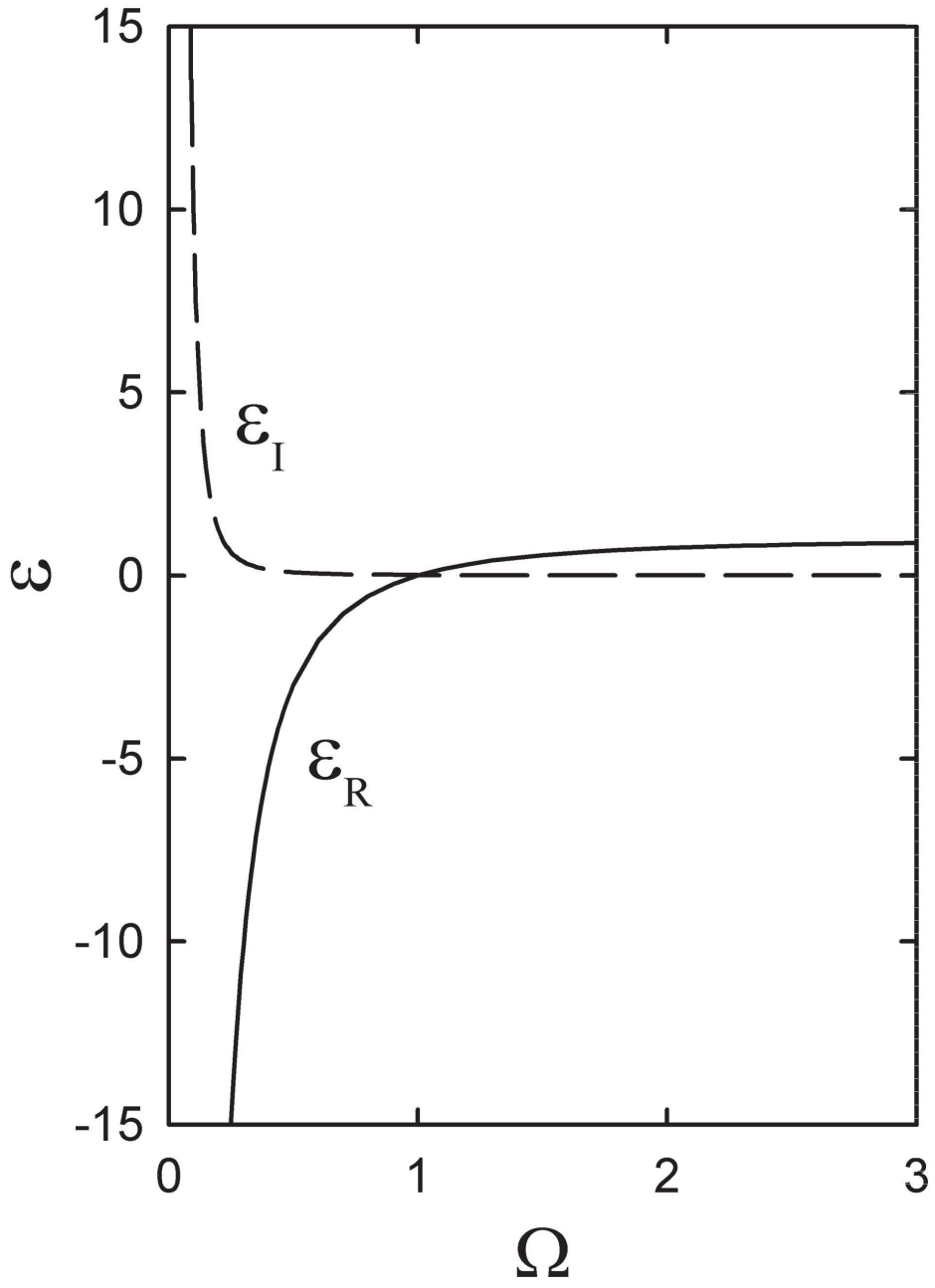

Figure 1.1: Frequency dependence of the dielectric function of a Drude metal with $\Gamma_e = 0.01$. Ω and Γ_e are defined in Eq. (1.15). The real and the imaginary part of the dielectric function is denoted as ε_R (solid line) and ε_I (dashed line), respectively.

The absorptance is an important parameter for thermal emission study as will be described in section 1.2.2. When a uniform material is thick enough that the transmission is negligible, the absorptance is given by

$$A = 1 - \left| \frac{\sqrt{\varepsilon} - 1}{\sqrt{\varepsilon} + 1} \right|^2 . \tag{1.18}$$

For a metal with small γ_e, the absorptance is obtained by substituting Eq. (1.13) into Eq. (1.18) with $\gamma_e = 0$ and using the dimensionless variables as

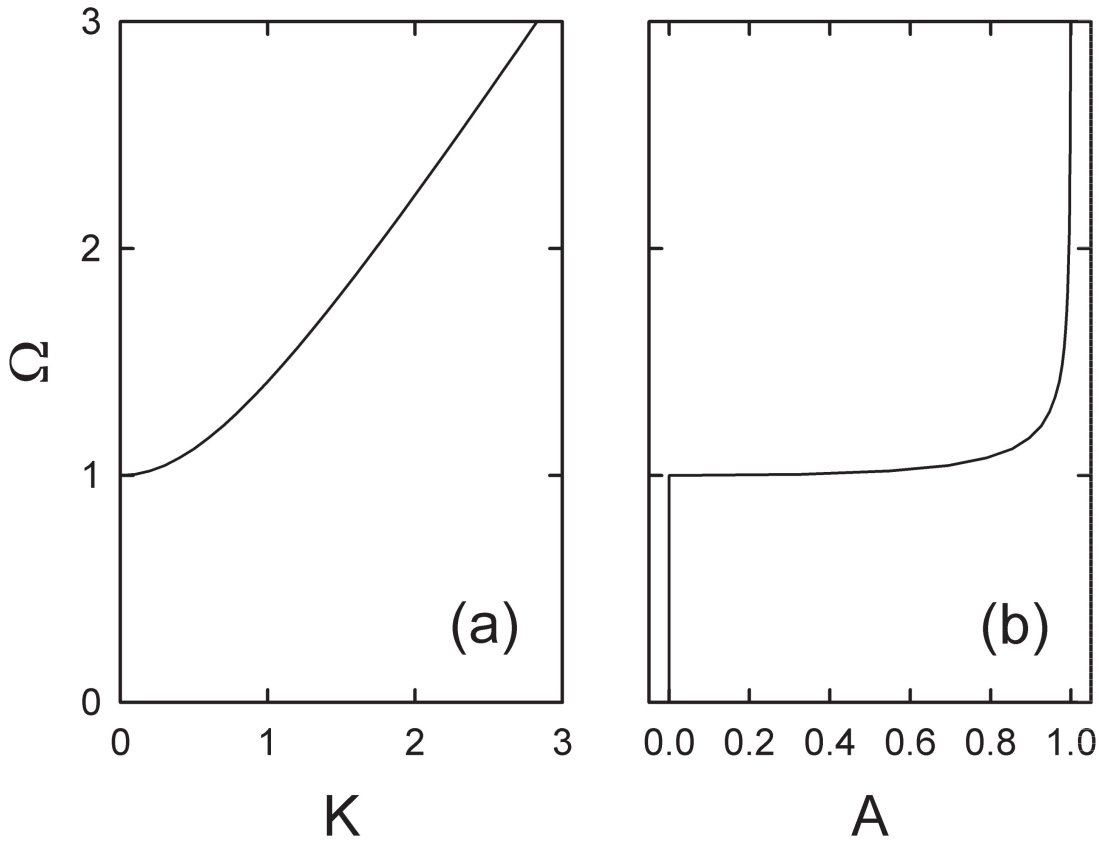

Figure 1.2: (a) Dispersion relation and (b) absorptance spectrum for a Drude metal with low loss.

$$A = 1 - \left| \frac{\sqrt{1 - 1/\Omega^2} - 1}{\sqrt{1 - 1/\Omega^2} + 1} \right|^2 . \tag{1.19}$$

Figure 1.2 compares the dispersion relation Eq. (1.17) and the absorptance spectrum Eq. (1.19) for small γ_e. The light of frequency below ω_p incident on a uniform metal is strongly reflected and the absorptance is negligible. This is because there are no photon states below ω_p. However the absorptance increases sharply above ω_p due to the coupling of the light to the photon states. The absorptance is almost 1 when the frequency is well above ω_p because the metal is semi-infinite and the reflection is negligible. When $\omega \gg \gamma_e$, Eq. (1.13) becomes

$$\begin{aligned} \varepsilon &= \varepsilon_R + i\varepsilon_I \\ &= 1 - \frac{1}{\Omega^2} + i\frac{\Gamma_e}{\Omega^3} \end{aligned} \tag{1.20}$$

using the dimensionless variables. Substituting Eq. (1.20) into Eq. (1.16) and using $\Omega = \Omega_R + i\Omega_I$, we obtain

$$\begin{aligned} \Omega_R &= \sqrt{1+K^2} \\ \Omega_I &= -\frac{\Gamma_e}{2\Omega_R^2} \quad \text{if } \Omega_R \gg |\Omega_I|. \end{aligned} \tag{1.21}$$

Equation (1.21) determines the dispersion relation for complex frequency space. The photon life time τ defined by [22]

$$\tau \equiv -\frac{1}{2\omega_I} \tag{1.22}$$

is obtained for a Drude metal from Eq. (1.15) and (1.21) as

$$\tau = \frac{\Omega_R^2}{\gamma_e} \quad \text{if } \Omega_R \gg |\Omega_I|. \tag{1.23}$$

Figure 1.3(a) shows the relation between the photon life time and the frequency in the dimensionless forms. The photon life time is the smallest at the plasma frequency ω_p. Therefore, the spectrum will be smoother at the band edge if absorption is present. This has an implication that photonic crystals behave similarly. Specifically, it is a general behavior observed in photonic crystals with absorption that the spectrum will be smoothened out strongly near the band edges due to the small life time of photons.

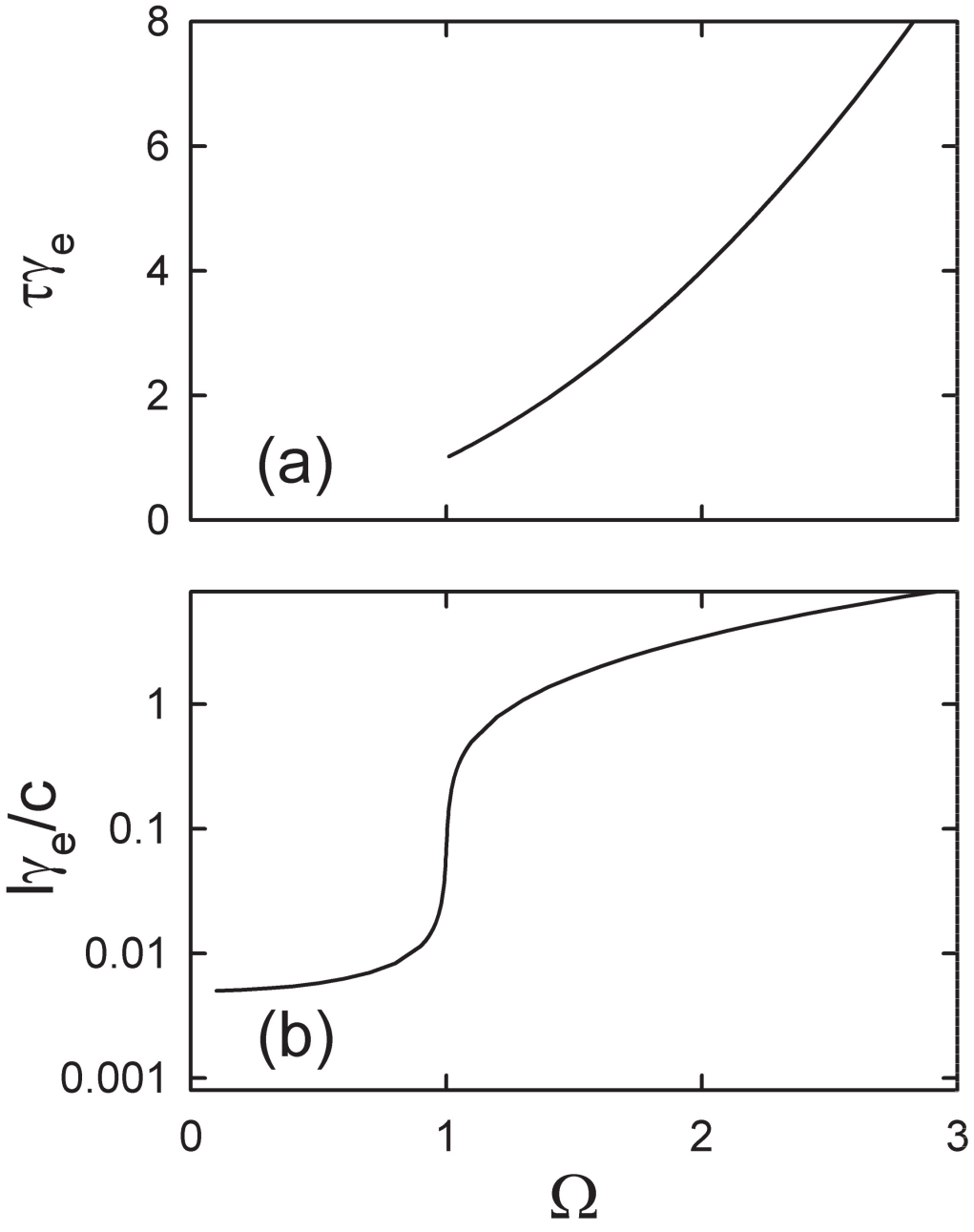

Figure 1.3: (a) Photon life time and (b) spatial decay length as a function of frequency for a Drude metal with low loss.

Instead of using the complex frequency, we can also use the complex wavevector $K = K_R + iK_I$. Using Eq. (1.16) and (1.20), the dispersion relation is obtained for the complex wavevector as

$$\begin{aligned} K_R &= \Omega\sqrt{\frac{\varepsilon_R + \sqrt{\varepsilon_R^2 + \varepsilon_I^2}}{2}} \\ K_I &= \Omega\sqrt{\frac{-\varepsilon_R + \sqrt{\varepsilon_R^2 + \varepsilon_I^2}}{2}}. \end{aligned} \tag{1.24}$$

The spacial decay length l defined by [22]

$$l \equiv \frac{1}{2k_I} \tag{1.25}$$

becomes, for a Drude metal,

$$l = \frac{c}{\gamma_e}\Omega^2\sqrt{\frac{\varepsilon_R + \sqrt{\varepsilon_R^2 + \varepsilon_I^2}}{2}}. \tag{1.26}$$

As the frequency approaches ω_p from the high frequency side, the spatial decay length l decreases and the decrease is faster very near ω_p, as shown in Fig. 1.3(b). Therefore, the absorptance will be high near ω_p even for a thin film. In Fig. 1.3(b), l becomes very small below the plasma frequency. In this case, l is called the *skin depth* of the metal. When the absorption is small and $\varepsilon_R \gg \varepsilon_I$, we have $K_I \simeq \Gamma_e/2K_R\Omega$ from Eq. (1.24) and an interesting relation between ω_I and k_I can be obtained from Eq. (1.21) as

$$\omega_I = -\frac{c^2 k}{\omega} k_I. \tag{1.27}$$

Because, from Eq. (1.15) and (1.17), the group velocity $v_g \equiv d\omega/dk$ equals c^2k/ω, Eq. (1.27) can be written as

$$\omega_I = -v_g k_I. \tag{1.28}$$

This relation can be generalized for photonic crystals as [23]

$$\omega_I = -\boldsymbol{v}_g \cdot \boldsymbol{k}_I. \tag{1.29}$$

The manipulation of light via photonic crystals is usually done by the Bragg-like multiple scattering, as we have seen in the discussion of dielectric photonic crystals. However, metallic photonic crystals can exhibit interesting and useful behaviors even without the Bragg-like multiple scattering if certain conditions are satisfied. This can be expected when the wavelength λ is much longer than the lattice constant a of the photonic crystal. In the following, we will discuss this case before addressing the Bragg-like multiple scattering in metallic photonic crystals, which happens when λ is comparable to a.

(b) Effective Medium Theory ($\lambda \gg a$): We have discussed that the dielectric function determines the optical response of a material. The dielectric function is a macroscopic quantity. The material is regarded as homogeneous when the wavelength is much larger than the atomic distances. In the same way, the optical response of a photonic crystal will be determined by a macroscopic quantity if the wavelength is much larger than the lattice parameter. This quantity is called the effective dielectric function which is determined by the effective medium theory. In the limit of long wavelength, the Bragg-like multiple scattering becomes negligible.

Pendry *et al.* developed an effective medium theory for a specific metallic photonic crystal called the wire mesh [24, 25, 26, 27, 28]. This structure is a simple cubic array of wires in three dimensions as shown in Fig. 1.4. The theory predicts that the effective dielectric function for this structure becomes

$$\varepsilon_{eff}(\omega) = 1 - \frac{\omega_{p,eff}^2}{\omega(\omega + i\gamma_{e,eff})}. \tag{1.30}$$

Here the effective electron collision frequency $\gamma_{e,eff}$ is the inverse of the effective electron relaxation time $\tau_{e,eff}$ given by

$$\tau_{e,eff} = \tau_e + \sigma_0 SL, \tag{1.31}$$

where S is the cross-sectional area of the wires and L is the self inductance per unit

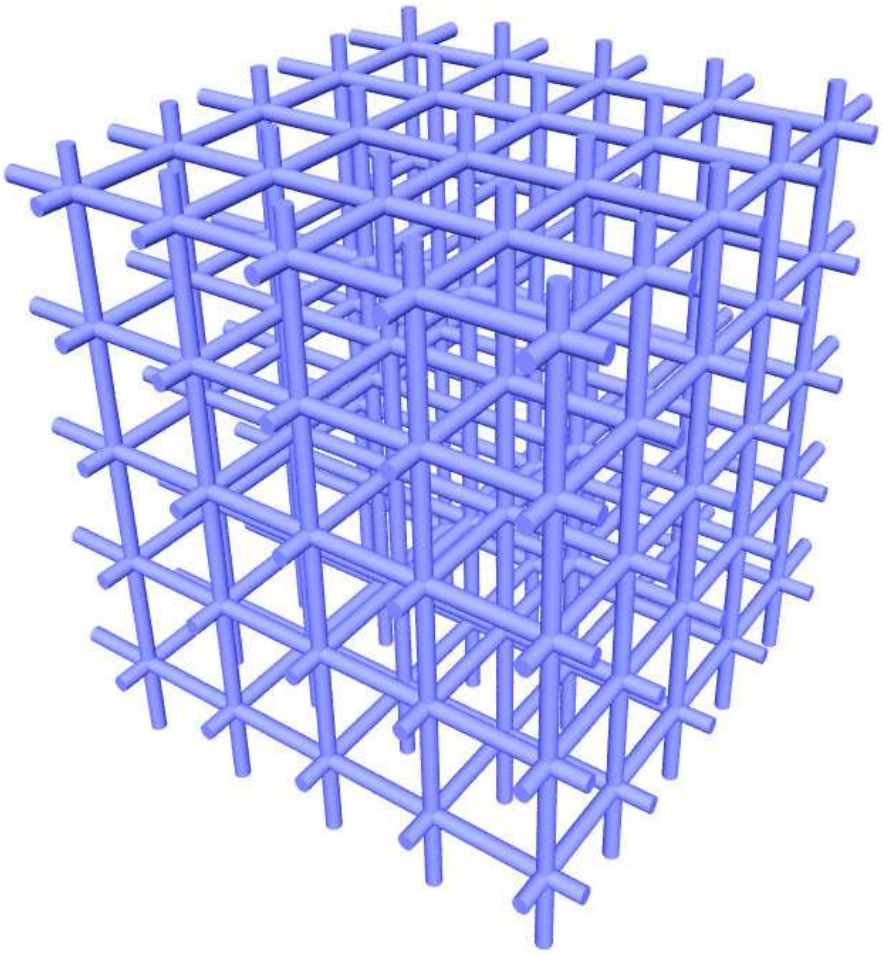

Figure 1.4: A simple cubic wire mesh structure.

length of the wire. The effective plasma frequency $\omega_{p,eff}$ in Eq. (1.30) is expressed by

$$\omega_{p,eff}^2 = f\frac{\tau_e}{\tau_{e,eff}}\omega_p^2, \tag{1.32}$$

where f is the filling fraction of the metal wires. Using Eq. (1.14), (1.31), and (1.32), $\omega_{p,eff}$ can be written as

$$\omega_{p,eff}^2 = \frac{N_{eff}e^2}{\varepsilon_0 m_{eff}}, \tag{1.33}$$

where the effective electron density N_{eff} is

$$N_{eff} = fN \tag{1.34}$$

and the effective electron mass m_{eff} is

$$m_{eff} = (1 + \sigma_0 SL/\tau_e)m. \tag{1.35}$$

Using Eq. (1.31), $\gamma_{e,eff}$ can also be expressed as

$$\gamma_{e,eff} = \frac{\gamma_e}{1 + \sigma_0 SL/\tau_e}. \tag{1.36}$$

Remarkably, Eq. (1.30) assumes the same form as Eq. (1.13) with the exception that ω_p and γ_e are replaced by $\omega_{p,eff}$ and $\gamma_{e,eff}$, respectively. This reveals that the optical response of the wire mesh is the same as a homogeneous metal but with a different plasma frequency and a different damping frequency. Because the plasma frequency is the only parameter that determines the optical properties of a homogeneous metal with negligible damping, it is useful to look at the form of the effective plasma frequency of the wire mesh. Comparison of Eqs. (1.14) and (1.33) together with Eqs. (1.34) and (1.35) shows that the wire mesh has the electron density diluted by the metal filling fraction and the electron mass increased by the self inductance. The electron collision frequency of the homogeneous metal is also reduced by the self inductance. Note that the metal filling fraction and the self inductance are purely determined by the geometry of the structure. A rough estimate of $\omega_{p,eff}$ is possible if the self inductance can be neglected. In this case, it follows from Eq. (1.32) that

$$\omega_{p,eff} \simeq \sqrt{f}\omega_p. \tag{1.37}$$

Eq. (1.37) is the consequence of averaging the dielectric function with the filling fraction as a weighting factor [29], *i.e.*

$$\varepsilon_{eff} \simeq (1 - f) + f\varepsilon, \tag{1.38}$$

as can be seen from Eqs. (1.13) and (1.30) when damping is negligible.

The basic principles explained above can be applied to other metallic photonic crystals as long as the structures are interconnected so that the self inductance is finite.

When the structures are disconnected, the capacitance plays a role at disconnected regions and a positive effective dielectric function is obtained at low frequencies. Thus the optical properties of metallic photonic crystals can be controlled by structural modifications when the wavelength is much larger than the lattice constant. When the absorption is weak, the dispersion relation can be established for metallic photonic crystals. Because the optical properties can be represented by Eq. (1.30) in the limit of long wavelength, the dispersion relation takes the same form as Eq. (1.17). In this case, no possible solutions exist below $\omega_{p,eff}$ and this frequency region is called the *metallicity gap* [30]. Note that the metallicity gap has nothing to do with Bragg-like multiple scattering and is only possible for connected structures. The metallicity gap has important implications for thermal emission modification. Absorptance in the metallicity gap is small. Because absorptance is equal to emissivity as will be explained in section 1.2, thermal emission in the metallicity gap is small. It means that low frequency emission is always suppressed when a connected metallic structure is heated. Moreover, the region of emission suppression can be controlled by shifting $\omega_{p,eff}$ by using the appropriate structures.

(c) Bragg-like multiple scattering ($\lambda \sim a$): Reflection of light at a surface increases as the dielectric contrast between the material and the surrounding medium (*e.g.* air) increases. The Bragg-like multiple scattering effect in photonic crystals will in general be strong if the dielectric contrast at the interfaces is large. Accordingly, the size of the photonic bandgaps increases as the dielectric constant increases for dielectric photonic crystals. For metallic photonic crystals, a very large dielectric contrast is available. However, it cannot be said that photonic bandgaps are always much wider for metals than dielectric materials for a given structure. This is because the photonic band structures of dielectric photonic crystals are altered dramatically when metals are used. The dielectric function of dielectric materials typically ranges from 2 to 20 whereas metals can have a very large negative dielectric function such as -1000 or -10000. Moreover,

the dielectric function of metals depends very strongly on the frequency and the imaginary part of the dielectric function is large. Therefore, for metallic photonic crystals, the photonic band structures are very different from dielectric photonic crystals and a direct comparison of the size of the bandgap for the two crystals is not possible. For example, connected metallic photonic crystals exhibit a metallicity gap which is destroyed when the metals are replaced by dielectrics.

Nevertheless, it may be possible to use a large dielectric contrast in metals to achieve a large photonic bandgap that is difficult to be realized in dielectric photonic crystals. For example, it has been reported that a large bandgap can be formed when the dielectric function is nearly zero, which happens near the plasma frequency [31]. In this case, the dielectric contrast becomes extremely large and a wide bandgap may be possible. However, it should be noted that the absorption can be strong near the plasma frequency and the width of the bandgap in this region can be decreased.

In the context of thermal emission, creating a bandgap near $\lambda \sim a$ can be very useful [8, 9, 10, 11, 32]. In particular, when the bandgap is large enough that it extends to the $\omega_{p,eff}$ expected from Eq. (1.30), the bandgap can overlap with the metallicity gap [33]. In this case, a very large frequency gap starting from zero and extending to a cutoff frequency can be formed. This can be viewed as the extension of the metallicity gap by using the photonic bandgap. Because the origin of the two gaps is different, in the overlapping region of the two gaps the mechanism becomes fuzzy. It can only be said that the effective medium effect is working for $\lambda \gg a$ and the Bragg-like multiple scattering is responsible near $\lambda \sim a$. Because the absorptance will be very low in this gap, thermal emission will be suppressed there. This interesting case will be explored in more detail in Chapter 4.

(d) Surface plasmon polaritons (SPPs) SPP is a quantum of the coupled oscillations of the electromagnetic field and the charge density existing at the interface of two materials [34]. The electromagnetic intensity decays exponentially in both materials so

that the SPPs are confined to the surface. When the SPPs lose the electromagnetic character and carry energy almost solely in the form of charge density waves, we call them the *surface plasmons* (SPs). SPs occur typically at a specific frequency called the surface plasmon frequency whereas SPPs are possible over a range of frequencies. In general, a polariton is a quantum of a mixed excitation that is part electromagnetic oscillation and part something else [35]. For example, a surface phonon polariton is a mixed excitation of polar surface vibrations (*i.e.* phonons) and an electromagnetic wave. Even though SPs and SPPs are distinct, many authors use the term SPs to include both [36, 37]. Here we will use SPPs for coupled excitations.

SPPs are possible between a dielectric material with $\varepsilon \geq 1$ and a material with $\varepsilon < -1$. This condition can be satisfied at metal-dielectric interfaces. The electric fields of SPPs are in the plane defined by the SPP propagation direction and the surface normal. This means SPPs can couple to only p-polarized light. The wavevector k_{SPP} of SPPs on a flat metal surface is given by [36]

$$k_{SPP} = \frac{2\pi}{\lambda}\sqrt{\frac{\varepsilon}{\varepsilon+1}}, \tag{1.39}$$

where ε is the dielectric function of the metal. Eq. (1.39) shows that, for a good metal whose ε is large negative, the SPPs carry a slightly larger momentum than the light in vacuum because $k_{SPP} \gtrsim 2\pi/\lambda$. Substituting Eq. (1.13) with negligible damping into (1.39), we can obtain the dispersion relation of SPPs. This is shown in Fig. 1.5 with dimensionless variables defined in Eq. (1.15). We note three important points in the dispersion relation. First, the dispersion curve shows a plateau at $\omega = \omega_p/\sqrt{2}$ which is called the SP frequency. In this region, the electromagnetic character disappears because of the high spatial frequency. From Eq. (1.13), this SP frequency corresponds to $\varepsilon = -1$. Second, the SPPs are possible below the SP frequency. Thus SPPs can be excited only when ε is less than -1. Third, because the dispersion curve of SPPs does not cross the light line $\omega = ck$, SPPs cannot be excited on a flat surface by incident light unless a special mechanism is provided to add momentum parallel to the surface

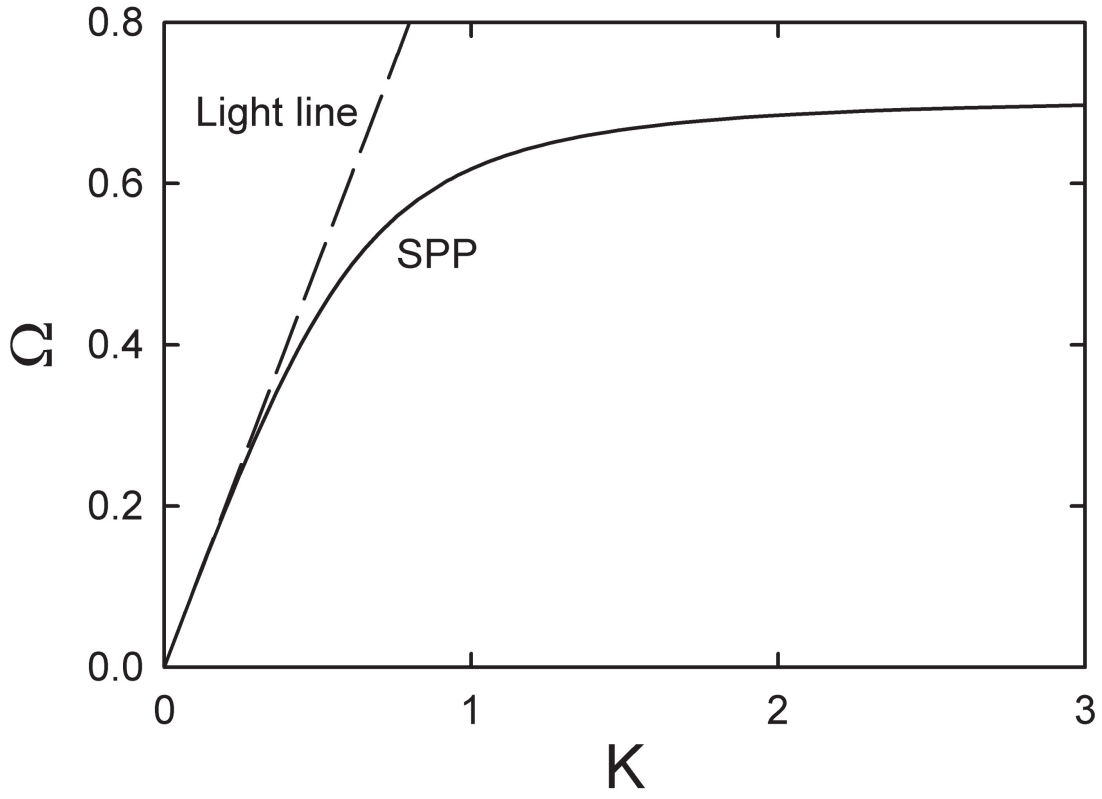

Figure 1.5: Dispersion relation of SPPs (solid line) for a flat surface of a Drude metal without loss. A light line (dashed line) given by $\Omega = K$ is shown for comparison.

to the light. The light can gain this additional momentum when the metal is ruled to generate a grating structure. Specifically, due to the periodic structure, Bloch modes are established and the dispersion relation becomes periodic in the wavevector as can be seen in Fig. 1.6 [see also the discussion following Eq. (1.6)]. The dispersion curve is periodic and can be in the region $\omega \geq ck$. In this case, the frequency, the wavevector, and the polarization of the SPPs can be the same as those of the incident light. Thus, the SPPs can couple to the light. However, it should be kept in mind that the dispersion relation is disturbed further as the surface is more strongly modulated. In other words, the grating does not just lead to Fig. 1.6 in this case. Rather, photonic gaps can form at the BZ boundaries. We also note that the dispersion relation does not give us

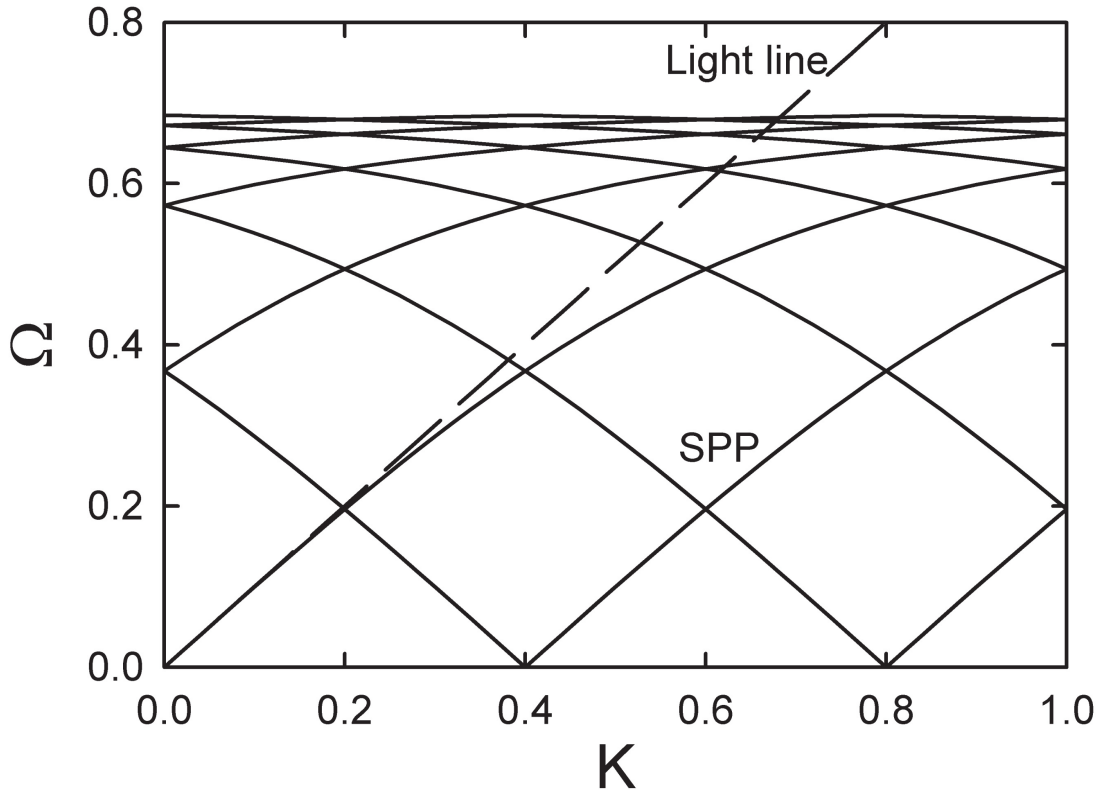

Figure 1.6: Dispersion relation of SPPs (solid line) for on a periodically structured surface of a Drude metal without loss and a light line (dashed line) given by $\Omega = K$. The surface is assumed to be modulated only slightly so that any bandgaps are not noticeable. The structural periodicity is set to $2.5\lambda_p$ where the plasma wavelength λ_p is given by $2\pi c/\omega_p$.

information about the strength of the coupling between the light and the SPPs. When light is well coupled to SPPs, it can be significantly absorbed. This means a metallic mirror that reflects light efficiently when its surface is smooth can absorb light strongly through SPPs when it is ruled appropriately. Moreover, this absorption can happen in a very narrow frequency band. The light absorption occurs because SPPs are eventually dissipated into heat by the metal. The propagation length or spatial decay length of an SPP, l_{SPP}, is defined by the distance over which the intensity of the SPP decays to $1/e$

of its original intensity as in Eq. (1.25), i.e.

$$l_{SPP} = \frac{1}{2k_{SPP,I}}, \tag{1.40}$$

where $k_{SPP,I}$ is the imaginary part of k_{SPP}. The SPP propagation length is related to the divergence angle of absorptance or emissivity as will be shown in section 1.3. The SPP life time τ_{SPP} is also defined in the same manner as Eq. (1.22). When the SPP has a long life time, the uncertainty in SPP frequency is minimal. Then the absorption spectrum can have a sharp peak. This in turn means a sharp emissivity. These properties can be used to obtain highly monochromatic thermal emission. We will discuss this in Chapter 5.

1.2 Thermal Emission

1.2.1 Planck's radiation law

The distribution function, commonly used in statistical physics, is defined as the probability distribution of states. Let n_k be the number of particles that are in the k^{th} quantum state. n_k is called the occupation number of the states. The distribution function is the average occupation number $< n_k >$ per state. If the wavefunction of the N identical particles is symmetric under exchange of any pair of particles, the particles are called bosons. The occupation numbers of the specific states of the bosons have no restriction and can take any value. The distribution function of the ideal gas of bosons is called the *Bose-Einstein distribution function* and can be expressed as [19, 20, 38]

$$< n_k >= \frac{1}{e^{(\varepsilon_k - \mu)/k_B T} - 1} \tag{1.41}$$

where k_B is the Boltzmann constant, ε_k is the energy of a particle in the k^{th} state, and μ is the chemical potential. Photons in vacuum do not exchange energy with each other at low intensity and can be regarded as an ideal gas [19, 38]. Thus photons in vacuum obey Bose-Einstein distribution. Photons must interact with matter to reach

an equilibrium state because they do not exchange energy with each other. However, in the interaction of photons with matter, photons are either absorbed or emitted but not scattered inelastically. This leads to the fluctuations in the number of photons. Because the free energy (F) is constant at equilibrium for variable number of photons (N), the chemical potential $\mu(= \partial F/\partial N)$ should be zero. Since the energy of photons ε_k is $\hbar\omega$, the distribution function of an ideal photon gas becomes

$$< n_\omega >= \frac{1}{e^{\hbar\omega/k_B T} - 1}, \tag{1.42}$$

which is the *Planck's distribution function.*

A *black-body* is defined as an ideal body which absorbs all the incident photons without any reflection. Thus the absorptance of a black-body is unity. A realizable approximation to a black-body is a small hole in the wall of an enclosure. The linear dimension of the enclosure and the hole is large compared to the wavelength of the radiation. When light is incident on the hole, it is trapped inside the enclosure and rarely escapes because the hole is much smaller than the enclosure. Thus, the hole absorbs almost all light incident on it and reasonably approximates a black-body. The spectral energy distribution in the radiation coming out through the hole will be the same as that in the enclosure. Therefore, the properties of radiation from a black-body can be obtained by considering the radiation in the enclosure. Consider the wall of the enclosure at a temperature T. The equilibrium electromagnetic radiation inside the enclosure is characterized by the same temperature T. At equilibrium, the radiation inside the enclosure is (i) uniform, (ii) isotropic, (iii) unpolarized, and (iv) independent of the geometry and material properties of the enclosure [20]. The average number of photons in vacuum per unit frequency per unit volume $N_\omega(\omega)$ is given by

$$N_\omega(\omega) = \rho_{vac}(\omega) < n_\omega >, \tag{1.43}$$

where ρ_{vac} and $< n_\omega >$ are given in Eqns. (1.8) and (1.42), respectively. Since the energy of a photon of frequency ω is $\hbar\omega$, the energy density per unit frequency $u_\omega(\omega)$ is

given by

$$u_\omega(\omega) = \hbar\omega N_\omega(\omega). \tag{1.44}$$

Substituting Eqs. (1.8) and (1.42) into Eq. (1.43), and then the resulting equation into Eq. (1.44), we obtain the energy density of black-body radiation per unit frequency as

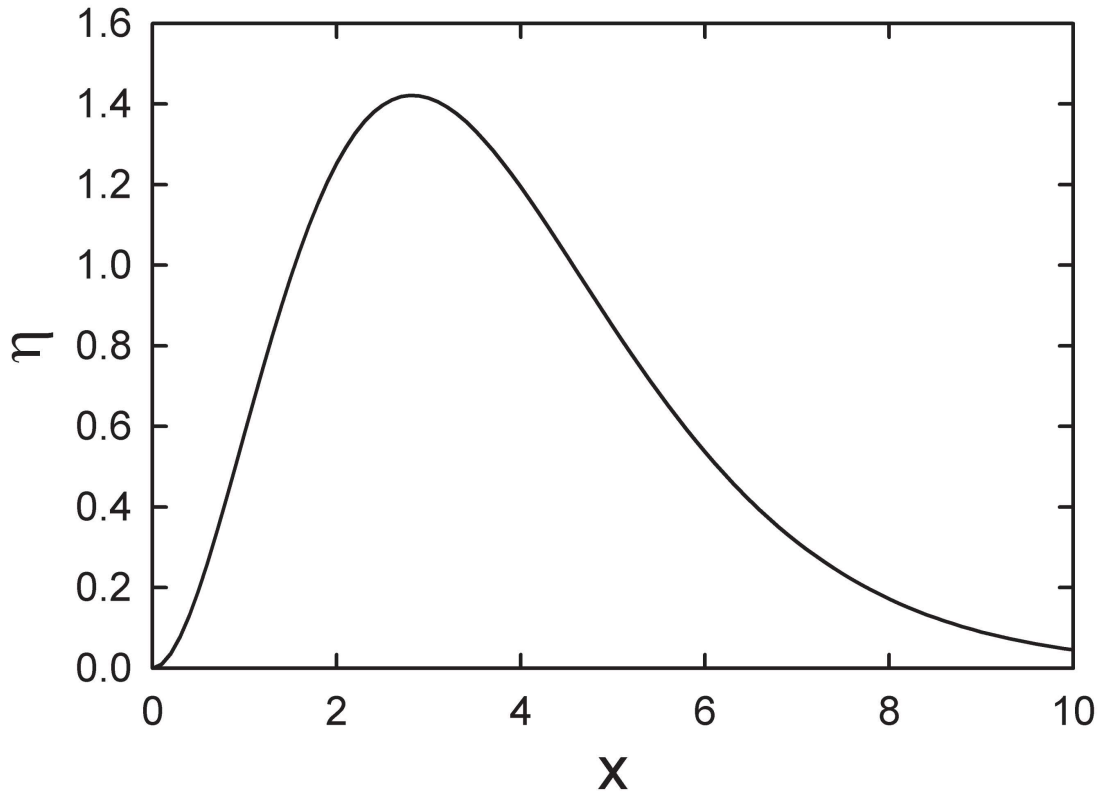

Figure 1.7: The spectral energy density of black-body radiation as a function of the dimensionless frequency $x = \hbar\omega/k_BT$.

$$u_\omega(\omega) = \frac{\hbar\omega^3}{\pi^2c^3}\frac{1}{e^{\hbar\omega/k_BT} - 1}. \tag{1.45}$$

This is the *Planck's radiation law*. Using the dimensionless frequency x and the spectral energy density $\eta(x)$ defined by

$$x = \frac{\hbar\omega}{k_BT} \tag{1.46}$$

and

$$\eta(x) = \frac{\pi^2 c^3 \hbar^2 u_\omega(x k_B T/\hbar)}{k_B^3 T^3}, \tag{1.47}$$

Eq. (1.45) can be expressed as

$$\eta(x) = \frac{x^3}{e^x - 1}. \tag{1.48}$$

Figure 1.7 shows a plot of Eq. (1.48). The energy density per unit frequency has a maximum when $x = 2.822$. It should be noted that the energy density per unit wavelength $u_\lambda(\lambda)$ does not have a maximum at $\frac{2\pi\hbar c}{\lambda k_B T} = 2.822$. Using $\omega = 2\pi\hbar c/\lambda$ in Eq. (1.45), $u_\lambda(\lambda)$ becomes

$$u_\lambda(\lambda) = \frac{16\pi^2\hbar c}{\lambda^5} \frac{1}{e^{2\pi\hbar c/\lambda k_B T} - 1}. \tag{1.49}$$

$u_\lambda(\lambda)$ has a maximum at $\frac{2\pi\hbar c}{\lambda k_B T} = 4.965$, which is equivalent to $\lambda T = 2898[\mu m \cdot K]$. The radiation maximum for $u_\omega(\omega)$ and $u_\lambda(\lambda)$ shifts to higher energies or shorter wavelengths as the temperature rises.

1.2.2 Kirchhoff's law

Consider a body with a finite absorptance in an enclosure at equilibrium. The linear dimension and the radii of curvature of the body are assumed to be large compared to the wavelength of the radiation. The condition of equilibrium requires that the energy of the body does not change with time apart from fluctuations. Because, in a given time, a finite amount of radiation energy is incident on the body, and the body absorbs a certain fraction of it, the body must emit the same amount of energy to maintain at a fixed temperature. Hence, the power absorbed by the body is the same as the power emitted by the body. The *principle of detailed balance* asserts that this statement is valid at each frequency and polarization [20, 38]. Namely, suppose that the body is surrounded by a filter which transmits only the radiation of a specific frequency and polarization. If the radiation energy of the frequency and polarization absorbed by the body is different from the emitted radiation of the same frequency and polarization, the temperature of the body will change with time contrary to the condition of equilibrium.

Let $P_{BB}(\omega)$ be the equilibrium spectral energy flux of black-body radiation per unit area and unit solid angle given by

$$P_{BB}(\omega) = \frac{u_\omega(\omega)c}{4\pi}. \tag{1.50}$$

Note that this quantity is independent of position, direction, and polarization according to the properties of black-body radiation in enclosures given in the previous section. When the radiation flux is incident on the body with a wavevector $\boldsymbol{k}$ which has an angle θ from the surface normal, the spectral energy absorbed per unit surface area and unit solid angle will be $A(\boldsymbol{k},\omega)P_{BB}(\omega)$, where $A(\boldsymbol{k},\omega)$ is the absorptance for incident photons of $\boldsymbol{k}$ and ω. Assume that the light is reflected without random scattering and the radiation that is not reflected is totally absorbed. From the principle of detailed balance, the emitted power $P(-\boldsymbol{k},\omega)$ per unit surface area and unit solid angle for the wavevector $-\boldsymbol{k}$ must be

$$P(-\boldsymbol{k},\omega) = A(\boldsymbol{k},\omega)P_{BB}(\omega)\cos\theta. \tag{1.51}$$

The requirement of $-\boldsymbol{k}$ in Eq. (1.51) follows from the fact that the isotropy of black-body radiation should be conserved. Note that $P(-\boldsymbol{k},\omega)$ is for unit surface area whereas $P_{BB}(\omega)$ is for unit area in the direction of propagation. This explains the factor $\cos\theta$ in Eq. (1.51). Equation (1.51) can be written as

$$\mathcal{E}(-\boldsymbol{k},\omega) = A(\boldsymbol{k},\omega), \tag{1.52}$$

where the *emissivity* $\mathcal{E}(-\boldsymbol{k},\omega)$ is defined by

$$\mathcal{E}(-\boldsymbol{k},\omega) = \frac{P(-\boldsymbol{k},\omega)}{P_{BB}(\omega)\cos\theta}. \tag{1.53}$$

Equation (1.52) is known as *Kirchhoff's law*. It states that the emissivity is equal to the absorptance with the propagation direction reversed. In the above discussion, we note five important points. (i) The emitted power per unit surface area becomes unimportant as $\theta \to 90^\circ$ because of the $\cos\theta$ factor in Eq. (1.51). Any source that

exhibits this rather broad $\cos\theta$ dependence is called the *Lambertian source*. This broad angular distribution is the consequence of the spatially incoherent nature of the source, which will be explained in section 1.3. Examples of Lambertian sources include most thermal sources and light-emitting diodes. However, thermal sources can also exhibit highly directional emission if appropriately structured. This will be the subject of Chapter 5. (ii) Even though $P(-\boldsymbol{k},\omega)$ and $A(\boldsymbol{k},\omega)$ are dependent on the properties of the body, their ratio is independent of the nature of the body. (iii) Kirchhoff's law in the form of Eq. (1.52) breaks down when the linear dimension of the body is comparable to or less than the wavelength of interest. In this case, the absorptance A depends on the size of the incident light and can be much larger than unity [35]. However, when small structural features are periodically placed such that the total dimension of the structure is much larger than the wavelength as in photonic crystals, Kirchhoff's law remains valid. For a proof of this statement, a different formulation is required and will be given in Chapter 2. Note that this considers the far-field where evanescent waves do not exist. In the near-field, Kirchhoff's law cannot be used even when the body is much larger than the wavelength. This is because both absorptance and emissivity refer to propagating waves only. In the case of small bodies or near-field, a different form of Kirchhoff's law which is not expressed in terms of A or $\mathcal{E}$ can be established [39]. (iv) Kirchhoff's law is not valid when luminescence occurs. This is because luminescence is a non-equilibrium phenomenon and Kirchhoff's law is derived for systems in strict equilibrium. Luminescence is actually defined as a violation of Kirchhoff's law [40]. (v) We are most often interested in situations where a body is not in equilibrium with its radiation environment, even though Eq. (1.51) was derived based on equilibrium conditions. For Kirchhoff's law to be used for such a non-equilibrium case, $A(\boldsymbol{k},\omega)$ and $\mathcal{E}(-\boldsymbol{k},\omega)$ have to be defined more carefully. When a body is radiating into an empty space not surrounded by an enclosure, the body does not have an incident field which would increase radiation through stimulated emission. Thus, the difference between an equilibrium and a non-equilibrium case comes through this stimulated emission. However, if $A(\boldsymbol{k},\omega)$ is defined

as stimulated absorption minus stimulated emission and $\mathcal{E}(-\boldsymbol{k},\omega)$ refers to spontaneous emission, the Kirchhoff's law can be used for any non-equilibrium environment [41]. In this case, the only change in the assumption of Kirchhoff's law is that the quantum states of the material (not the photons) can be described by an equilibrium distribution function and the material does not need to be in equilibrium with the radiation. This is the consequence of the fact that the emissivity is associated with the spontaneous emission only. These definitions of $A(\boldsymbol{k},\omega)$ and $\mathcal{E}(-\boldsymbol{k},\omega)$ are exactly the experimentally measurable quantities. In experiment, we cannot separate stimulated absorption and stimulated emission. For example, when we measure reflectance or reflectivity R and use $A = 1 - R$ for an opaque sample to obtain absorptance, the measured reflectivity will be partly due to stimulated emission. Then the obtained A will be absorption minus stimulated emission in agreement with the definition above. Therefore, to use the measured absorptance correctly in Kirchhoff's law, emission experiments should measure only spontaneous emission. This means, in the measurement of emissivity, the emitted radiation should not be allowed to reflect back and strike the sample. Otherwise, we would obtain an emissivity higher than the measured absorptance because the emissivity would be due not only to spontaneous emission but also to stimulated emission. This becomes important for high temperatures and long wavelengths. At high temperatures, more excited states are available and the stimulated emission becomes stronger. A more detailed analysis shows that the condition

$$\exp(-\hbar\omega/k_B T) \ll 1 \tag{1.54}$$

should be satisfied [41]. For errors up to 1%, this amounts to $\lambda T \leq 3150[\mu m \cdot K]$ which is not far from the condition of peak maximum for black-body radiation.

To keep the state of material as close to equilibrium as possible, we should suppress any non-equilibrium processes. For example, the temperature of the body should be nearly constant. If a hot body is immersed in a gas with a different temperature, heat transfer between the body and the gas occurs through convection and increases the

temperature gradient near the surfaces. Using ultra high vacuum, such convection can be suppressed and the temperature gradient can be negligible [42]. In this case, heat conduction inside the body often dominates heat radiation.

1.3 Optical Coherence

In this study of thermal emission modification, optical coherence theory will be used mainly to explain the origin of the angular distribution of the emission. This in turn will give us insight into how we can control the angular dispersion by microstructuring the material. The optical coherence arises from the fact that all optical waves have some random fluctuations. Thus, a correlation of optical fields at two different spatial or temporal points can be defined. The degree of correlation between two optical fluctuations is called the *optical coherence* [43, 44]. Two extremes are completely coherent and completely incoherent sources. If a quasimonochromatic beam at two different moments remains coherent up until a time Δt, we call Δt the *coherence time* of the beam. If the coherence time is very large, the wave has a well-defined frequency by the Fourier transform relationship. This is manifested as a sharp spectral line. When we measure the coherence at two different points by increasing their separation and the beam remains coherent over the separation Δl, this is called the *coherence length*. When the two points are in the direction of the beam propagation, Δl_{lon} is called the longitudinal coherence length. This is directly related to the coherence time by

$$\Delta l_{lon} = c\Delta t. \tag{1.55}$$

If the two points are on the plane perpendicular to the beam, we call Δl_{trn} the transverse coherence length. In this thesis, we will use the term coherence length for Δl_{trn} and designate it simply as Δl. As we will see, this coherence length is related to the angular divergence of the beam. With increasing coherence length, the angular width of the beam decreases.

The spatial coherence for an electromagnetic field of frequency ω is represented by the *cross-spectral density tensors* W_{ij}, defined by [43]

$$\begin{aligned}
\left\langle E_i^*(\boldsymbol{r}_1,\omega)E_j(\boldsymbol{r}_2,\omega')\right\rangle &= W_{ij}^{(e)}(\boldsymbol{r}_1,\boldsymbol{r}_2,\omega)\delta(\omega-\omega') \\
\left\langle H_i^*(\boldsymbol{r}_1,\omega)H_j(\boldsymbol{r}_2,\omega')\right\rangle &= W_{ij}^{(h)}(\boldsymbol{r}_1,\boldsymbol{r}_2,\omega)\delta(\omega-\omega') \\
\left\langle E_i^*(\boldsymbol{r}_1,\omega)H_j(\boldsymbol{r}_2,\omega')\right\rangle &= W_{ij}^{(m)}(\boldsymbol{r}_1,\boldsymbol{r}_2,\omega)\delta(\omega-\omega') \\
\left\langle H_i^*(\boldsymbol{r}_1,\omega)E_j(\boldsymbol{r}_2,\omega')\right\rangle &= W_{ij}^{(n)}(\boldsymbol{r}_1,\boldsymbol{r}_2,\omega)\delta(\omega-\omega'),
\end{aligned} \tag{1.56}$$

where E and H are the electric and magnetic fields respectively, the subscripts i, j stand for the Cartesian components, and δ is the Dirac delta function. $W_{ij}^{(e)}$ and $W_{ij}^{(h)}$ are the *electric* and *magnetic cross-spectral density tensors* respectively and $W_{ij}^{(m)}$ and $W_{ij}^{(n)}$ are *mixed cross-spectral density tensors*. To simplify matters, we often ignore the polarization properties and use scalar waves. In this case, we consider scalar wave fields $V(\boldsymbol{r},\omega)$ and the *cross-spectral density function* W is defined by

$$\left\langle V^*(\boldsymbol{r}_1,\omega)V(\boldsymbol{r}_2,\omega')\right\rangle = W(\boldsymbol{r}_1,\boldsymbol{r}_2,\omega)\delta(\omega-\omega'). \tag{1.57}$$

For spatial coherence, it is convenient to define vectors that are parallel to the emission source plane. We define the parallel position vector $\boldsymbol{r}_\parallel = \boldsymbol{r}\sin\theta$ and the parallel wavevector $\boldsymbol{k}_\parallel = \boldsymbol{k}\sin\theta$ where θ is the polar angle measured from the surface normal. The cross-spectral density function is related to the emissivity by [43]

$$W(\boldsymbol{r}_{\parallel 1},\boldsymbol{r}_{\parallel 2},\omega) \propto \int d\boldsymbol{k}_\parallel \frac{\mathcal{E}(\boldsymbol{k}_\parallel,\omega)}{\cos\theta} e^{i\boldsymbol{k}_\parallel\cdot(\boldsymbol{r}_{\parallel 2}-\boldsymbol{r}_{\parallel 1})}. \tag{1.58}$$

Eq. (1.58) shows that the cross-spectral density function is proportional to the Fourier transform of the emissivity apart from the $\cos\theta$ factor. Thus, a long range spatial correlation on the source plane results in a narrow angular divergence of the emissivity. This relation can be understood by considering interference. For example, if all the fields on the source plane are in-phase with each other, as in a laser, the waves resulting from the fields will constructively interfere only in the surface normal direction. Then the light will propagate as a beam in the normal direction. When the angular divergence

of the beam is narrow such that $\sin\theta \simeq \theta$, Eq. (1.58) can take a simpler form. In this case, the cross-spectral density function becomes

$$\begin{aligned} W(\boldsymbol{R}_{\parallel},\omega) &\sim \frac{1}{\pi(k\theta)^2}\int_0^{2\pi} d\phi \int_0^{k\theta} dk_{\parallel} k_{\parallel} e^{ik_{\parallel}R_{\parallel}\cos\phi} \\ &= \frac{2}{x^2}\int_0^{x} dy y J_0(y) \\ &= \frac{2J_1(x)}{x}, \end{aligned} \tag{1.59}$$

where $\boldsymbol{R}_{\parallel} = \boldsymbol{r}_{\parallel 2} - \boldsymbol{r}_{\parallel 1}$, $x = k\theta R_{\parallel}$, and J_n is the Bessel function of the n^{th} kind. Note that this definition of x is different from Eq. (1.46). $W(\boldsymbol{R}_{\parallel},\omega)$ is normalized by $W(0,\omega)$ and we assumed $\mathcal{E} = 1$ over the angle θ and $\mathcal{E} = 0$ otherwise in Eq. (1.59). The function W as a function of x is shown in Fig. 1.8. The coherence length can be defined by the length over which the normalized cross-spectral density function becomes $1/e$. From Eq. (1.59), the coherence length corresponds to $x = k\theta\Delta l = 2.584$. This yields

$$\Delta l = 0.822\frac{\lambda}{\Delta\theta}, \tag{1.60}$$

where $\Delta\theta = 2\theta$ is the angular width of the beam. Thus, the divergence angle of the emitted light is inversely proportional to the coherence length on the source plane. In general, we can write

$$\Delta l \sim \frac{\lambda}{\Delta\theta}. \tag{1.61}$$

For a one-dimensional case, Eq. (1.58) becomes

$$\begin{aligned} W(\boldsymbol{R}_{\parallel},\omega) &\sim \frac{1}{2k\theta}\int_{-k\theta}^{k\theta} dk_{\parallel} e^{ik_{\parallel}R_{\parallel}} \\ &= \frac{\sin x}{x}. \end{aligned} \tag{1.62}$$

This function behaves similar to Fig. 1.8.

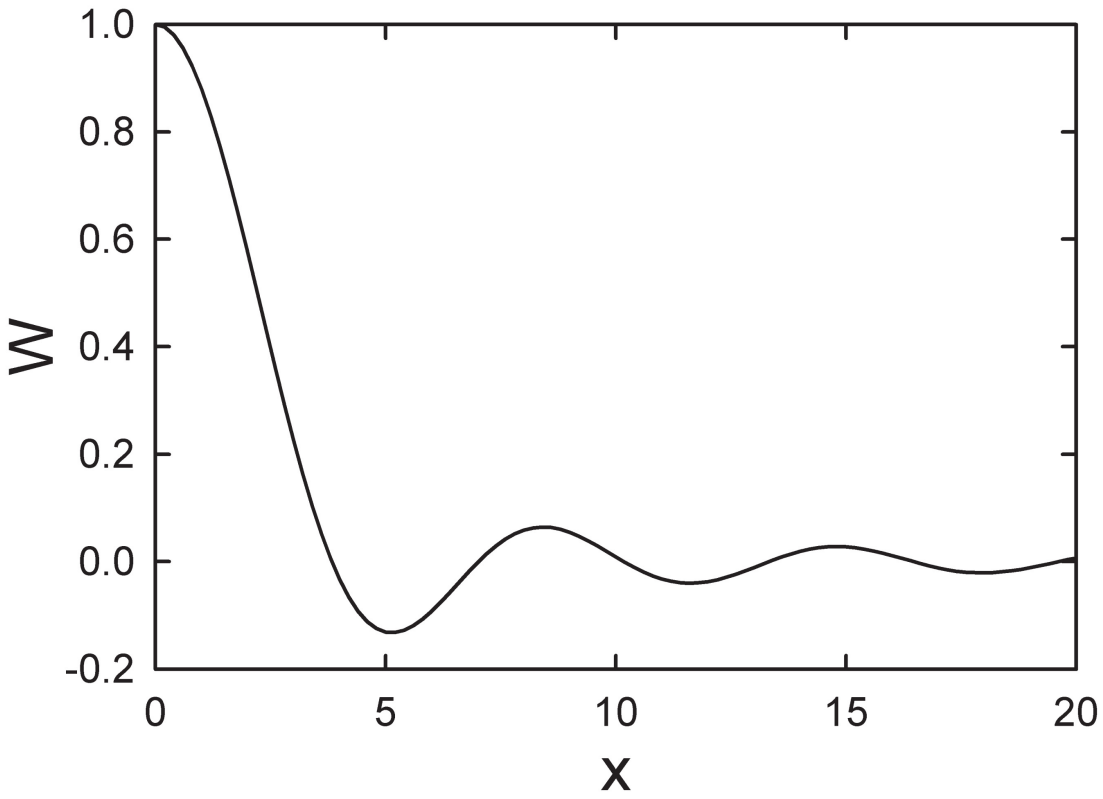

Figure 1.8: The cross-spectral density function W as a function of $x = k\theta R_{\|}$.

References

[1] P. C. Sorcar, *Energy saving lighting systems* (Van Nostrand Reinhold, New York, 1982).

[2] E. Yablonovitch, "Inhibited spontaneous emission in solid-state physics and electronics," Phys. Rev. Lett. **58**, 2059-2062 (1987).

[3] J. D. Joannopoulos, *Photonic crystals : Molding the flow of light* (Princeton University Press, Princeton, 2008).

[4] J. -M. Lourtioz, H. Benisty, V. Berger, J. -M Gérard, D. Maystre, and A. Tchelnokov, *Photonic crystals : Towards nanoscale photonic devices* (Springer, Berlin, 2005).

[5] K. Sakoda, *Optical properties of photonic crystals* (Springer, Berlin, 2001).

[6] K. Busch, *Photonic crystals : Advances in design, fabrication, and characterization* (Wiley-VCH, Weinheim, 2004).

[7] C. M. Cornelius and J. P. Dowling, "Modification of planck blackbody radiation by photonic band-gap structures," Phys. Rev. A **59**, 4736-4746 (1999).

[8] S. Y. Lin, J. G. Fleming, E. Chow, J. Bur, K. K. Choi, and A. Goldberg, "Enhancement and suppression of thermal emission by a three-dimensional photonic crystal," Phys. Rev. B **62**, R2243-R2246 (2000).

[9] S. Y. Lin, J. Moreno, and J. G. Fleming, "Three-dimensional photonic-crystal emitter for thermal photovoltaic power generation," Appl. Phys. Lett. **83**, 380-382 (2003).

[10] S. Y. Lin, J. G. Fleming, and I. El-Kady, "Experimental observation of photonic crystal emission near a photonic band edge," Appl. Phys. Lett. **83**, 593-595 (2003).

[11] S. Y. Lin, J. G. Fleming, and I. El-Kady, "Highly efficient light emission at $\lambda = 1.5$ μm by a three-dimensional tungsten photonic crystal," Opt. Lett. **28**, 1683-1685 (2003).

[12] S. John and R. Wang, "Metallic photonic-band-gap filament architectures for optimized incandescent lighting," Phys. Rev. A **78**, 043809 (2008).

[13] P. Nagpal, S. E. Han, A. Stein, and D. J. Norris, "Efficient low-temperature thermophotovoltaic emitters from metallic photonic crystals," Nano Lett. **8**, 3238-3243 (2008).

[14] M. Laroche, R. Carminati, and J.-J. Greffet, "Coherent thermal antenna using a photonic crystal slab," Phys. Rev. Lett. **96**, 123903 (2006).

[15] C. Kittel, *Introduction to solid state physics* (Wiley, New York, 1966).

[16] N. W. Ashcroft, *Solid state physics* (Brooks Cole, 1976).

[17] Z.-Y. Li, L.-L. Lin, and Z.-Q. Zhang, "Spontaneous emission from photonic crystals: Full vectorial calculations," Phys. Rev. Lett. **84**, 4341-4344 (2000).

[18] K. Busch and S. John, "Photonic band gap formation in certain self-organizing systems," Phys. Rev. E **58**, 3896-3908 (1998).

[19] L. D. Landau and E. M. Lifshitz, *Statistical physics*, 3rd ed. Part 1 (Reed Educational and Professional Publishing, Oxford, 1980).

[20] F. Reif, *Fundamentals of statistical and thermal physics* (McGraw-Hill, New York, 1965).

[21] M. A. Ordal, R. J. Bell, Jr R. W. Alexander, L. L. Long, and M. R. Querry, "Optical properties of fourteen metals in the infrared and far infrared: Al, Co, Cu, Au, Fe, Pb, Mo, Ni, Pd, Pt, Ag, Ti, V, and W," Appl. Opt. **24**, 4493-4499 (1985).

[22] V. Kuzmiak and A. A. Maradudin, "Photonic band structures of one- and two-dimensional periodic systems with metallic components in the presence of dissipation" Phys. Rev. B **55**, 7427-7444 (1997).

[23] A. A. Krokhin and P. Halevi, "Influence of weak dissipation on the photonic band structure of periodic composites," Phys. Rev. B **53**, 1205-1214 (1996).

[24] J. B. Pendry, A. J. Holden, W. J. Stewart, and I. Youngs, "Extremely low frequency plasmons in metallic mesostructures," Phys. Rev. Lett. **76**, 4773-4776 (1996).

[25] S. A. Mikhailov, "Comment on 'Extremely low frequency plasmons in metallic mesostructures,' " Phys. Rev. Lett. **78**, 4135 (1997).

[26] J. B. Pendry, A. J. Holden, W. J. Stewart, and I. Youngs, "Pendry *et al.* Reply:" Phys. Rev. Lett. **78**, 4136 (1997).

[27] R. M. Walser, A. P. Valanju, and P. M. Valanju, "Comment on 'Extremely low frequency plasmons in metallic mesostructures,' " Phys. Rev. Lett. **87**, 119701 (2001).

[28] J. B. Pendry, A. J. Holden, D. J. Robbins, and W. J. Stewart, "Low frequency plasmons in thin-wire structures," J. Phys.: Condens. Matter **10**, 4785-4809 (1998).

[29] A. L. Pokrovsky, "Analytical and numerical studies of wire-mesh metallic photonic crystals," Phys. Rev. B **69**, 195108 (2004).

[30] E. Özbay, B. Temelkuran, M. Sigalas, G. Tuttle, C. M. Soukoulis, and K. M. Ho, "Defect structures in metallic photonic crystals," Appl. Phys. Lett. **69**, 3797-3799 (1996).

[31] A. Moroz, "Three-dimensional complete photonic-band-gap structures in the visible," Phys. Rev. Lett. **83**, 5274-5277 (1999).

[32] J. G. Fleming, S. Y. Lin, I. El-Kady, R. Biswas, and K. M. Ho, "All-metallic three-dimensional photonic crystals with a large infrared bandgap," Nature **417**, 52-55 (2002).

[33] Z.-Y. Li, I. El-Kady, K.-M. Ho, S. Y. Lin, and J. G. Fleming, "Photonic band gap effect in layer-by-layer metallic photonic crystals," J. Appl. Phys. **93**, 38-42 (2003).

[34] *Surface polaritons: Electromagnetic waves at surfaces and interfaces* edited by V. M. Agranovich and D. L. Mills (North-Holland, Amsterdam, 1982).

[35] C. F. Bohren and D. R. Huffman, *Absorption and scattering of light by small particles* (Wiley, New York, 1998).

[36] H. Raether, *Surface plasmons on smooth and rough surfaces and on gratings* (Springer-Verlag, Berlin, 1988).

[37] W. L. Barnes, A. Dereux, and T. W. Ebbesen, "Surface plasmon subwavelength optics," Nature **424**, 824-830 (2003).

[38] C. Kittel, *Thermal physics* (W. H. Freeman, San Francisco, 1980).

[39] S. M. Rytov, Yu. A. Kravtsov, and V. I. Tatarskii, *Principles of statistical radiophysics vol. 3: Elements of random fields* (Springer-Verlag, Berlin, 1989).

[40] P. Pringsheim, *Luminescence of liquids and solids and its practical applications* (Interscience publishers, New York, 1943).

[41] H. P. Baltes, "On the validity of Kirchhoff's law of heat radiation for a body in a nonequilibriumm environment," Prog. Opt. **13**, 1-25 (1976).

[42] A. Kittel, W. Müller-Hirsch, J. Parisi, S.-A. Biehs, D. Reddig, and M. Holthaus, "Near-field heat transfer in a scanning thermal microscope," Phys. Rev. Lett. **95**, 224301 (2005).

[43] L. Mandel and E. Wolf, *Optical coherence and quantum optics* (Cambridge University Press, Cambridge, 1995).

[44] M. Born and E. Wolf, *Principles of optics : Electromagnetic theory of propagation, interference and diffraction of light* (Pergamon Press, Oxford, 1965).

Chapter 2

Theory of Thermal Emission from Periodic Structures*

"In mathematics you don't understand things. You just get used to them."

Johann von Neumann

2.1 Introduction

Control of thermal emission is essential for various applications including lighting [1], imaging [2], and heat-to-electrical conversion systems such as in thermophotovoltaics [3, 4]. Thermal emission can be dramatically modified when the heated objects are periodically structured on an optical length scale [5, 6, 7]. In these structures, known as photonic crystals [8], optical diffraction leads to a modification of the photonic density of states. This affects the thermal emission. A recent experimental study reported thermal emission from a photonic crystal could exceed Planck's black-body limit [3].

* Much of Chapter 2 will appear in print: S. E. Han, Phys. Rev. B (to be submitted).

However, it was subsequently argued that this would violate the second law of thermodynamics [9]. This argument assumed thermal equilibrium between the photonic crystal and the radiation field. Consequently, a potential explanation for the experiments was that they represented the effect of non-equilibrium processes. Out of equilibrium, the emission could potentially be higher than the black-body [10, 11, 12]. However, theoretical calculations later predicted that the black-body limit should be maintained as long as thermal equilibrium is achieved inside the emitting material [13]. In other words, the emitter does not need to be in equilibrium with the electromagnetic field. Subsequent experiments supported this conclusion [14, 15]. However, these experiments only probed the properties of specific photonic crystal structures and a proof for arbitrary periodic structures is still needed. In this chapter, we provide this proof using fluctuational electrodynamics. The formalism used can also be extended to thermal near-fields. We present, for the first time, the calculations of optical coherence in the near-field of a periodic structure. We also show that the behavior of the electric energy density in the near-field of a photonic crystal is different from a flat surface. For example, at a distance z from the surface, the electric energy density does not necessarily scale as $1/z^3$ in the near-field, as is the case for a flat surface [16, 17].

2.2 Calculating Green's Dyadic from the Transfer Matrix

In the formulation of fluctuational electrodynamics, we will use the Green's dyadic which relates a point source to the resulting fields. Because many methods for calculating electromagnetic fields for periodic structures generate transmission and reflection coefficients, it is useful to obtain the Green's dyadic in terms of these optical coefficients. A matrix constructed from the optical coefficients for the plane waves of different wavevectors and polarizations is called the transfer matrix. In this section, we will find a relation between the Green's dyadic and the transfer matrix.

Consider light thermally emitted into vacuum from a periodically structured film.

For simplicity, we assume that the film is composed of nonmagnetic materials, lies in the xy plane, and extends in z from $-L$ to 0. Due to the periodicity in the xy plane, Bloch waves will be developed. Thus, the fields can be represented by the sum of the Bloch waves as

$$\boldsymbol{V}(\boldsymbol{r}_\parallel, z, \omega) = \sum_{\boldsymbol{k}_\parallel} \boldsymbol{V}_{\boldsymbol{k}_\parallel}(\boldsymbol{r}_\parallel, z, \omega), \tag{2.1}$$

where $\boldsymbol{V}$ is a field, $\boldsymbol{r}_\parallel$ and $\boldsymbol{k}_\parallel$ are the position and the wave vectors parallel to the surface (xy plane), $\boldsymbol{V}_{\boldsymbol{k}_\parallel}$ is the Bloch wave with the wavevector component $\boldsymbol{k}_\parallel$, and ω is the angular frequency. Note that $\boldsymbol{k}_\parallel$ lies in the first Brillouin zone and takes discrete values because the size of the structured film is finite in the xy plane. The Bloch wave $\boldsymbol{V}_{\boldsymbol{k}_\parallel}$ should satisfy the Bloch theorem [see Eq. (1.6)]

$$\boldsymbol{V}_{\boldsymbol{k}_\parallel}(\boldsymbol{r}_\parallel + \boldsymbol{a}_\parallel, z, \omega) = \boldsymbol{V}_{\boldsymbol{k}_\parallel}(\boldsymbol{r}_\parallel, z, \omega) e^{i\boldsymbol{k}_\parallel \cdot \boldsymbol{a}_\parallel}, \tag{2.2}$$

where $\boldsymbol{a}_\parallel$ is the lattice vector in the xy plane. If we expand the Bloch wave using the reciprocal lattice vector $\boldsymbol{g}_\parallel$ as

$$\boldsymbol{V}_{\boldsymbol{k}_\parallel}(\boldsymbol{r}_\parallel, z, \omega) = \sum_{\boldsymbol{g}_\parallel} \widetilde{\boldsymbol{V}}(\boldsymbol{k}_\parallel + \boldsymbol{g}_\parallel, z, \omega) e^{i(\boldsymbol{k}_\parallel + \boldsymbol{g}_\parallel)\cdot \boldsymbol{r}_\parallel}, \tag{2.3}$$

the Bloch theorem (Eq. (2.2)) is satisfied because

$$e^{i\boldsymbol{g}_\parallel \cdot \boldsymbol{a}_\parallel} = 1. \tag{2.4}$$

$\widetilde{\boldsymbol{V}}$ can be obtained by the two-dimensional inverse Fourier transform of Eq. (2.3) as

$$\widetilde{\boldsymbol{V}}(\boldsymbol{k}_\parallel + \boldsymbol{g}_\parallel, z, \omega) = \frac{1}{\int_{uc} d\boldsymbol{r}_\parallel} \int_{uc} d\boldsymbol{r}_\parallel \boldsymbol{V}_{\boldsymbol{k}_\parallel}(\boldsymbol{r}_\parallel, z, \omega) e^{-i(\boldsymbol{k}_\parallel + \boldsymbol{g}_\parallel)\cdot \boldsymbol{r}_\parallel}, \tag{2.5}$$

where uc stands for the two-dimensional unit cell in the xy plane. Substituting Eq. (2.3) into (2.1), we have

$$\boldsymbol{V}(\boldsymbol{r}_\parallel, z, \omega) = \sum_{\boldsymbol{k}_\parallel} \sum_{\boldsymbol{g}_\parallel} \widetilde{\boldsymbol{V}}(\boldsymbol{k}_\parallel + \boldsymbol{g}_\parallel, z, \omega) e^{i(\boldsymbol{k}_\parallel + \boldsymbol{g}_\parallel)\cdot \boldsymbol{r}_\parallel}. \tag{2.6}$$

Therefore $\widetilde{\boldsymbol{V}}$ can also be obtained by the inverse Fourier transform of Eq. (2.6) as

$$\widetilde{\boldsymbol{V}}(\boldsymbol{k}_\parallel + \boldsymbol{g}_\parallel, z, \omega) = \frac{1}{\int d\boldsymbol{r}_\parallel} \int d\boldsymbol{r}_\parallel \boldsymbol{V}(\boldsymbol{r}_\parallel, z, \omega) e^{-i(\boldsymbol{k}_\parallel + \boldsymbol{g}_\parallel)\cdot \boldsymbol{r}_\parallel}. \tag{2.7}$$

Consider the electric field in vacuum that results from the thermal fluctuations in the electric current $\boldsymbol{j}$ inside the structure. They are related to each other through the Green's dyadic G as

$$\boldsymbol{E}(\boldsymbol{r}_\parallel, z, \omega) = i\omega\mu_0 \int d\boldsymbol{r}'_\parallel \int dz'\, G(\boldsymbol{r}_\parallel, \boldsymbol{r}'_\parallel; z, z'; \omega) \cdot \boldsymbol{j}(\boldsymbol{r}'_\parallel, z', \omega), \tag{2.8}$$

where μ_0 is the permeability of free space. The Green's dyadic $G(\boldsymbol{r}_\parallel, \boldsymbol{r}'_\parallel; z, z'; \omega)$ relates the electric current at position $(\boldsymbol{r}'_\parallel, z')$ to the electric field at position $(\boldsymbol{r}_\parallel, z)$ at frequency ω. The Green's dyadic is known to satisfy [18]

$$G^T(\boldsymbol{r}_\parallel, \boldsymbol{r}'_\parallel; z, z'; \omega) = G(\boldsymbol{r}'_\parallel, \boldsymbol{r}_\parallel; z', z; \omega). \tag{2.9}$$

Equation (2.9) is the consequence of the electrodynamic reciprocity theorem [16, 19]. This theorem will be explained in section 3.1. Substituting Eq. (2.6) for $\boldsymbol{V} = \boldsymbol{j}$ into Eq. (2.8) and the resulting equation into Eq. (2.7) for $\boldsymbol{V} = \boldsymbol{E}$, we have

$$\widetilde{\boldsymbol{E}}(\boldsymbol{k}_\parallel + \boldsymbol{g}_\parallel, z, \omega) = \sum_{\boldsymbol{k}'_\parallel, \boldsymbol{g}'_\parallel} \int dz'\, G(\boldsymbol{k}_\parallel + \boldsymbol{g}_\parallel, \boldsymbol{k}'_\parallel + \boldsymbol{g}'_\parallel; z, z'; \omega) \cdot \widetilde{\boldsymbol{j}}(\boldsymbol{k}'_\parallel + \boldsymbol{g}'_\parallel, z', \omega), \tag{2.10}$$

where

$$G(\boldsymbol{k}_\parallel + \boldsymbol{g}_\parallel, \boldsymbol{k}'_\parallel + \boldsymbol{g}'_\parallel; z, z'; \omega) = \frac{i\omega\mu_0}{\int d\boldsymbol{r}_\parallel} \int d\boldsymbol{r}_\parallel \int d\boldsymbol{r}'_\parallel G(\boldsymbol{r}_\parallel, \boldsymbol{r}'_\parallel; z, z'; \omega) e^{i\left[(\boldsymbol{k}'_\parallel + \boldsymbol{g}'_\parallel)\cdot \boldsymbol{r}'_\parallel - (\boldsymbol{k}_\parallel + \boldsymbol{g}_\parallel)\cdot \boldsymbol{r}_\parallel\right]}. \tag{2.11}$$

In Eq. (2.10), $\widetilde{\boldsymbol{E}}$ and $\widetilde{\boldsymbol{j}}$ should have the same $\boldsymbol{k}_\parallel$ because of the conservation of parallel momentum. Thus the Green's dyadic satisfies

$$G(\boldsymbol{k}_\parallel + \boldsymbol{g}_\parallel, \boldsymbol{k}'_\parallel + \boldsymbol{g}'_\parallel; z, z'; \omega) = G(\boldsymbol{k}_\parallel + \boldsymbol{g}_\parallel, \boldsymbol{k}_\parallel + \boldsymbol{g}'_\parallel; z, z'; \omega) \delta_{\boldsymbol{k}_\parallel, \boldsymbol{k}'_\parallel} \tag{2.12}$$

and Eq. (2.10) becomes

$$\widetilde{\boldsymbol{E}}(\boldsymbol{k}_\parallel + \boldsymbol{g}_\parallel, z, \omega) = \sum_{\boldsymbol{g}'_\parallel} \int dz'\, G(\boldsymbol{k}_\parallel + \boldsymbol{g}_\parallel, \boldsymbol{k}_\parallel + \boldsymbol{g}'_\parallel; z, z'; \omega) \cdot \widetilde{\boldsymbol{j}}(\boldsymbol{k}_\parallel + \boldsymbol{g}'_\parallel, z', \omega). \tag{2.13}$$

The Green's dyadic $G(\boldsymbol{k}_\parallel + \boldsymbol{g}_\parallel, \boldsymbol{k}_\parallel + \boldsymbol{g}'_\parallel; z, z'; \omega)$ relates the electric current component of parallel wavevector $\boldsymbol{k}_\parallel + \boldsymbol{g}'_\parallel$ at the $z = z'$ plane to the electric field component of parallel wavevector $\boldsymbol{k}_\parallel + \boldsymbol{g}_\parallel$ at the $z = z$ plane at frequency ω. Taking the transpose of Eq. (2.11) and using Eqs. (2.9) and (2.12), we have

$$G^T(\boldsymbol{k}_\parallel + \boldsymbol{g}_\parallel, \boldsymbol{k}_\parallel + \boldsymbol{g}'_\parallel; z, z'; \omega) = G(-\boldsymbol{k}_\parallel - \boldsymbol{g}'_\parallel, -\boldsymbol{k}_\parallel - \boldsymbol{g}_\parallel; z', z; \omega). \tag{2.14}$$

$G(\boldsymbol{r}_\parallel, \boldsymbol{r}'_\parallel; z, z'; \omega)$ can be expressed by taking the Fourier transform of Eq. (2.11) and using Eq. (2.14) as

$$\begin{aligned} G(\boldsymbol{r}_\parallel, \boldsymbol{r}'_\parallel; z, z'; \omega) &= \frac{1}{i\omega\mu_0 \int d\boldsymbol{r}_\parallel} \sum_{\boldsymbol{k}_\parallel} \sum_{\boldsymbol{g}_\parallel, \boldsymbol{g}'_\parallel} G^T(-\boldsymbol{k}_\parallel - \boldsymbol{g}'_\parallel, -\boldsymbol{k}_\parallel - \boldsymbol{g}_\parallel; z', z; \omega) \\ &\quad \times e^{i(\boldsymbol{k}_\parallel + \boldsymbol{g}_\parallel)\cdot \boldsymbol{r}_\parallel - i(\boldsymbol{k}_\parallel + \boldsymbol{g}'_\parallel)\cdot \boldsymbol{r}'_\parallel} \end{aligned} \tag{2.15}$$

To consider the polarization property of thermal emission, we define s- and p-polarization unit vectors as [20]

$$\begin{aligned} \hat{\boldsymbol{s}}_{\boldsymbol{q}_\parallel, \pm} &\equiv \hat{\boldsymbol{q}}_\parallel \times \hat{\boldsymbol{z}} \\ \hat{\boldsymbol{p}}_{\boldsymbol{q}_\parallel, \pm} &\equiv \frac{c}{\omega}[\mp k_{z,v}(\boldsymbol{q}_\parallel, \omega)\hat{\boldsymbol{q}}_\parallel + |\boldsymbol{q}_\parallel|\hat{\boldsymbol{z}}], \end{aligned} \tag{2.16}$$

where $\boldsymbol{q}_\parallel = \boldsymbol{k}_\parallel + \boldsymbol{g}_\parallel$, $\hat{\boldsymbol{q}}_\parallel = \boldsymbol{q}_\parallel / |\boldsymbol{q}_\parallel|$, and $+$ and $-$ indicate whether the light is propagating or evanescent in the $+z$ and $-z$ directions, respectively. In Eq. (2.16), $k_{z,v}$ is the z component of the wavevector in vacuum and is obtained by

$$k_{z,v}(\boldsymbol{k}_\parallel + \boldsymbol{g}_\parallel, \omega) = \sqrt{\frac{\omega^2}{c^2} - |\boldsymbol{k}_\parallel + \boldsymbol{g}_\parallel|^2}, \tag{2.17}$$

and $k_{z,v}$ is taken such that its imaginary part is positive but, if the imaginary part vanishes, the real part is non-negative. This sign convention is chosen to ensure that the wave is propagating or evanescent in the $\pm z$ direction for the $\pm$ sign in Eq. (2.16).

To relate the Green's dyadic to the transfer matrix, consider an electric field in vacuum at the $z > 0$ plane generated by a current at the same plane. This electric field

incident on the structure is [20]

$$d\widetilde{\boldsymbol{E}}_{inc}(-\boldsymbol{k}_{\parallel}-\boldsymbol{g}_{\parallel},z,\omega)=-\frac{\omega\mu_0}{2k_{z,v}(\boldsymbol{k}_{\parallel}+\boldsymbol{g}_{\parallel},\omega)}\sum_{\alpha}\hat{\boldsymbol{\alpha}}_{-\boldsymbol{k}_{\parallel}-\boldsymbol{g}_{\parallel},-}\hat{\boldsymbol{\alpha}}_{-\boldsymbol{k}_{\parallel}-\boldsymbol{g}_{\parallel},-}\cdot\widetilde{\boldsymbol{j}}(-\boldsymbol{k}_{\parallel}-\boldsymbol{g}_{\parallel},z,\omega)dz \tag{2.18}$$

where the subscript *inc* denotes incident light and $\hat{\boldsymbol{\alpha}}$=$\hat{\boldsymbol{s}}$ or $\hat{\boldsymbol{p}}$. The electric field at a different plane $z'<0$ with parallel wavevector $-\boldsymbol{k}_{\parallel}-\boldsymbol{g}'_{\parallel}$ resulting from the incident wave is expressed in terms of the transfer matrix M by

$$d\widetilde{\boldsymbol{E}}(-\boldsymbol{k}_{\parallel}-\boldsymbol{g}'_{\parallel},z',\omega)=\sum_{\boldsymbol{g}_{\parallel}}M(-\boldsymbol{k}_{\parallel}-\boldsymbol{g}'_{\parallel},-\boldsymbol{k}_{\parallel}-\boldsymbol{g}_{\parallel};z',z;\omega)\cdot d\widetilde{\boldsymbol{E}}_{inc}(-\boldsymbol{k}_{\parallel}-\boldsymbol{g}_{\parallel},z,\omega). \tag{2.19}$$

Plugging Eq. (2.18) into Eq. (2.19) and comparing the resulting equation with

$$d\widetilde{\boldsymbol{E}}(-\boldsymbol{k}_{\parallel}-\boldsymbol{g}'_{\parallel},z',\omega)=\sum_{\boldsymbol{g}_{\parallel}}G(-\boldsymbol{k}_{\parallel}-\boldsymbol{g}'_{\parallel},-\boldsymbol{k}_{\parallel}-\boldsymbol{g}_{\parallel};z',z;\omega)\cdot\widetilde{\boldsymbol{j}}(-\boldsymbol{k}_{\parallel}-\boldsymbol{g}_{\parallel},z,\omega)dz, \tag{2.20}$$

we obtain

$$G(-\boldsymbol{k}_{\parallel}-\boldsymbol{g}'_{\parallel},-\boldsymbol{k}_{\parallel}-\boldsymbol{g}_{\parallel};z',z;\omega)=\sum_{\alpha}-\frac{\omega\mu_0}{2k_{z,v}(\boldsymbol{k}_{\parallel}+\boldsymbol{g}_{\parallel},\omega)}M^{\alpha-}(-\boldsymbol{k}_{\parallel}-\boldsymbol{g}'_{\parallel},-\boldsymbol{k}_{\parallel}-\boldsymbol{g}_{\parallel};z',z;\omega), \tag{2.21}$$

where $M^{\alpha-}$ is defined by

$$M^{\alpha-}(-\boldsymbol{k}_{\parallel}-\boldsymbol{g}'_{\parallel},-\boldsymbol{k}_{\parallel}-\boldsymbol{g}_{\parallel};z',z;\omega)\equiv M(-\boldsymbol{k}_{\parallel}-\boldsymbol{g}'_{\parallel},-\boldsymbol{k}_{\parallel}-\boldsymbol{g}_{\parallel};z',z;\omega)\cdot\hat{\boldsymbol{\alpha}}_{-\boldsymbol{k}_{\parallel}-\boldsymbol{g}_{\parallel},-}\hat{\boldsymbol{\alpha}}_{-\boldsymbol{k}_{\parallel}-\boldsymbol{g}_{\parallel},-}. \tag{2.22}$$

$M^{\alpha-}(-\boldsymbol{k}_{\parallel}-\boldsymbol{g}'_{\parallel},-\boldsymbol{k}_{\parallel}-\boldsymbol{g}_{\parallel};z',z;\omega)$ can be viewed as the electric field of the parallel wavevector $-\boldsymbol{k}_{\parallel}-\boldsymbol{g}'_{\parallel}$ at $z=z'$ resulting from the α-polarized electric current of unit amplitude and the parallel wavevector $-\boldsymbol{k}_{\parallel}-\boldsymbol{g}_{\parallel}$ at $z=z(>z')$ and frequency ω. Substituting Eq. (2.21) into Eq. (2.15), we obtain

$$\begin{aligned}G(\boldsymbol{r}_{\parallel},\boldsymbol{r}'_{\parallel};z,z';\omega) &= \sum_{\alpha}\sum_{\boldsymbol{k}_{\parallel}}\sum_{\boldsymbol{g}_{\parallel},\boldsymbol{g}'_{\parallel}}\frac{i}{2k_{z,v}(\boldsymbol{k}_{\parallel}+\boldsymbol{g}_{\parallel},\omega)\int d\boldsymbol{r}_{\parallel}}\\ &\quad\times M^{\alpha-T}(-\boldsymbol{k}_{\parallel}-\boldsymbol{g}'_{\parallel},-\boldsymbol{k}_{\parallel}-\boldsymbol{g}_{\parallel};z',z;\omega)e^{i(\boldsymbol{k}_{\parallel}+\boldsymbol{g}_{\parallel})\cdot\boldsymbol{r}_{\parallel}-i(\boldsymbol{k}_{\parallel}+\boldsymbol{g}'_{\parallel})\cdot\boldsymbol{r}'_{\parallel}}.\end{aligned} \tag{2.23}$$

Hence, we can find the real space Green's dyadic from the transfer matrix using Eq. (2.23). The Green's dyadic will now be used to derive Kirchhoff's law (section 2.3) and to calculate the field correlations (section 2.4).

2.3 Kirchhoff's Law for Photonic Crystals

Kirchhoff's law is derived with the assumption that both (1) the length of the object and (2) the distance from the object is much larger than the wavelength. The first condition is imposed in order to use geometric optics and the second to exclude near-fields where evanescent waves exist. As the two assumptions break down, interesting phenomena that do not necessarily obey Kirchhoff's law can be expected. Here, we modify the first assumption by considering periodic structures whose structural components are comparable to or less than the wavelength in size but whose overall dimension is much larger than the wavelength. The second assumption of the far-field is still imposed. In this case, Kirchhoff's law is obeyed as will be shown below.

A Fourier component of the electric field in vacuum above the structure ($z > 0$) can be expressed in terms of the field at the surface ($z = 0$) by

$$\widetilde{\boldsymbol{E}}(\boldsymbol{k}_\parallel + \boldsymbol{g}_\parallel, z, \omega) = \widetilde{\boldsymbol{E}}(\boldsymbol{k}_\parallel + \boldsymbol{g}_\parallel, 0, \omega) e^{ik_{z,v}(\boldsymbol{k}_\parallel + \boldsymbol{g}_\parallel, \omega) z}. \tag{2.24}$$

Substituting Eq. (2.24) into Eq. (2.6) with $\boldsymbol{V} = \boldsymbol{E}$ and using the method of stationary phase [21], we can obtain the far-field form of the electric field as

$$\boldsymbol{E}(\boldsymbol{r}_\parallel, z, \omega) \longrightarrow -\frac{\int d\boldsymbol{r}_\parallel}{2\pi} i \frac{\omega}{c} \cos\theta \frac{e^{i\frac{\omega}{c} r}}{r} \widetilde{\boldsymbol{E}}(\boldsymbol{\kappa}, 0, \omega), \tag{2.25}$$

where $r = |\boldsymbol{r}_\parallel + z\hat{\boldsymbol{z}}|$, $\boldsymbol{\kappa} = \frac{\omega}{c}\frac{\boldsymbol{r}_\parallel}{r}$ is the wavevector parallel to the film surface, and θ is the angle between the propagation direction and the z-axis. Note that $\boldsymbol{\kappa}$ is for the propagating wave and its magnitude is always less than or equal to ω/c. To take the polarization into account, we define the polarization dependent Green's dyadic $G^{\alpha\pm}$ (α=s or p) as

$$G^{\alpha+}(\boldsymbol{\kappa}, \boldsymbol{k}_\parallel + \boldsymbol{g}'_\parallel; 0, z'; \omega) \quad \equiv \quad \hat{\boldsymbol{\alpha}}\hat{\boldsymbol{\alpha}} \cdot G(\boldsymbol{\kappa}, \boldsymbol{k}_\parallel + \boldsymbol{g}'_\parallel; 0, z'; \omega)$$

$$G^{\alpha-}(-\boldsymbol{k}_\parallel-\boldsymbol{g}'_\parallel,-\boldsymbol{\kappa};z',0;\omega) \equiv G(-\boldsymbol{k}_\parallel-\boldsymbol{g}'_\parallel,-\boldsymbol{\kappa};z',0;\omega)\cdot\hat{\boldsymbol{\alpha}}\hat{\boldsymbol{\alpha}}, \tag{2.26}$$

where $\hat{\boldsymbol{\alpha}}\hat{\boldsymbol{\alpha}}=\hat{\boldsymbol{\alpha}}_{-\boldsymbol{\kappa},-}\hat{\boldsymbol{\alpha}}_{-\boldsymbol{\kappa},-}=\hat{\boldsymbol{\alpha}}_{\boldsymbol{\kappa},+}\hat{\boldsymbol{\alpha}}_{\boldsymbol{\kappa},+}$ with $\hat{\boldsymbol{\alpha}}=\hat{\boldsymbol{s}}$ or $\hat{\boldsymbol{p}}$ and using the same notation as in Eq. (2.16). The Fourier component of the electric field of the α-polarized wave going in the $\pm z$ direction at $z=0$ is obtained as

$$\widetilde{\boldsymbol{E}}^{\alpha\pm}(\boldsymbol{\kappa},0,\omega)=\hat{\boldsymbol{\alpha}}\hat{\boldsymbol{\alpha}}\cdot\widetilde{\boldsymbol{E}}(\boldsymbol{\kappa},0,\omega). \tag{2.27}$$

From Eqs. (2.7), (2.13), (2.26), and (2.27) letting $\boldsymbol{k}_\parallel+\boldsymbol{g}_\parallel=\boldsymbol{\kappa}$, we obtain $\widetilde{\boldsymbol{E}}^{\alpha+}$ using the inverse Fourier transform of $\widetilde{\boldsymbol{j}}$ as

$$\widetilde{\boldsymbol{E}}^{\alpha+}(\boldsymbol{\kappa},0,\omega)=\frac{1}{\int d\boldsymbol{r}_\parallel}\sum_{\boldsymbol{g}'_\parallel}\int d\boldsymbol{r}'_\parallel\int_{-L}^{0}dz'\,e^{-i(\boldsymbol{k}_\parallel+\boldsymbol{g}'_\parallel)\cdot\boldsymbol{r}'_\parallel}G^{\alpha+}(\boldsymbol{\kappa},\boldsymbol{k}_\parallel+\boldsymbol{g}'_\parallel;0,z';\omega)\cdot\boldsymbol{j}(\boldsymbol{r}'_\parallel,z',\omega). \tag{2.28}$$

The ensemble average of $\widetilde{\boldsymbol{E}}^{\alpha+*}(\boldsymbol{\kappa},0,\omega)\cdot\widetilde{\boldsymbol{E}}^{\alpha+}(\boldsymbol{\kappa},0,\omega')$ is obtained from Eq. (2.28) as

$$\begin{aligned}&\left\langle\widetilde{\boldsymbol{E}}^{\alpha+*}(\boldsymbol{\kappa},0,\omega)\cdot\widetilde{\boldsymbol{E}}^{\alpha+}(\boldsymbol{\kappa},0,\omega')\right\rangle\\ =\;&\frac{1}{\int d\boldsymbol{r}_\parallel}\frac{\omega}{\pi}\varepsilon_0\delta(\omega-\omega')\sum_{\boldsymbol{g}'_\parallel,\boldsymbol{g}''_\parallel}\int_{-L}^{0}dz'\,\tilde{f}(\boldsymbol{g}''_\parallel-\boldsymbol{g}'_\parallel,z',\omega)\\ &\times G^{\alpha+*}(\boldsymbol{\kappa},\boldsymbol{k}_\parallel+\boldsymbol{g}'_\parallel;0,z';\omega):G^{\alpha+}(\boldsymbol{\kappa},\boldsymbol{k}_\parallel+\boldsymbol{g}''_\parallel;0,z';\omega),\end{aligned} \tag{2.29}$$

where ε_0 is the permittivity of free space and

$$\tilde{f}(\boldsymbol{g}''_\parallel-\boldsymbol{g}'_\parallel,z',\omega)=\frac{1}{\int d\boldsymbol{r}_\parallel}\int d\boldsymbol{r}'_\parallel e^{i(\boldsymbol{g}'_\parallel-\boldsymbol{g}''_\parallel)\cdot\boldsymbol{r}'_\parallel}\varepsilon_I(\boldsymbol{r}'_\parallel,z',\omega)\frac{\hbar\omega}{e^{\hbar\omega/kT(\boldsymbol{r}'_\parallel,z')}-1}. \tag{2.30}$$

$\tilde{f}$ is the Fourier transform of a function $f(\boldsymbol{r}'_\parallel,z',\omega)\equiv\varepsilon_I(\boldsymbol{r}'_\parallel,z',\omega)\Theta(\omega,T(\boldsymbol{r}'_\parallel,z'))$. Here f is assumed to be periodic in the xy plane. In Eq. (2.30), the two integrations can be done for a unit cell without changing the results, so that the calculation of $\tilde{f}$ becomes simple. Note that the integration is evaluated only over the material portion because $\varepsilon_I=0$ in vacuum. In deriving Eq. (2.29), we used the fluctuation-dissipation theorem assuming local equilibrium [16]

$$\begin{aligned}&\left\langle {j_j}^*(\boldsymbol{r}'_\parallel,z',\omega,T)j_k(\boldsymbol{r}''_\parallel,z'',\omega',T)\right\rangle\\ =\;&\frac{\omega\Theta(\omega,T)}{\pi}\varepsilon_0\varepsilon_I(\boldsymbol{r}'_\parallel,z',\omega)\delta_{jk}\delta(\boldsymbol{r}'_\parallel-\boldsymbol{r}''_\parallel)\delta(z'-z'')\delta(\omega-\omega'),\end{aligned} \tag{2.31}$$

where ε_I is the imaginary part of the dielectric function, $i, j, k = x, y, z$, and $\Theta(\omega, T) = \frac{\hbar\omega}{e^{\hbar\omega/k_B T}-1}$ is the mean energy of the harmonic oscillator minus the zero-point energy. Equation (2.31) says that the thermal currents are delta correlated in position. This is the consequence of the assumption that the medium is without spatial dispersion. The magnitude of the ensemble-averaged Poynting vector $\langle S_\omega^{\alpha+}(\boldsymbol{r}_\parallel, z)\rangle$ of light of α-polarization and frequency ω propagating in the $+z$ direction is given by [22]

$$\langle S_\omega^{\alpha+}(\boldsymbol{r}_\parallel, z)\rangle \delta(\omega - \omega') = \frac{2}{\mu_0 c} \left\langle \boldsymbol{E}^{\alpha+*}(\boldsymbol{r}_\parallel, z, \omega) \cdot \boldsymbol{E}^{\alpha+}(\boldsymbol{r}_\parallel, z, \omega') \right\rangle . \tag{2.32}$$

The emission rate of α-polarized light per unit solid angle per unit frequency per unit area in the far-field is

$$\mathcal{P}^{\alpha+}(\boldsymbol{\kappa}, \omega) = \frac{r^2}{\int d\boldsymbol{r}_\parallel \cos\theta} \langle S_\omega^{\alpha+}(\boldsymbol{r}_\parallel, z)\rangle_{\frac{\omega}{c} r \to \infty}. \tag{2.33}$$

We find the Poynting vector from Eqs. (2.25), (2.29), and (2.32) and insert this into (2.33) to obtain the emission rate. Then the resulting expression is

$$\begin{aligned} \mathcal{P}^{\alpha+}(\boldsymbol{\kappa}, \omega) &= \frac{\omega^3 \cos\theta}{2\pi^3 c^3} \frac{\varepsilon_0}{\mu_0} \sum_{\boldsymbol{g}'_\parallel, \boldsymbol{g}''_\parallel} \int_{-L}^{0} dz' \tilde{f}(\boldsymbol{g}''_\parallel - \boldsymbol{g}'_\parallel, z', \omega) \\ &\quad \times G^{\alpha+*}(\boldsymbol{\kappa}, \boldsymbol{k}_\parallel + \boldsymbol{g}'_\parallel; 0, z'; \omega) : G^{\alpha+}(\boldsymbol{\kappa}, \boldsymbol{k}_\parallel + \boldsymbol{g}''_\parallel; 0, z'; \omega). \end{aligned} \tag{2.34}$$

Now, as in Kirchhoff's law, we wish to relate the emission rate to the parameters in the absorption process. For this, we use the electrodynamic reciprocity theorem Eq. (2.14) for $\boldsymbol{k}_\parallel + \boldsymbol{g}_\parallel = \boldsymbol{\kappa}$ and $z = 0$. We premultiply $\hat{\boldsymbol{\alpha}}\hat{\boldsymbol{\alpha}}$ with Eq. (2.14) and use Eq. (2.26) to find the relation for polarization α as

$$G^{\alpha+}(\boldsymbol{\kappa}, \boldsymbol{k}_\parallel + \boldsymbol{g}'_\parallel; 0, z'; \omega) = G^{\alpha-T}(-\boldsymbol{k}_\parallel - \boldsymbol{g}'_\parallel, -\boldsymbol{\kappa}; z', 0; \omega) \tag{2.35}$$

Substituting Eq. (2.35) into Eq. (2.34), we have

$$\begin{aligned} \mathcal{P}^{\alpha+}(\boldsymbol{\kappa}, \omega) &= \frac{\omega^3 \cos\theta}{2\pi^3 c^3} \frac{\varepsilon_0}{\mu_0} \sum_{\boldsymbol{g}'_\parallel, \boldsymbol{g}''_\parallel} \int_{-L}^{0} dz' \tilde{f}(\boldsymbol{g}''_\parallel - \boldsymbol{g}'_\parallel, z', \omega) \\ &\quad \times G^{\alpha-*}(-\boldsymbol{k}_\parallel - \boldsymbol{g}'_\parallel, -\boldsymbol{\kappa}; z', 0; \omega) : G^{\alpha-}(-\boldsymbol{k}_\parallel - \boldsymbol{g}''_\parallel, -\boldsymbol{\kappa}; z', 0; \omega). \end{aligned} \tag{2.36}$$

In calculating this emission rate, we may use the Green's dyadic in Eq. (2.21). Post-multiplying $\hat{\boldsymbol{\alpha}}\hat{\boldsymbol{\alpha}}$ with Eq. (2.21) for $\boldsymbol{k}_\parallel + \boldsymbol{g}_\parallel = \boldsymbol{\kappa}$ and $z = 0$ and using the orthogonality for different polarizations defined in Eq. (2.16), we obtain the relation

$$G^{\alpha-}(-\boldsymbol{k}_\parallel - \boldsymbol{g}'_\parallel, -\boldsymbol{\kappa}; z', 0; \omega) = -\frac{c\mu_0}{2\cos\theta} M^{\alpha-}(-\boldsymbol{k}_\parallel - \boldsymbol{g}'_\parallel, -\boldsymbol{\kappa}; z', 0; \omega), \tag{2.37}$$

where we used $k_{z,v}(\boldsymbol{\kappa}, \omega) = \frac{\omega}{c}\cos\theta$. Plugging Eq. (2.37) into Eq. (2.36), we find that

$$\begin{aligned} \mathcal{P}^{\alpha+}(\boldsymbol{\kappa}, \omega) &= \frac{\omega^3}{8\pi^3 c^3 \cos\theta} \sum_{\boldsymbol{g}'_\parallel, \boldsymbol{g}''_\parallel} \int_{-L}^{0} dz' \tilde{f}(\boldsymbol{g}''_\parallel - \boldsymbol{g}'_\parallel, z', \omega) \\ &\quad \times M^{\alpha-*}(-\boldsymbol{k}_\parallel - \boldsymbol{g}'_\parallel, -\boldsymbol{\kappa}; z', 0; \omega) : M^{\alpha-}(-\boldsymbol{k}_\parallel - \boldsymbol{g}''_\parallel, -\boldsymbol{\kappa}; z', 0; \omega). \end{aligned} \tag{2.38}$$

Hence the emission rate can be calculated using the transfer matrices.

By expressing transfer matrices in terms of the electric fields, the physics becomes clearer. Similarly to Eq. (2.19), the electric field at a plane $z = z' < 0$ with parallel wavevector $-\boldsymbol{k}_\parallel - \boldsymbol{g}'_\parallel$ resulting from the incident wave of polarization α and parallel wavevector $-\boldsymbol{\kappa}$ is

$$d\widetilde{\boldsymbol{E}}^{(\alpha-)}_{(-\boldsymbol{\kappa},0)}(-\boldsymbol{k}_\parallel - \boldsymbol{g}'_\parallel, z', \omega) = M^{\alpha-}(-\boldsymbol{k}_\parallel - \boldsymbol{g}'_\parallel, -\boldsymbol{\kappa}; z', 0; \omega) \cdot d\widetilde{\boldsymbol{E}}^{\alpha-}_{inc}(-\boldsymbol{\kappa}, 0, \omega). \tag{2.39}$$

In Eq. (2.39) and the following, the brackets in the subscript or superscript are used to describe the incident light that leads to a quantity inside the film, in this case $d\widetilde{\boldsymbol{E}}$. The subscripts indicate the parallel wavevector of the incident light on the film at $z = 0$. The superscripts indicate the polarization and the propagation direction of the incident light. For example, the electric field $\widetilde{\boldsymbol{E}}^{(\alpha-)}_{(-\boldsymbol{\kappa},0)}$ in Eq. (2.39) results from the incident light that is α-polarized, propagating downward, and having parallel wavevector $-\boldsymbol{\kappa}$. Using Eq. (2.39), we obtain the transfer matrix as

$$M^{\alpha-}(-\boldsymbol{k}_\parallel - \boldsymbol{g}'_\parallel, -\boldsymbol{\kappa}; z', 0; \omega) = \frac{\widetilde{\boldsymbol{E}}^{(\alpha-)}_{(-\boldsymbol{\kappa},0)}(-\boldsymbol{k}_\parallel - \boldsymbol{g}'_\parallel, z', \omega)\widetilde{\boldsymbol{E}}^{\alpha-}_{inc}(-\boldsymbol{\kappa}, 0, \omega)}{[\widetilde{\boldsymbol{E}}^{\alpha-}_{inc}(-\boldsymbol{\kappa}, 0, \omega)]^2}. \tag{2.40}$$

Inserting Eqs. (2.30) and (2.40) into Eq. (2.38) and using (see Eq. (2.3))

$$\boldsymbol{E}^{(\alpha-)}_{-\boldsymbol{k}_\parallel(-\boldsymbol{\kappa},0)}(\boldsymbol{r}'_\parallel, z', \omega) = \sum_{\boldsymbol{g}'_\parallel} \widetilde{\boldsymbol{E}}^{(\alpha-)}_{(-\boldsymbol{\kappa},0)}(-\boldsymbol{k}_\parallel - \boldsymbol{g}'_\parallel, z', \omega) e^{-i(\boldsymbol{k}_\parallel + \boldsymbol{g}'_\parallel)\cdot \boldsymbol{r}'_\parallel}, \tag{2.41}$$

we obtain

$$\mathcal{P}^{\alpha+}(\boldsymbol{\kappa},\omega)=\frac{\hbar\omega^4}{8\pi^3c^3\cos\theta}\frac{1}{\int d\boldsymbol{r}_\parallel}\int_{-L}^{0}dz'\int d\boldsymbol{r}'_\parallel\frac{\varepsilon_I(\boldsymbol{r}'_\parallel,z',\omega)}{e^{\hbar\omega/kT(\boldsymbol{r}'_\parallel,z')}-1}\frac{|\boldsymbol{E}^{(\alpha-)}_{-\boldsymbol{k}_\parallel(-\boldsymbol{\kappa},0)}(\boldsymbol{r}'_\parallel,z',\omega)|^2}{|\widetilde{\boldsymbol{E}}^{\alpha-}(-\boldsymbol{\kappa},0,\omega)|^2},\tag{2.42}$$

where we suppressed the subscript *inc* on $\widetilde{\boldsymbol{E}}^{\alpha-}$. In Eq. (2.41) and (2.42), the electric field $\boldsymbol{E}^{(\alpha-)}_{-\boldsymbol{k}_\parallel(-\boldsymbol{\kappa},0)}$ has a parallel wavevector $-\boldsymbol{k}_\parallel$ in the first Brillouin zone and results from α-polarized light with parallel wavevector $-\boldsymbol{\kappa}$ incident on the $z=0$ plane. Because we assumed that the temperature distribution has the same periodicity as the structure, the integrations in Eq. (2.42) can be performed over a surface unit cell. Then Eq. (2.42) can be written as

$$\mathcal{P}^{\alpha+}(\boldsymbol{\kappa},\omega)=\frac{1}{S_{uc}\cos\theta}\int_{-L}^{0}dz'\int_{uc}d\boldsymbol{r}'_\parallel Q^{(\alpha-)}_{(-\boldsymbol{\kappa},0)}(\boldsymbol{r}'_\parallel,z',\omega)\mathcal{P}^{\alpha+}_{BB}(\boldsymbol{r}'_\parallel,z',\omega),\tag{2.43}$$

where S_{uc} is the area of the surface unit cell and $Q^{(\alpha-)}_{(-\boldsymbol{\kappa},0)}$ is the local absorption rate per unit volume when the film is irradiated with α-polarized light of unit intensity with parallel wavevector $-\boldsymbol{\kappa}$ incident on the $z=0$ plane. This absorption rate is given by [19]

$$Q^{(\alpha-)}_{(-\boldsymbol{\kappa},0)}(\boldsymbol{r}'_\parallel,z',\omega)=\frac{\omega}{c}\varepsilon_I(\boldsymbol{r}'_\parallel,z',\omega)\frac{|\boldsymbol{E}^{(\alpha-)}_{-\boldsymbol{k}_\parallel(-\boldsymbol{\kappa},0)}(\boldsymbol{r}'_\parallel,z',\omega)|^2}{|\widetilde{\boldsymbol{E}}^{\alpha-}(-\boldsymbol{\kappa},0,\omega)|^2}.\tag{2.44}$$

Finally, $\mathcal{P}^{\alpha+}_{BB}$ is the black-body radiation intensity for α-polarized light given by

$$\mathcal{P}^{\alpha+}_{BB}(\boldsymbol{r}'_\parallel,z',\omega)=\frac{\omega^2}{8\pi^3c^2}\frac{\hbar\omega}{e^{\hbar\omega/kT(\boldsymbol{r}'_\parallel,z')}-1}.\tag{2.45}$$

Equation (2.43) is the same as the Eq. (3.1) except for slight changes in notation [23]. When the temperature is uniform, $\mathcal{P}^{\alpha+}_{BB}$ is independent of the position and Eq. (2.43) becomes

$$\mathcal{P}^{\alpha+}(\boldsymbol{\kappa},\omega)=A^{(\alpha-)}(-\boldsymbol{\kappa},\omega)\mathcal{P}^{\alpha+}_{BB}(\omega),\tag{2.46}$$

where $A^{(\alpha-)}$ is the absorptivity for an α-polarized incident wave given by

$$A^{(\alpha-)}(-\boldsymbol{\kappa},\omega)=\frac{1}{S_{uc}\cos\theta}\int_{-L}^{0}dz'\int_{uc}d\boldsymbol{r}'_\parallel Q^{(\alpha-)}_{(-\boldsymbol{\kappa},0)}(\boldsymbol{r}'_\parallel,z',\omega).\tag{2.47}$$

Equation (2.46) is Kirchhoff's law for a periodically structured object with an arbitrary length scale. Thus, we proved that the Kirchhoff's law is obeyed for photonic crystal films if local equilibrium is assumed.

2.4 Optical Coherence for Photonic Crystals

The correlation between the electric fields of a given frequency at two different points is represented by the electric cross-spectral density tensor $W_{ij}^{(e)}$ defined in Eq. (1.56). This can be obtained from Eqs. (2.8) and (2.31) as

$$\begin{aligned} W_{ij}^{(e)}(\boldsymbol{r}_{\parallel 1}, \boldsymbol{r}_{\parallel 2}; z_1, z_2; \omega) &= \frac{\omega^3 \mu_0^2 \varepsilon_0}{\pi} \int d\boldsymbol{r}'_{\parallel} \int dz' \, \varepsilon_I(\boldsymbol{r}'_{\parallel}, z', \omega) \Theta(\omega, T(\boldsymbol{r}'_{\parallel}, z')) \\ &\quad \times \sum_k G_{ik}^*(\boldsymbol{r}_{\parallel 1}, \boldsymbol{r}'_{\parallel}; z_1, z'; \omega) G_{jk}(\boldsymbol{r}_{\parallel 2}, \boldsymbol{r}'_{\parallel}; z_2, z'; \omega). \end{aligned} \tag{2.48}$$

In Eq. (2.48), we assumed local equilibrium for non-uniform temperatures because the fluctuation-dissipation theorem was used. This is in general justified for high vacuum conditions as discussed in the Appendix of Chapter 3. The calculation of $W_{ij}^{(e)}$ for an arbitrary temperature distribution is formidable because of the integration in Eq. (2.48). However, if $f(\boldsymbol{r}'_{\parallel}, z', \omega) \equiv \varepsilon_I(\boldsymbol{r}'_{\parallel}, z', \omega)\Theta(\omega, T(\boldsymbol{r}'_{\parallel}, z'))$ is periodic in the xy plane, the calculation is simplified using Eq. (2.30). In this case, f can be expanded in a Fourier series as

$$f(\boldsymbol{r}'_{\parallel}, z', \omega) = \sum_{\boldsymbol{g}'_{\parallel}} \tilde{f}(\boldsymbol{g}'_{\parallel}, z') e^{i\boldsymbol{g}'_{\parallel} \cdot \boldsymbol{r}'_{\parallel}}. \tag{2.49}$$

Substituting Eq. (2.49) into Eq. (2.48) and using Eq. (2.23), we obtain

$$\begin{aligned} W_{ij}^{(e)}(\boldsymbol{r}_{\parallel 1}, \boldsymbol{r}_{\parallel 2}; z_1, z_2; \omega) &= \frac{\omega^3 \mu_0^2 \varepsilon_0}{\pi} \int dz' \sum_k \sum_{\alpha,\beta} \sum_{\boldsymbol{k}_{\parallel}} \sum_{\boldsymbol{g}_{\parallel 1}, \boldsymbol{g}'_{\parallel 1}} \sum_{\boldsymbol{g}_{\parallel 2}, \boldsymbol{g}'_{\parallel 2}} \tilde{f}(\boldsymbol{g}'_{\parallel 2} - \boldsymbol{g}'_{\parallel 1}, z') \\ &\quad \times \frac{e^{-i(\boldsymbol{k}_{\parallel} + \boldsymbol{g}_{\parallel 1}) \cdot \boldsymbol{r}_{\parallel 1} + i(\boldsymbol{k}_{\parallel} + \boldsymbol{g}_{\parallel 2}) \cdot \boldsymbol{r}_{\parallel 2}}}{4 k_{z,v}^*(\boldsymbol{k}_{\parallel} + \boldsymbol{g}_{\parallel 1}, \omega) k_{z,v}(\boldsymbol{k}_{\parallel} + \boldsymbol{g}_{\parallel 2}, \omega) \int d\boldsymbol{r}_{\parallel}} \\ &\quad \times e^{-ik_{z,v}^*(\boldsymbol{k}_{\parallel} + \boldsymbol{g}_{\parallel 1}, \omega) z_1 + ik_{z,v}(\boldsymbol{k}_{\parallel} + \boldsymbol{g}_{\parallel 2}, \omega) z_2} \end{aligned}$$

$$\times M_{ki}^{\alpha-*}(-\boldsymbol{k}_\parallel - \boldsymbol{g}'_{\parallel 1}, -\boldsymbol{k}_\parallel - \boldsymbol{g}_{\parallel 1}; z', 0; \omega)$$
$$\times M_{kj}^{\beta-}(-\boldsymbol{k}_\parallel - \boldsymbol{g}'_{\parallel 2}, -\boldsymbol{k}_\parallel - \boldsymbol{g}_{\parallel 2}; z', 0; \omega), \quad (2.50)$$

where β is the polarization defined similarly to α and we used

$$M(-\boldsymbol{k}_\parallel - \boldsymbol{g}'_\parallel, -\boldsymbol{k}_\parallel - \boldsymbol{g}_\parallel; z', z; \omega) = M(-\boldsymbol{k}_\parallel - \boldsymbol{g}'_\parallel, -\boldsymbol{k}_\parallel - \boldsymbol{g}_\parallel; z', 0; \omega) e^{ik_{z,v}(\boldsymbol{k}_\parallel + \boldsymbol{g}_\parallel, \omega) z} \quad (2.51)$$

and

$$\sum_{\boldsymbol{g}'_\parallel} \tilde{f}(\boldsymbol{g}'_\parallel, z') \delta_{\boldsymbol{g}'_\parallel + (\boldsymbol{k}_{\parallel 1} + \boldsymbol{g}'_{\parallel 1}) - (\boldsymbol{k}_{\parallel 2} + \boldsymbol{g}'_{\parallel 2}), 0} = \tilde{f}(\boldsymbol{g}'_{\parallel 2} - \boldsymbol{g}'_{\parallel 1}, z') \delta_{\boldsymbol{k}_{\parallel 1}, \boldsymbol{k}_{\parallel 2}}. \quad (2.52)$$

Thus the electric cross-spectral density tensor can be calculated from the knowledge of the transfer matrices using Eq. (2.50).

Now we wish to replace the transfer matrices by the electric fields as in the previous section. We replace $\boldsymbol{\kappa}$ in Eqs. (2.40) and (2.41) by $\boldsymbol{k}_\parallel + \boldsymbol{g}_{\parallel 1}$ and $\boldsymbol{k}_\parallel + \boldsymbol{g}_{\parallel 2}$ and substitute the resulting equations into Eq. (2.50) to obtain

$$\begin{aligned} W_{ij}^{(e)}(\boldsymbol{r}_{\parallel 1}, \boldsymbol{r}_{\parallel 2}; z_1, z_2; \omega) \;=\; & \frac{\omega^3 \mu_0^2 \varepsilon_0}{\pi} \int d\boldsymbol{r}'_\parallel \int dz' \sum_{\alpha,\beta} \sum_{\boldsymbol{k}_\parallel} \sum_{\boldsymbol{g}_{\parallel 1}, \boldsymbol{g}_{\parallel 2}} \\ & \times \frac{\varepsilon_I(\boldsymbol{r}'_\parallel, z', \omega) \Theta(\omega, T(\boldsymbol{r}'_\parallel, z'))}{4 k_{z,v}^*(\boldsymbol{k}_\parallel + \boldsymbol{g}_{\parallel 1}, \omega) k_{z,v}(\boldsymbol{k}_\parallel + \boldsymbol{g}_{\parallel 2}, \omega) \left(\int d\boldsymbol{r}_\parallel\right)^2} \\ & \times e^{-i(\boldsymbol{k}_\parallel + \boldsymbol{g}_{\parallel 1}) \cdot \boldsymbol{r}_{\parallel 1} + i(\boldsymbol{k}_\parallel + \boldsymbol{g}_{\parallel 2}) \cdot \boldsymbol{r}_{\parallel 2}} \\ & \times e^{-ik_{z,v}^*(\boldsymbol{k}_\parallel + \boldsymbol{g}_{\parallel 1}, \omega) z_1 + ik_{z,v}(\boldsymbol{k}_\parallel + \boldsymbol{g}_{\parallel 2}, \omega) z_2} \\ & \times \boldsymbol{E}^{(\alpha-)}_{-\boldsymbol{k}_\parallel (-\boldsymbol{k}_\parallel - \boldsymbol{g}_{\parallel 1}, 0)}{}^{*}(\boldsymbol{r}'_\parallel, z', \omega) \cdot \boldsymbol{E}^{(\beta-)}_{-\boldsymbol{k}_\parallel (-\boldsymbol{k}_\parallel - \boldsymbol{g}_{\parallel 2}, 0)}(\boldsymbol{r}'_\parallel, z', \omega) \\ & \times \frac{\widetilde{E}_i^{\alpha-*}(-\boldsymbol{k}_\parallel - \boldsymbol{g}_{\parallel 1}, 0, \omega) \widetilde{E}_j^{\beta-}(-\boldsymbol{k}_\parallel - \boldsymbol{g}_{\parallel 2}, 0, \omega)}{\widetilde{\boldsymbol{E}}^{\alpha-*2}(-\boldsymbol{k}_\parallel - \boldsymbol{g}_{\parallel 1}, 0, \omega) \widetilde{\boldsymbol{E}}^{\beta-2}(-\boldsymbol{k}_\parallel - \boldsymbol{g}_{\parallel 2}, 0, \omega)}, \end{aligned} \quad (2.53)$$

where we removed $\tilde{f}$ using Eq. (2.30). Eq. (2.53) is the general equation that describes the correlations of any two points over periodic structures with a periodic temperature distribution. The location of the two points can be in the near-field where evanescent fields exist.

Often, we are interested in the coherence on a plane that is parallel to the surface of the film and in the far-field. In this case, the coherence is related to the angular

dependence of the thermal emission as discussed in section 1.3. We set $z_1 = z_2 = z$ and assume that z is large such that $k_{zI,v}z \gg 1$ for all $\boldsymbol{g}_\parallel$'s, where $k_{zI,v}$ is the imaginary part of $k_{z,v}$. We also assume that the temperature is uniform and the wavelength is larger than the periodicity of the structure. For this wavelength, only zero-order reflections occur for an incident light. With these assumptions, Eq. (2.53) is reduced to

$$\begin{aligned} W_{ij}^{(e)}(\boldsymbol{R}_\parallel, z, \omega) &= \frac{\omega\mu_0}{\pi}\int_{uc} d\boldsymbol{r}'_\parallel \int dz' \sum_{\alpha,\beta}\sum_{\boldsymbol{k}_\parallel} \varepsilon_I(\boldsymbol{r}'_\parallel, z', \omega)\Theta(\omega, T) \\ &\times \frac{e^{i\boldsymbol{k}_\parallel\cdot\boldsymbol{R}_\parallel}}{4\cos^2\theta \int d\boldsymbol{r}_\parallel \int_{uc} d\boldsymbol{r}_\parallel} \\ &\times \boldsymbol{E}^{(\alpha-)}_{-\boldsymbol{k}_\parallel(-\boldsymbol{k}_\parallel,0)}{}^{*}(\boldsymbol{r}'_\parallel, z', \omega)\cdot \boldsymbol{E}^{(\beta-)}_{-\boldsymbol{k}_\parallel(-\boldsymbol{k}_\parallel,0)}(\boldsymbol{r}'_\parallel, z', \omega) \\ &\times \frac{\widetilde{E}_i^{\alpha-*}(-\boldsymbol{k}_\parallel, 0, \omega)\widetilde{E}_j^{\beta-}(-\boldsymbol{k}_\parallel, 0, \omega)}{\widetilde{\boldsymbol{E}}^{\alpha-*2}(-\boldsymbol{k}_\parallel, 0, \omega)\widetilde{\boldsymbol{E}}^{\beta-2}(-\boldsymbol{k}_\parallel, 0, \omega)}, \end{aligned} \tag{2.54}$$

where $\boldsymbol{R}_\parallel = \boldsymbol{r}_{\parallel 2} - \boldsymbol{r}_{\parallel 1}$, $|\boldsymbol{k}_\parallel| \le \omega/c$, and we used $k_{z,v}(-\boldsymbol{k}_\parallel, \omega) = \frac{\omega}{c}\cos\theta$. Note that $W_{ij}^{(e)}$ depends only on the difference in the position in this case. The trace of $W^{(e)}$ in Eq. (2.54) becomes

$$\begin{aligned} \mathrm{Tr}W^{(e)}(\boldsymbol{R}_\parallel, z, \omega) &= \frac{\omega\mu_0}{\pi}\int_{uc} d\boldsymbol{r}'_\parallel \int dz'\, \varepsilon_I(\boldsymbol{r}'_\parallel, z', \omega)\Theta(\omega, T) \\ &\times \sum_{\boldsymbol{k}_\parallel}\sum_{\alpha} \frac{e^{i\boldsymbol{k}_\parallel\cdot\boldsymbol{R}_\parallel}}{4\cos^2\theta \int d\boldsymbol{r}_\parallel \int_{uc} d\boldsymbol{r}_\parallel} \frac{|\boldsymbol{E}^{(\alpha-)}_{-\boldsymbol{k}_\parallel(-\boldsymbol{k}_\parallel,0)}(\boldsymbol{r}'_\parallel, z', \omega)|^2}{|\widetilde{\boldsymbol{E}}^{\alpha-}(-\boldsymbol{k}_\parallel, 0, \omega)|^2}, \end{aligned} \tag{2.55}$$

where we used the fact that $\hat{\boldsymbol{\alpha}}_{-\boldsymbol{k}_\parallel,-}$ is real. Using the absorptance $A = \sum_\alpha A^{(\alpha-)}/2$ defined in Eq. (2.47), Eq. (2.55) can be written as

$$\mathrm{Tr}W^{(e)}(\boldsymbol{R}_\parallel, z, \omega) = \frac{c\mu_0\Theta(\omega, T)}{2\pi\int d\boldsymbol{r}_\parallel}\sum_{\boldsymbol{k}_\parallel}\frac{A(-\boldsymbol{k}_\parallel, \omega)}{\cos\theta}e^{i\boldsymbol{k}_\parallel\cdot\boldsymbol{R}_\parallel}. \tag{2.56}$$

Equation (2.56) indicates that, apart from a constant factor, the coherence function $\mathrm{Tr}W^{(e)}$ is equal to the Fourier transform of $A/\cos\theta$. This is similar to Eq. (1.58). Conversely, the absorptance A can be obtained in terms of the coherence function $\mathrm{Tr}W^{(e)}$

by the inverse Fourier transform as

$$A(-\boldsymbol{k}_{\parallel},\omega)=\frac{2\pi c\cos\theta}{\omega^2\mu_0\Theta(\omega,T)}\int d\boldsymbol{R}_{\parallel}\mathrm{Tr}W^{(e)}(\boldsymbol{R}_{\parallel},z,\omega)e^{-i\boldsymbol{k}_{\parallel}\cdot\boldsymbol{R}_{\parallel}}. \tag{2.57}$$

An analytical expression for $\mathrm{Tr}W^{(e)}$ is obtained for a black-body. In Eq. (2.56), setting $A=1$ and using $\cos\theta=\frac{c}{\omega}k_{z,v}(\boldsymbol{k}_{\parallel},\omega)$ from Eq. (2.17), we have

$$\begin{aligned}\mathrm{Tr}W^{(e)}(\boldsymbol{R}_{\parallel},z,\omega) &= \frac{c\mu_0\Theta(\omega,T)}{2\pi\int d\boldsymbol{r}_{\parallel}}\sum_{\boldsymbol{k}_{\parallel}}\frac{e^{i\boldsymbol{k}_{\parallel}\cdot\boldsymbol{R}_{\parallel}}}{\sqrt{\frac{\omega^2}{c^2}-|\boldsymbol{k}_{\parallel}|^2}}\\ &= \frac{c\mu_0\Theta(\omega,T)}{8\pi^3}\int_{k_{\parallel}<\frac{\omega}{c}}d\boldsymbol{k}_{\parallel}\frac{e^{i\boldsymbol{k}_{\parallel}\cdot\boldsymbol{R}_{\parallel}}}{\sqrt{\frac{\omega^2}{c^2}-k_{\parallel}^2}}\\ &= \frac{c\mu_0\Theta(\omega,T)}{4\pi^2}\frac{\sin\rho}{\rho},\end{aligned} \tag{2.58}$$

where $\rho=\frac{\omega}{c}R_{\parallel}$. In Eq. (2.58), the transition from summation to integral is valid when the linear dimension of the black-body is much larger than the wavelength $\lambda=2\pi c/\omega$. Equation (2.58) agrees with Ref. [24] and shows that the coherence length of a black-body is of the order of λ. Note that in general $W_{ij}^{(e)}$ in Eq. (2.54) cannot be obtained in terms of $A^{(\alpha-)}$ because the electric fields resulting from incident s- and p-polarized light ($\boldsymbol{E}^{(s-)}$ and $\boldsymbol{E}^{(p-)}$) are not necessarily orthogonal in the photonic crystal. This is possible only when they are orthogonal as in a homogeneous flat film. However, $\mathrm{Tr}W^{(e)}$ can be expressed in terms of A for photonic crystals as seen in Eq. (2.56). Equation (2.56) shows that $\mathrm{Tr}W^{(e)}$ is in general a complex number. This can be real if $A(-\boldsymbol{k}_{\parallel},\omega)=A(\boldsymbol{k}_{\parallel},\omega)$ which happens for structures with mirror symmetry. However, even in this case, $\mathrm{Tr}W^{(e)}$ in the near-field is in general complex.

Using Eq. (2.56) and the transfer matrix method [25], we calculated $\mathrm{Tr}W^{(e)}$ for the SiC grating reported in Ref. [26]. At $\lambda=11.36\ \mu m$, surface phonon polaritons can be excited on the SiC film and coupled to light by the grating. Because the surface phonon polaritons can propagate a long distance, it was shown that the coherence length was large. This coherence has already been calculated in Ref. [27], but only the contributions from the surface phonon polaritons were considered. Here we investigate the coherence

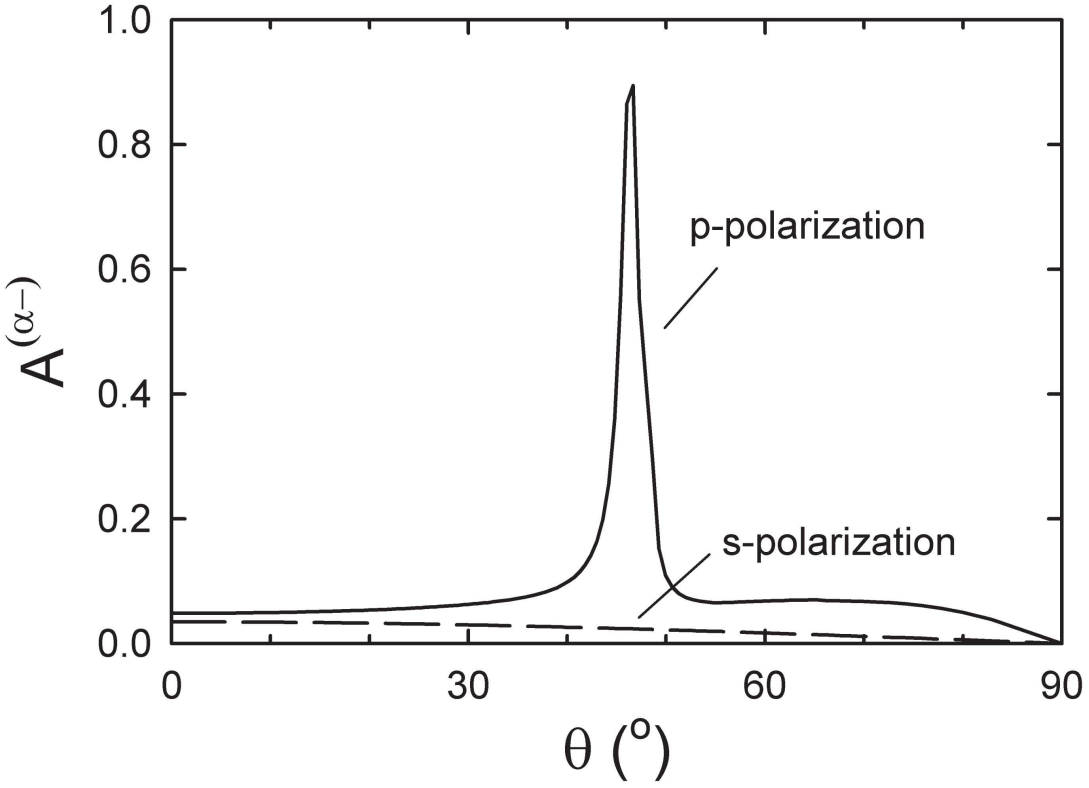

Figure 2.1: Angular dependence of the absorptance of a SiC linear grating for s- and p-polarizations at $\lambda = 11.36\ \mu m$. The groove period, width, and depth are 6.248 μm, 3.79 μm, and 250 nm, respectively. θ is the angle from the surface normal in the plane perpendicular to the grating direction.

considering all the propagating fields. The structural parameters were slightly modified such that the groove period, width, and depth are 6.248 μm, 3.79 μm, and 250 nm, respectively.

Figure 2.1 shows the calculated absorptance for s- and p-polarizations as a function of the inclination angle θ from the surface normal. We set the Cartesian coordinate system such that the y axis is the direction in which the grating is ruled and the z axis is normal to the surface. The inclination angle is in the xz plane. The peak in the p-polarization is due to the surface phonon polaritons. The peak width is about 2.5° and the approximate formula for the coherence length l

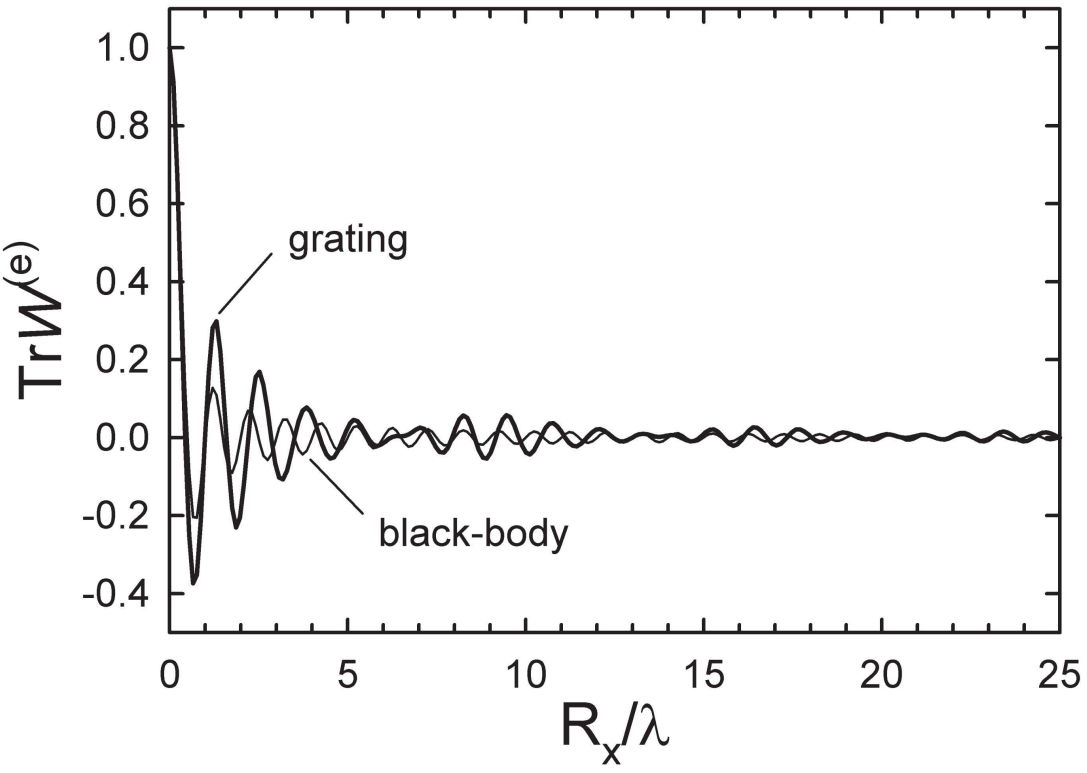

Figure 2.2: Normalized electric coherence $\mathrm{Tr}W^{(e)}$ as a function of the separation of the two points at $\lambda = 11.36$ μm in the far-field of the grating in Fig. 2.1. The distance between the two points (R_x) is normalized to the wavelength λ.

$$l \sim \frac{\lambda}{\Delta\theta \cos\theta} \tag{2.59}$$

yields $l \sim 32\lambda$. However, the coherence calculated from Eq. (2.56) shown in Fig. 2.2 shows that the coherence length is much shorter. In Fig. 2.2, $\mathrm{Tr}W^{(e)}$ is normalized to its value at $R_x = 0$. The envelope of the normalized $\mathrm{Tr}W^{(e)}$ decays to $1/e$ at $\sim \lambda$. Thus the coherence length is $\sim \lambda$ even though the thermal emission is highly directional. This is partly due to the contributions of the modes that are not related to the surface phonon polaritons. These contributions are also manifested in the oscillating features with a periodicity of $\sim \lambda$ in Fig. 2.2. These features are present in the $\mathrm{Tr}W^{(e)}$ of a black-body as shown as a dashed line in Fig. 2.2. However, this periodicity of $\sim \lambda$ is also contributed by the surface phonon polaritons. The peak in Fig. 2.1 at $\theta = 46.7°$ corresponds to $k_x a_x/2\pi = 0.4$ where a_x is the grating period. At this wavevector, the expected period in $\mathrm{Tr}W^{(e)}$ is $R_x/\lambda = 1.375$ from Eq. (2.56) if only the peak in Fig. 2.1 is considered. We also observe in Fig. 2.2 the beats with a period $R_x/\lambda \sim 9$. This cannot be explained by the surface phonon polariton modes in Fig. 2.1 or other modes different from surface phonon polaritons. The surface phonon polaritons couple to the light not only in the xz plane but also in all the other planes perpendicular to the surface. These surface phonon polaritons have different wavevectors than $k_{\|}a_x/2\pi = 0.4$ and contribute to the beats in Fig. 2.2. The exact locations of $\boldsymbol{k}_{\|}$ can be found in Ref. [28]. Because these $\boldsymbol{k}_{\|}$'s cover a broad range, this also contributes to the short coherence length in Fig. 2.2. Therefore, the large difference in the coherence length between Eq. (2.59) and Fig. 2.2 comes partly from the fact that Eq. (2.59) considers only the surface phonon polaritons in the xz plane.

In Ref. [27], the coherence length of a grating shorter than that of a flat film was attributed solely to the radiative losses. However, we find that the surface phonon polaritons with a range of wavevectors couple to the light for the grating and this is the main reason for the decrease in the coherence length. In this case, many different wavevectors are summed up in Eq. (2.56) resulting in dephasing which implies a decrease

in the coherence length. The range of wavevectors is the consequence of the directional momentum transfer from the grating to the surface phonon polaritons. If we consider only the surface phonon polaritons of the wavevectors in the x direction, Eq. (2.56) yields $l \sim 32\lambda$ which agrees with the prediction of Eq. (2.59) and is not very different from $l \sim 36\lambda$ predicted for a flat film. When we considered all the surface phonon polariton modes excluding the background emission, the calculated coherence was $l \sim 5\lambda$ (not shown). Therefore we conclude that the main reason for the decrease of the coherence length for the grating is not the radiation damping but the momentum transfer in the x direction from the grating. If the grating has a cylindrical symmetry as in a bull's eye pattern, the momentum transfer occurs in the radial direction. Further, if the resulting momentum of the light is such that $\boldsymbol{k}_{\parallel} \simeq 0$, the coherence length due to the surface polaritons does not decrease by the momentum transfer because a very narrow range of wavevectors is involved. In this case, the light due to the surface polaritons will be beaming in the direction of surface normal [29]. This will be discussed further in Chapter 5.

The calculation of coherence in the near-field can be demanding even for simple structures. This is because large parallel wavevectors contribute to the coherence significantly in the near-field. To see this more clearly, we note that Eq. (2.53) contains a factor $\exp[-k_{zI,v}z]$. From Eq. (2.17), $k_{zI,v}(\boldsymbol{k}_{\parallel} + \boldsymbol{g}_{\parallel}, \omega)$ increases as $|\boldsymbol{k}_{\parallel} + \boldsymbol{g}_{\parallel}|$ increases. When z is not small, the contributions of large $|\boldsymbol{k}_{\parallel} + \boldsymbol{g}_{\parallel}|$'s become negligible because $\exp[-k_{zI,v}z]$ becomes small. Thus, in this case, we do not need large $|\boldsymbol{g}_{\parallel}|$'s in numerical calculations. However, when z is small, we need to include many terms in the summation over $\boldsymbol{g}_{\parallel}$'s in Eq. (2.53), which leads to a large computation time. However, these calculations are suitable for a parallel computing approach because the calculations for each $\boldsymbol{g}_{\parallel}$ can be done in parallel. Here we present calculations of optical coherence in the near-field over a periodic structure. The grating used in the calculations is the same as the one in Fig. 2.1. In such structures with a mirror symmetry, the summation in $\boldsymbol{k}_{\parallel}$ can be done only for $k_x \geq 0$. Because of a large computation time in the near-field

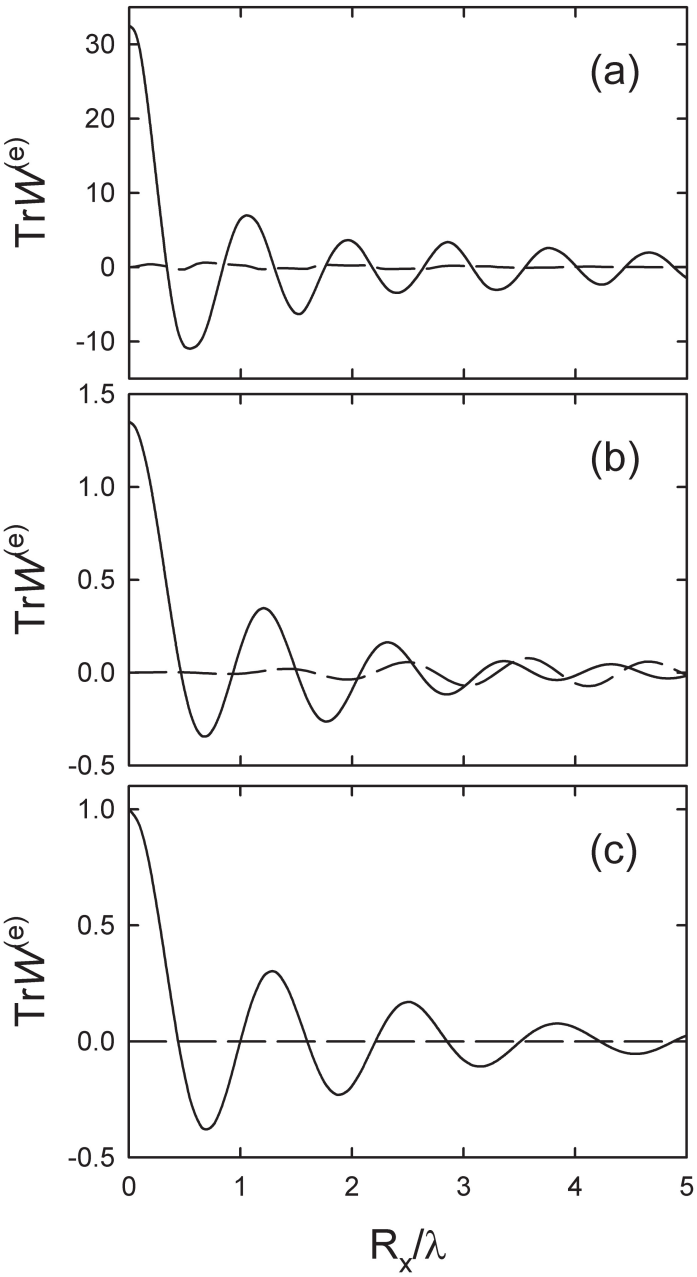

Figure 2.3: Real (solid line) and imaginary (dashed line) part of the electric coherence $\mathrm{Tr}W^{(e)}$ as a function of the separation of the two points at $\lambda = 11.36\ \mu m$ in the near-field at (a) $z = 0.1\lambda$, (b) $z = \lambda$, and (c) $z = 10\lambda$ of the grating in Fig. 2.1. $\mathrm{Tr}W^{(e)}$'s are normalized to their value at $R_x = 0$ and $z = 10\lambda$. The distance between the two points (R_x) is normalized to the wavelength λ.

calculations, we investigate the coherence on the planes at $z \geq 0.1\lambda$. Figure 2.3 shows $\mathrm{Tr}W^{(e)}$ for the grating at $z = 0.1\lambda$, λ, and 10λ. All $\mathrm{Tr}W^{(e)}$'s are normalized to their values for $R_x = 0$ at $z = 10\lambda$. At $z = 10\lambda$, the evanescent field is almost absent and the coherence is very similar to Fig. 2.2. $\mathrm{Tr}W^{(e)}$ is almost real at this far-field. However, at $z = 0.1\lambda$ and λ, we observe that $\mathrm{Tr}W^{(e)}$, which is real for a flat surface, is now complex. Moreover, the imaginary part does not necessarily decrease as z increases even though it disappears for a sufficiently large z. The period of the oscillation in $\mathrm{Tr}W^{(e)}$ decreases as z decreases, which indicates that large wavevectors become important as the surface is approached. $W^{(e)}_{yy}$, which is associated with the fields polarized in the grating direction, behaves similar to the black-body at the range of z's investigated (not shown). This indicates that the large coherence length in Fig. 2.3 is mainly due to the surface phonon polaritons which are p-polarized.

The electric energy density is proportional to $\mathrm{Tr}W^{(e)}$ for $R_x = 0$. In Fig. 2.3, we can see that the electric energy density increases as z decreases. It is well known that, for a flat surface, the electric energy density decreases with increasing z as $1/z^3$ in the near-field [16, 17]. However, this is not in general true for photonic crystals. To see this more clearly, we set $\boldsymbol{r}_{\parallel 1} = \boldsymbol{r}_{\parallel 2}$ and $z = z_1 = z_2$ in Eq. (2.53) and define the electric energy density averaged over a unit cell $\bar{u}^{(e)}$ as

$$\bar{u}^{(e)}(z,\omega) = \frac{1}{\int_{uc} d\boldsymbol{r}_\parallel} \int_{uc} d\boldsymbol{r}_\parallel \sum_i W^{(e)}_{ii}(\boldsymbol{r}_\parallel, \boldsymbol{r}_\parallel; z, z; \omega). \tag{2.60}$$

Substitution of Eq. (2.53) for a uniform temperature into Eq. (2.60) yields

$$\bar{u}^{(e)}(z,\omega) = \frac{\omega\mu_0\Theta}{4\pi \int d\boldsymbol{r}_\parallel} \sum_{\alpha,\beta} \sum_{\boldsymbol{k}_\parallel} \sum_{\boldsymbol{g}_\parallel} \frac{e^{-2k_{zI,v}(\boldsymbol{k}_\parallel + \boldsymbol{g}_\parallel, \omega)z}}{|k_{z,v}(\boldsymbol{k}_\parallel + \boldsymbol{g}_\parallel, \omega)|} A^{(\alpha\beta--)}(-\boldsymbol{k}_\parallel - \boldsymbol{g}_\parallel, \omega), \tag{2.61}$$

where the generalized absorptance $A^{(\alpha\beta--)}$ is defined similarly to Eq. (2.47) as

$$A^{(\alpha\beta--)}(-\boldsymbol{k}_\parallel - \boldsymbol{g}_\parallel, \omega) = \frac{\omega}{c|k_{z,v}(\boldsymbol{k}_\parallel + \boldsymbol{g}_\parallel, \omega)| \int_{uc} d\boldsymbol{r}_\parallel} \int dz' \int_{uc} d\boldsymbol{r}'_\parallel Q^{(\alpha\beta--)}_{(-\boldsymbol{k}_\parallel - \boldsymbol{g}_\parallel, 0)}(\boldsymbol{r}'_\parallel, z', \omega) \tag{2.62}$$

and the generalized absorption rate per unit volume $Q^{(\alpha\beta--)}_{(-\boldsymbol{k}_\parallel-\boldsymbol{g}_\parallel,0)}$ is

$$\begin{aligned} Q^{(\alpha\beta--)}_{(-\boldsymbol{k}_\parallel-\boldsymbol{g}_\parallel,0)}(\boldsymbol{r}'_\parallel,z',\omega) &= \frac{\omega}{c}\varepsilon_I(\boldsymbol{r}'_\parallel,z',\omega) \\ &\times \boldsymbol{E}^{(\alpha-)}_{-\boldsymbol{k}_\parallel(-\boldsymbol{k}_\parallel-\boldsymbol{g}_\parallel,0)}{}^{*}(\boldsymbol{r}'_\parallel,z',\omega)\cdot\boldsymbol{E}^{(\beta-)}_{-\boldsymbol{k}_\parallel(-\boldsymbol{k}_\parallel-\boldsymbol{g}_\parallel,0)}(\boldsymbol{r}'_\parallel,z',\omega) \\ &\times \frac{\widetilde{\boldsymbol{E}}^{\alpha-*}(-\boldsymbol{k}_\parallel-\boldsymbol{g}_\parallel,0,\omega)\cdot\widetilde{\boldsymbol{E}}^{\beta-}(-\boldsymbol{k}_\parallel-\boldsymbol{g}_\parallel,0,\omega)}{\widetilde{\boldsymbol{E}}^{\alpha-*2}(-\boldsymbol{k}_\parallel-\boldsymbol{g}_\parallel,0,\omega)\widetilde{\boldsymbol{E}}^{\beta-2}(-\boldsymbol{k}_\parallel-\boldsymbol{g}_\parallel,0,\omega)}. \end{aligned} \tag{2.63}$$

$Q^{(\alpha\beta--)}_{(-\boldsymbol{k}_\parallel-\boldsymbol{g}_\parallel,0)}$ is the local absorption rate per unit volume for the two sources that have polarizations α and β and the same parallel wavevector $-\boldsymbol{k}_\parallel-\boldsymbol{g}_\parallel$ at $z=0$. $A^{(\alpha\beta--)}$ is the corresponding absorptance. When $1/z \gg \omega/c$, it follows from Eq. (2.61) that

$$\bar{u}^{(e)}(z,\omega) \propto \int_0^\infty dq_\parallel \left[\frac{\sum_{\alpha,\beta}\int_0^{2\pi} d\phi A^{(\alpha\beta--)}(-\boldsymbol{q}_\parallel,\omega)}{|k_{z,v}(q_\parallel,\omega)|}\right] q_\parallel e^{-2q_\parallel z}, \tag{2.64}$$

where $\boldsymbol{q}_\parallel = \boldsymbol{k}_\parallel + \boldsymbol{g}_\parallel$ and ϕ is the azimuthal angle on the xy plane. For a flat surface, the factor in the bracket in Eq. (2.64) is proportional to $q_\parallel$ and $\bar{u}^{(e)} \propto 1/z^3$ in the near-field [17]. However, this does not happen in general for periodic structures. Therefore, the near-field heat transport can be modified when a uniform film is periodically structured.

2.5 Conclusion

We have shown using fluctuational electrodynamics that thermal emission in the far-field of photonic crystals obeys Kirchhoff's law. This does not assume that the photonic crystals are in thermal equilibrium with the radiation field, but the material components should be in thermal equilibrium. Our proof is applicable to any photonic crystal structure. Thus, in the study of thermal emission, we can avoid the direct calculation of thermal emission from photonic crystals which is computationally intensive [13]. Our formulation of fluctuational electrodynamics provides a comprehensive study of thermal emission from photonic crystals both in the far-field and the near-field. The coherence in the far-field of a linear grating that supports surface polaritons is not much improved in comparison to the flat surface due to two reasons: (1) the directional momentum

transfer from the grating to the surface polaritons and (2) the modes that are not related to the surface polaritons. These two lead to the far-field coherence length of $\sim \lambda$ which is not much different from the black-body. The thermal near-field behavior of photonic crystals is shown to be different from a uniform film. This implies that near-field heat transport can be controlled by using photonic crystals.

References

[1] S. John and R. Wang, "Metallic photonic-band-gap filament architectures for optimized incandescent lighting," Phys. Rev. A **78**, 043809 (2008).

[2] Y. De Wilde, F. Formanek, R. Carminati, B. Gralak, P. A. Lemoine, K. Joulain, J. P. Mulet, Y. Chen, and J. J. Greffet, "Thermal radiation scanning tunnelling microscopy," Nature **444**, 740-743 (2006).

[3] S.-Y. Lin, J. Moreno, and J. G. Fleming, "Three-dimensional photonic-crystal emitter for thermal photovoltaic power generation," Appl. Phys. Lett. **83**, 380-382 (2003).

[4] P. Nagpal, S. E. Han, A. Stein, and D. J. Norris, "Efficient low-temperature thermophotovoltaic emitters from metallic photonic crystals," Nano Lett. **8**, 3238-3243 (2008).

[5] C. M. Cornelius and J. P. Dowling, "Modification of Planck blackbody radiation by photonic band-gap structures," Phys. Rev. A **59**, 4736-4746 (1999).

[6] J. G. Fleming, S.-Y. Lin, I. El-Kady, R. Biswas, and K. M. Ho, "All-metallic three-dimensional photonic crystals with a large infrared bandgap," Nature **417**, 52-55 (2002).

[7] S. E. Han, A. Stein, and D. J. Norris, "Tailoring self-assembled metallic photonic crystals for modified thermal emission," Phys. Rev. Lett. **99**, 053906 (2007).

[8] J. D. Joannopoulos, P. R. Villeneuve, and S. Fan, "Photonic crystals: Putting a new twist on light," Nature **386**, 143-149 (1997).

[9] T. Trupke, P. Wurfel, and M. A. Green, "Comment on 'Three-dimensional photonic-crystal emitter for thermal photovoltaic power generation' [Appl. Phys. Lett. 83, 380 (2003)]," Appl. Phys. Lett. **84**, 1997-1998 (2004).

[10] S.-Y. Lin, J. Moreno, and J. G. Fleming, "Response to 'Comment on 'Three-dimensional photonic-crystal emitter for thermal photovoltaic power generation' '[Appl. Phys. Lett. **84**, 1997 (2004)]," Appl. Phys. Lett. **84**, 1999 (2004).

[11] I. El-Kady, W. W. Chow, and J. G. Fleming, "Emission from an active photonic crystal," Phys. Rev. B **72**, 195110 (2005).

[12] W. W. Chow, "Theory of emission from an active photonic lattice," Phys. Rev. A **73**, 013821 (2006).

[13] C. Luo, A. Narayanaswamy, G. Chen, and J. D. Joannopoulos, "Thermal radiation from photonic crystals: A direct calculation," Phys. Rev. Lett. **93**, 213905 (2004).

[14] J. G. Fleming, "Addendum: 'Three-dimensional photonic-crystal emitter for thermal photovoltaic power generation' [Appl. Phys. Lett. 83, 380 (2003)]," Appl. Phys. Lett. **86**, 249902 (2005).

[15] C. H. Seager, M. B. Sinclair, and J. G. Fleming, "Accurate measurements of thermal radiation from a tungsten photonic lattice," Appl. Phys. Lett. **86**, 244105 (2005).

[16] S. M. Rytov, Y. A. Kravtsov, and V. I. Tatarskii, *Principles of statistical radiophysics, Vol. 3: Elements of random fields* (Springer-Verlag, Berlin, 1989).

[17] C. Henkel, K. Joulain, R. Carminati, and J.-J. Greffet, "Spatial coherence of thermal near fields," Opt. Commun. **186**, 57-67 (2000).

[18] C. T. Tai, *Dyadic green functions in electromagnetic theory*, 2nd ed. (IEEE Press, New York, 1994), Section 4-5.

[19] L. D. Landau and E. M. Lifshitz, *Electrodynamics of continuous media*, 2nd ed. (Pergamon, Oxford, 1984).

[20] J. E. Sipe, "New Green-function formalism for surface optics," J. Opt. Soc. Am. B **4**, 481-489 (1987).

[21] L. Mandel and E. Wolf, *Optical coherence and quantum optics* (Cambridge University Press, Cambridge, 1995), Section 3.3.

[22] L. D. Landau and E. M. Lifshitz, *Statistical physics, Part 1* (Pergamon, Oxford, 1984), Section 58.

[23] S. E. Han and D. J. Norris, "Control of thermal emission by selective heating of periodic structures," Phys. Rev. Lett. (submitted).

[24] C. L. Mehta and E. Wolf, "Coherence properties of blackbody radiation. III. Cross-spectral tensors," Phys. Rev. **161**, 1328-1334 (1967).

[25] J. B. Pendry and A. MacKinnon, "Calculation of photon dispersion relations," Phys. Rev. Lett. **69**, 2772-2775 (1992).

[26] J.-J. Greffet, R. Carminati, K. Joulain, J. P. Mulet, S. Mainguy, and Y. Chen, "Coherent emission of light by thermal sources," Nature (London) **416**, 61-64 (2002).

[27] F. Marquier, K. Joulain, J.-P. Mulet, R. Carminati, and J.-J. Greffet, "Coherent spontaneous emission of light by thermal sources," Phys. Rev. B **69**, 155412 (2004).

[28] F. Marquier, C. Arnold, M. Laroche, J.-J. Greffet, and Y. Chen, "Degree of polarization of thermal light emitted by gratings supporting surface waves," Opt. Express **16**, 5305-5313 (2008).

[29] S. E. Han, P. Nagpal, and D. J. Norris, "Beaming thermal emission from hot metallic bull's eyes," Phys. Rev. Lett. (submitted).

Chapter 3

Control of Thermal Emission by Selective Heating of Periodic Structures*

"Where is the way where light dwelleth?
and as for darkness, where is the place thereof,
That thou shouldest take it to the bound thereof,
and that thou shouldest know the paths to the house thereof?"

Job 38:19-20

3.1 Introduction

When a material is structured on a micrometer length scale, its thermal emission spectrum can be modified. This can occur due to excitation of optical modes on patterned surfaces [1, 2, 3] or due to optical diffraction in three-dimensionally periodic solids known as photonic crystals [4, 5, 6]. By utilizing these effects, heated structures can exhibit

* Much of Chapter 3 will appear in print: S. E. Han and D. J. Norris, Phys. Rev. Lett. (submitted).

thermal emission over a relatively narrow spectral range, instead of a broad black-body-like peak. This may lead to efficient light sources, new thermophotovoltaic devices [7, 8], and unexpected physical phenomena. However, so far, investigations have been limited to structures that are homogeneously heated. In this case, all electromagnetic modes that conserve energy and can couple to propagating modes in the far-field will emit. If instead, heat is applied inhomogenously, additional control over the emission might be possible. Consider monochromatic light coupled from the far field into a photonic crystal with a lattice parameter comparable to the optical wavelength. Diffraction will concentrate this electromagnetic wave at specific locations within the unit cell, analogous to spatial variations in the electronic wave functions of atomic crystals [9]. If this photonic crystal were heated periodically with the same pattern, a specific frequency might be selected for thermal emission. Thus, depending on where the heat is applied within the unit cell, spectral control over the thermal emission might be obtained.

In this chapter, we examine this simple and surprisingly unexplored possibility. Because Kirchoff's law, which is the typical starting point for modeling thermal emission, is not applicable when local temperature variations exist, we use instead the reciprocity theorem of electrodynamics. It roughly states that a fluctuating current and the electric field that it creates at a distant location can be interchanged without affecting their relationship [10, 11]. Thus, if an external field of a specific frequency is concentrated within the structure, oscillating dipoles placed at the same locations will lead to strong emission at this frequency. Below we combine the reciprocity theorem with the fluctuation-dissipation theorem and examine structures in which the absorptivity periodically varies in space. We show that thermal emission can be controlled depending on how the heat is applied within the unit cell. For example, numerical calculations for a two-component structure show that one can choose between two emission frequencies depending on which component is heated. Thus, we confirm that nonuniform heating can provide new control over thermal emission.

3.2 Formulation

To begin, we derive an expression for the emission intensity $\mathcal{P}$ emanating from a thin photonic film consisting of periodically placed components. The film lies in the xy plane with a finite thickness in z. We first make an important assumption, addressed further below, that the fluctuation-dissipation theorem is valid locally. Maxwell's equations can then be solved for thermal emission propagating away from the structure at an angle θ from the z axis. The emission rate per unit solid angle per unit frequency per unit area is

$$\mathcal{P}^{\alpha+}_{+\boldsymbol{\kappa}} = \frac{\int_{S_{uc}} d\boldsymbol{r}_{\parallel} \int dz Q^{\alpha-}_{-\boldsymbol{\kappa}}(\boldsymbol{r}_{\parallel}, z) \mathcal{P}^{\alpha+}_{BB}(\boldsymbol{r}_{\parallel}, z)}{S_{uc} \cos\theta}. \tag{3.1}$$

A detailed derivation of Eq. (3.1) can be found in Chapter 2. Here α designates the polarization of the light (TE or TM) while $+$ and $-$ indicate whether the light is propagating away from or toward the film, respectively. S_{uc} is the area of a two-dimensional unit cell in the xy plane, and $\boldsymbol{\kappa}$ and $\boldsymbol{r}_{\parallel}$ are the wavevector and the position vector parallel to this plane. $Q^{\alpha-}_{-\boldsymbol{\kappa}}$ is the local absorption rate per unit volume for a film irradiated with polarized light of unit intensity and is given by

$$Q^{\alpha-}_{-\boldsymbol{\kappa}}(\boldsymbol{r}_{\parallel}, z) = \frac{\omega}{c} \varepsilon_I(\boldsymbol{r}_{\parallel}, z) \frac{|\boldsymbol{E}^{\alpha-}_{-\boldsymbol{k}_{\parallel}}(\boldsymbol{r}_{\parallel}, z)|^2}{|\widetilde{\boldsymbol{E}}^{\alpha-}|^2}, \tag{3.2}$$

where c and ω are the speed and angular frequency of the light, ε_I is the imaginary dielectric function, $\boldsymbol{k}_{\parallel}$ is the component of $\boldsymbol{\kappa}$ in the first Brillouin zone, $\boldsymbol{E}^{\alpha-}_{-\boldsymbol{k}_{\parallel}}$ is the electric field inside the film with $-\boldsymbol{k}_{\parallel}$ when irradiated by light of polarization α and parallel wavevector $-\boldsymbol{\kappa}$, and $\widetilde{\boldsymbol{E}}^{\alpha-}$ is the Fourier component of the electric field for an incident plane wave with parallel wavevector $-\boldsymbol{\kappa}$. $\mathcal{P}^{\alpha+}_{BB}$ is the black-body radiation intensity given by

$$\mathcal{P}^{\alpha+}_{BB}(\boldsymbol{r}_{\parallel}, z) = \frac{\hbar\omega^3}{8\pi^3 c^2} \frac{1}{e^{\hbar\omega/k_B T} - 1}, \tag{3.3}$$

where $\hbar, k_B$, and T, are Planck's constant, Boltzmann's constant, and temperature. Although not explicitly stated, $\mathcal{P}$, Q, ε_I, and $\boldsymbol{E}$ depend on ω, and due to nonuniform T, $\mathcal{P}^{\alpha+}_{BB}$ depends on position.

Note that Eq. (3.1) states that the emission $\mathcal{P}$, which is caused by current fluctuations, is related to the absorption rate Q, as required by the fluctuation-dissipation theorem. Also, $\mathcal{P}^{\alpha+}_{+\boldsymbol{\kappa}}$ is related to the absorption rate for light propagating in the opposite direction, i.e., $Q^{\alpha-}_{-\boldsymbol{\kappa}}$, as required by the reciprocity theorem.

Next we assume that the structure consists of two material components labeled 1 and 2 with temperatures T_1 and T_2. In this case, Eq. (3.1) can be reduced to

$$\mathcal{P}^{\alpha+} = A_1^{\alpha-}\mathcal{P}^{\alpha+}_{BB}(T_1) + A_2^{\alpha-}\mathcal{P}^{\alpha+}_{BB}(T_2), \tag{3.4}$$

where $A_i^{\alpha-}$ is given by

$$A_i^{\alpha-} = \frac{\int_{S_i} d\boldsymbol{r}_\parallel \int dz Q^{\alpha-}_{-\boldsymbol{\kappa}}(\boldsymbol{r}_\parallel, z)}{S_{uc}\cos\theta}, \tag{3.5}$$

with S_i as the area of component i in the xy unit cell. For simplicity we do not include the dependence of $A_i^{\alpha-}$ on $\boldsymbol{k}_\parallel$ in our notation. $A_i^{\alpha-}$ is a useful parameter for describing photonic structures. Because the overall absorptivity $A^{\alpha-}$ for α polarization is the sum

$$A^{\alpha-} = A_1^{\alpha-} + A_2^{\alpha-}, \tag{3.6}$$

$A_i^{\alpha-}$ represents the local contribution of component i. Thus, we refer to it as the local absorptivity. Here we make a connection to an analogous parameter, the local density of photonic states (LDOS). LDOS helps quantify the contribution of an individual optical dipole at a specific location in a photonic crystal to the spontaneous emission from a distribution of dipoles [12, 13]. Similarly, Eq. (3.4) shows that the local absorptivity can describe specific spatial contributions to the thermal emission intensity. Consequently, once all $A_i^{\alpha-}$ are known, the thermal emission can be obtained for various temperature configurations. Due to this relationship to emission, $A_i^{\alpha-}$ could alternatively be called the local emissivity.

3.3 Numerical Calculation

To be useful for spectral control of thermal emission, the two components in Eq. (3.4) must have local absorptivities that peak at different energies. We demonstrate this

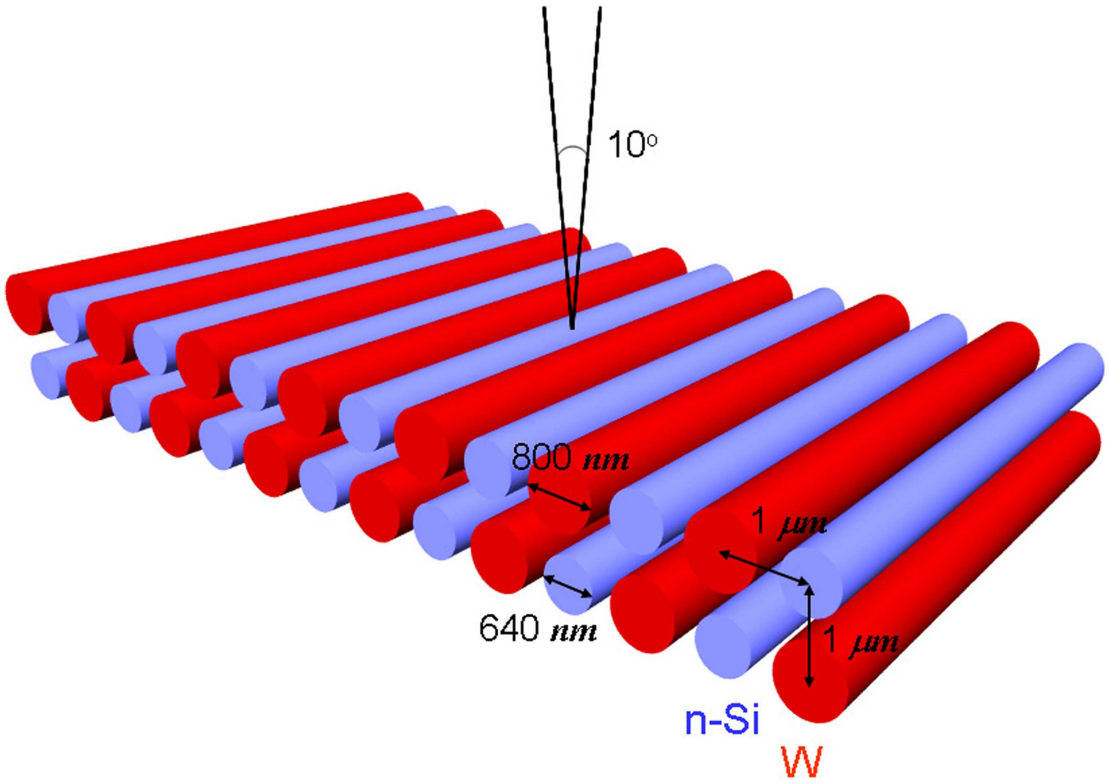

Figure 3.1: A computer generated image of the W-Si rod structure shown in the inset of Fig. 3.2. In the calculations, the thermally emitted light is collected over an angular cone of ±5° from the z axis as shown.

possibility with calculations for a specific structure [14]. Two layers of parallel tungsten and silicon rods lie in the plane of the film (the xy plane). The rods are arranged as in the cross-section in Fig. 3.2. This structure repeats in the x direction; the rods are uniform in y. A computer generated image of the structure is shown in Fig. 3.1. We used experimental dielectric functions [15] and assumed a donor concentration of 3×10^{19} cm^{-3} for Si so it has an absorption comparable to W near 0.45 eV. Figure 3.2a shows the calculated absorptivity when the film is illuminated along z by TE polarized light (the magnetic field along the rods). This calculation also averages the absorptivity over ±5° from the z axis to approximate experiments. Two pronounced peaks at 0.428 and 0.458 eV are found. The local absorptivities in Fig. 3.2b show that each peak can be

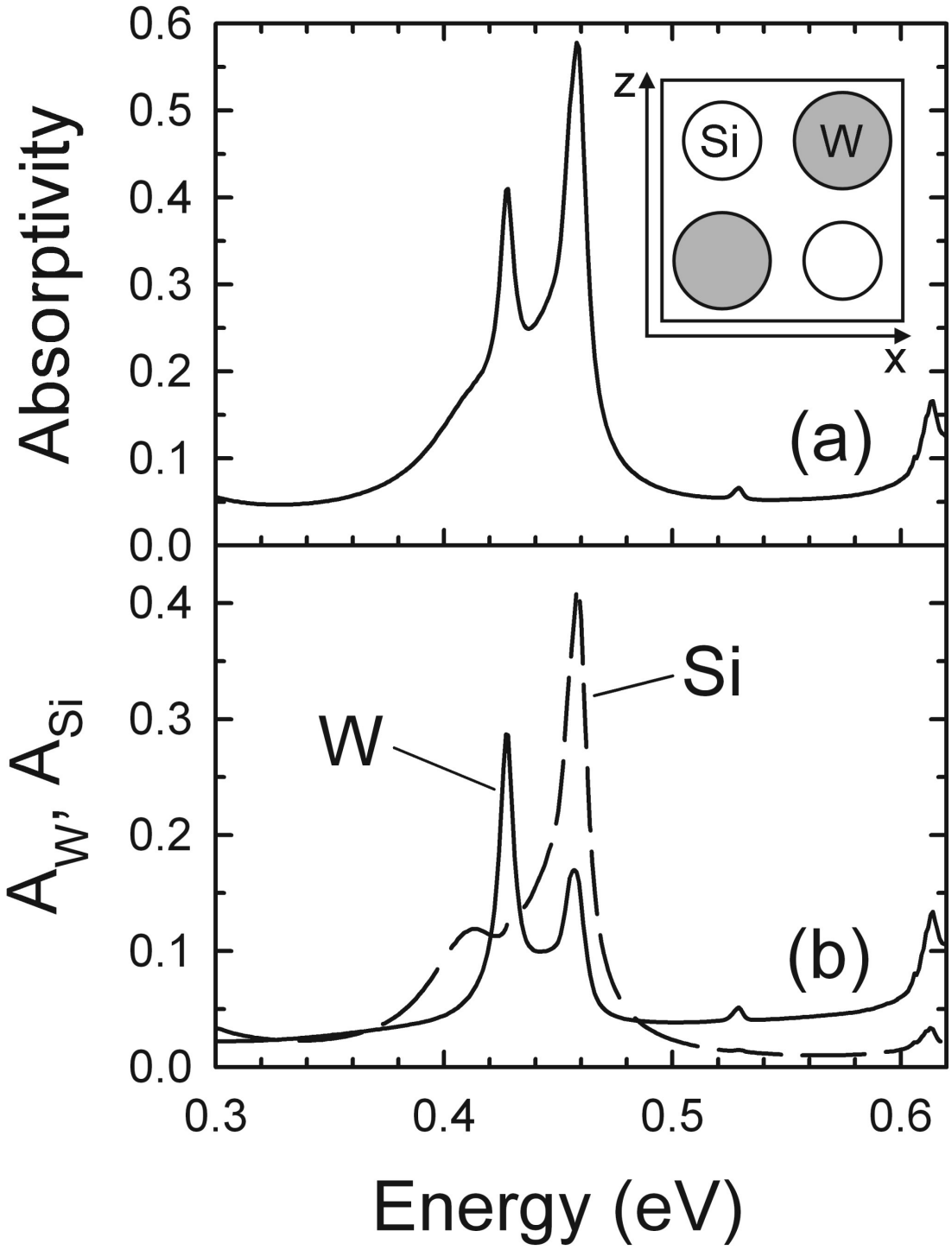

Figure 3.2: Calculated (a) absorptivity and (b) local absorptivities, A_W and A_{Si}, for a film with the cross section in the inset. This structure repeats in the x direction and is uniform in y. The W and Si rods are 800 and 640 nm in diameter, respectively. The center-to-center distance of neighboring rods is 1 μm. The absorptivity is averaged for TE polarized light incident over a cone $\pm 5^\circ$ from the z axis.

attributed primarily either to the W or the Si rods. This occurs because the structure has two resonances which concentrate the light differently in the two rods. Fig. 3.3 shows Q, the calculated local absorption rate per unit volume. The panels 3.3a and 3.3b show Q at 0.428 eV and 0.458 eV, respectively, calculated using Eq. (3.2). To see the profile more clearly, we plot Q on a log scale. At both energies, the field intensity is spread over the Si rod, while it is limited to the surface region of the W rod due to the skin effect. However, the relative magnitude of the field intensity changes between the two cases. At 0.428 eV, the field is more concentrated in W; at 0.458 eV it is more concentrated in the Si. Indeed, when the local absorption rate is integrated over the cross-sectional area of each rod, the absorption occurs mostly in the W and the Si for panels 3.3a and 3.3b, respectively. This agrees with the local absorptivity in Fig. 3.2b. However, note that the peaks still have some mixed character. For example, some light is absorbed by W even on the resonance assigned to Si. This explains the weak peak at 0.458 eV in A_W in Fig. 3.2b.

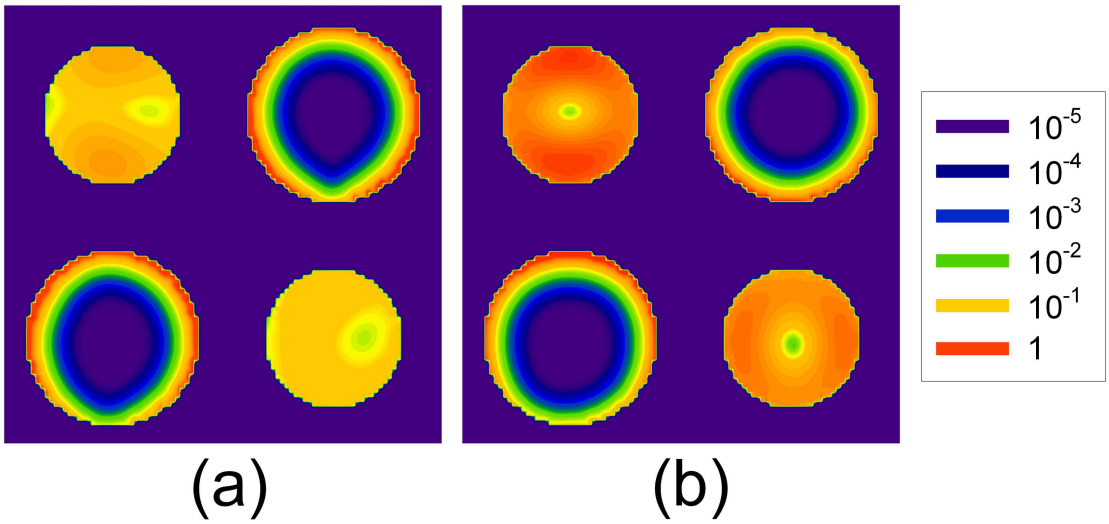

Figure 3.3: Calculated Q, the local absorption rate per unit volume, at (a) 0.428 eV and (b) 0.458 eV. The description of the structure and the materials is the same as in Fig. 3.1. Q is averaged for TE polarized light incident over an angular cone of $\pm 5^\circ$ from the z axis. The plot is arbitrary units and plotted on a log scale.

Thus, Eq. (3.4) suggests that the peak at 0.428 eV will be strong if the W rods are heated and the 0.458 eV peak will dominate if Si is heated. However, we must determine the temperature to apply. Note that the goal is different than with uniform heating, where the temperature is chosen simply to overlap the black-body spectrum with the absorption to maximize the emission [4]. Here we want to control the emission frequency. We consider two cases and apply Eq. (3.4). When W is "hot" and Si is "cold", we label the result $\mathcal{P}^{\alpha+}_{Whot}$. The opposite case is $\mathcal{P}^{\alpha+}_{Sihot}$. Taking the ratio, we obtain

$$\frac{\mathcal{P}^{\alpha+}_{Whot}}{\mathcal{P}^{\alpha+}_{Sihot}} = \frac{A^{\alpha-}_{W} + A^{\alpha-}_{Si}\,\rho(T_c, T_h)}{A^{\alpha-}_{W}\,\rho(T_c, T_h) + A^{\alpha-}_{Si}}, \tag{3.7}$$

where T_h and T_c are the temperatures of the hot and cold rods, respectively, and

$$\rho(T_c, T_h) = \frac{\mathcal{P}^{\alpha+}_{BB}(T_c)}{\mathcal{P}^{\alpha+}_{BB}(T_h)} < 1. \tag{3.8}$$

From Eq. (3.8), we see that $\rho(T_c, T_h)$ should be minimized to maximize the intensity contrast for the two peaks. In the ideal case, $\rho(T_c, T_h)$ vanishes and the ratio becomes $A^{\alpha-}_{W}/A^{\alpha-}_{Si}$. Figure 3.4 shows $\rho(T_c, T_h)$ as a function of T_c when $T_h - T_c$ is 300K. Several specific photon energies are plotted. For example, when T_c is 500K, $\rho(T_c, T_c + 300)$ is about 0.02 at 0.428 and 0.458 eV. Thus, the peak contrast should be nearly ideal at these temperatures. Moreover, they are well below the melting points of the two components (3687K for W and 1687K for Si).

The emission intensities obtained from Eq. (3.4) for T_c =500K and T_h =800K are displayed in Fig. 3.5. As predicted, the two peaks can be controlled depending on which rods are hot. Moreover, the intensity contrast is pronounced at these temperatures. For comparison, we also plot the emission spectra when both rods are 500K or both 800K. The results with T_c =500K and T_h =800K are bounded by the uniform cases at all photon energies.

Of course, if the goal is to control the energy of a thermal emission peak, approaches other than selective heating are possible. For example, the rod spacing in a uniformly heated structure could simply be modified. In our case, the Si rods could be removed

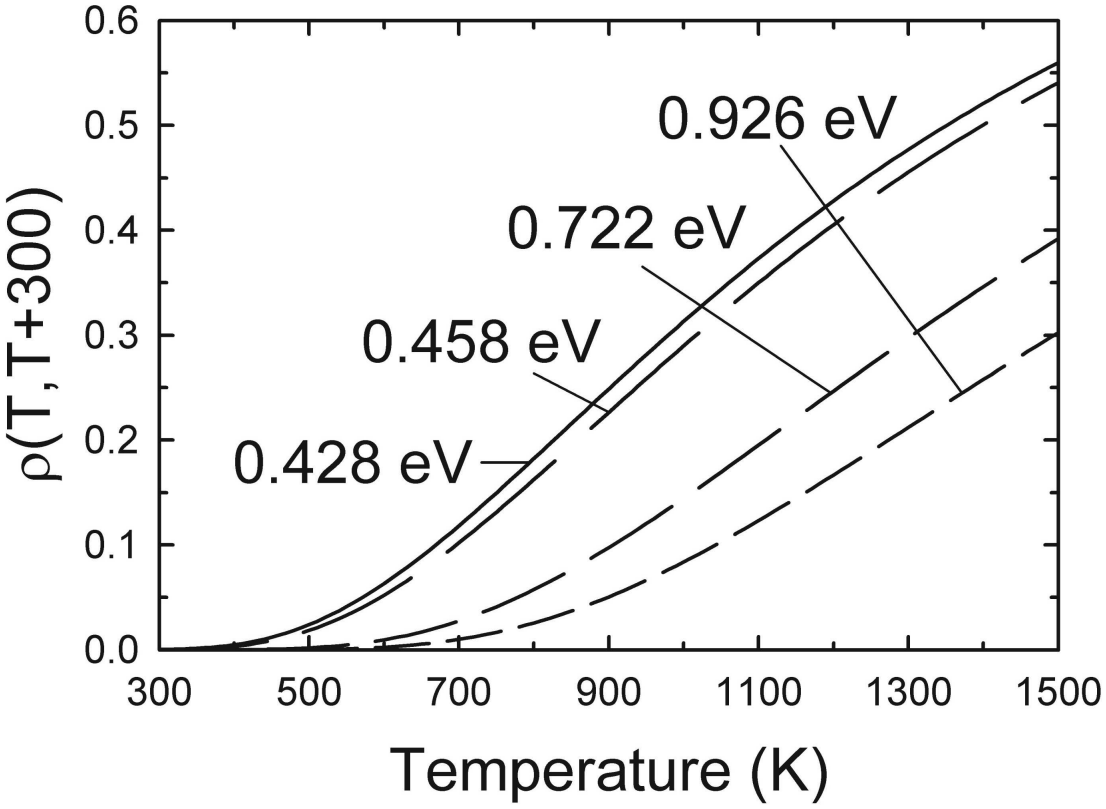

Figure 3.4: The ratio, $\rho(T, T+300)$, of the black body emission spectra at temperatures T and T+300 versus temperature for several photon energies.

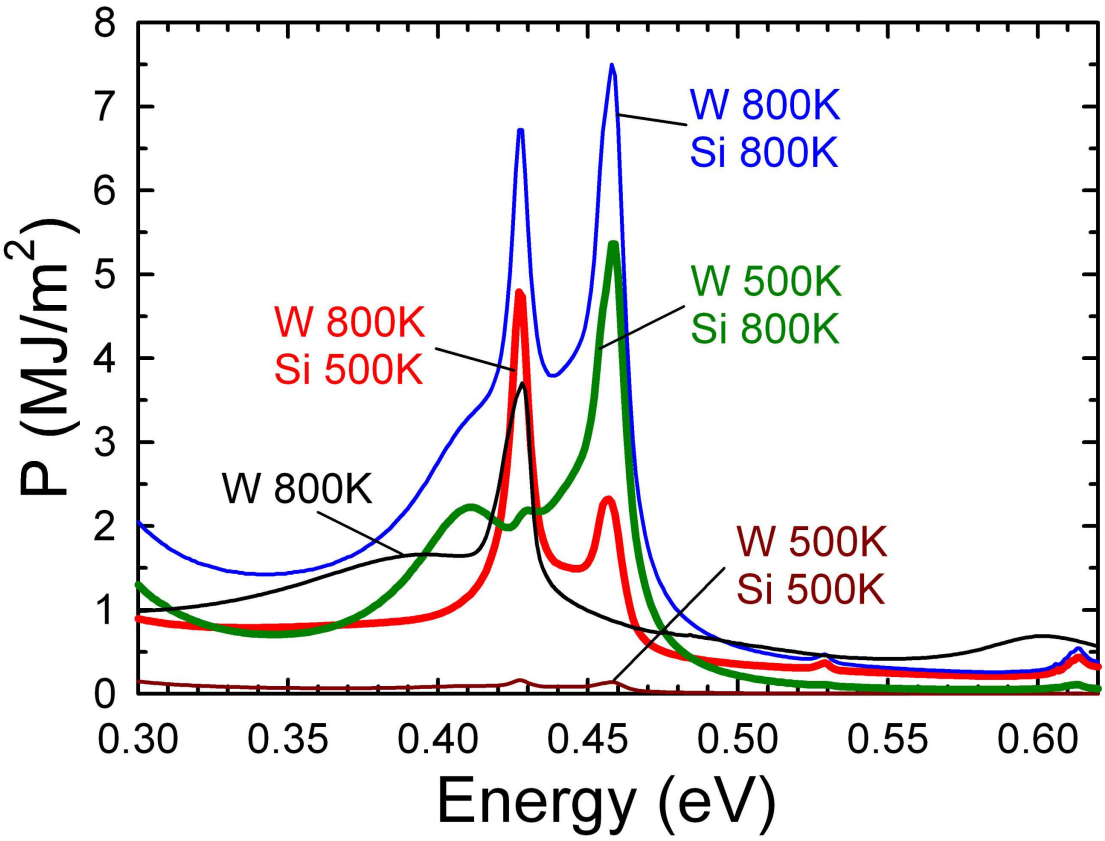

Figure 3.5: Calculated thermal emission intensities for TE polarized light for the W-Si film in Fig. 3.2. Several temperature combinations are plotted. The emission is averaged over $\pm 5^\circ$ from the z axis. The black curve is the emission without Si rods; the W rod separation is increased by 28%.

and the emission energy tuned by changing the separation between the W rods. However, we find that the presence of the Si rods actually induces more emission from the W. To show this, we calculated the emission spectrum for our film without the Si rods. Since vacuum now replaces the Si, the optical path length between the W rods decreases. Consequently, the emission peak associated with W appears at higher energy. To compare with the result for the W-Si film, we increased the distance between the W rods by 28% to return the W peak to its original energy (0.428 eV). The resulting emission spectrum at 800K is shown as the black line in Fig. 3.5. The peak is clearly weaker than when W rods are heated to 800K in the presence of cooler Si rods. This occurs because the Si rods modify the local absorptivity of the W. Thus, selective heating not only provides the ability to control the emission energy with temperature, but the presence of the dielectric rods can also boost the emission. More generally, it allows greater flexibility in the design of emission sources.

If we use different materials, emission control can also be shifted to higher energies. For example, a film similar to above, but with copper and germanium rods, can exhibit emission peaks near the optical wavelength of 1.5 μm (0.83 eV). The rod spacing in the film is adjusted as shown in the cross sectional view in Fig. 3.6. Figure 3.6 also plots the calculated intensities for light emitted from the film in the z direction. The temperatures of the rods are the same as in Fig. 3.5, which are below the melting points of Cu (1358K) and Ge (1211K). Two strong peaks appear at 0.722 and 0.926 eV with only broad background emission below 0.6 eV. For this film, the association of each peak with either the metal or the dielectric rods is even stronger than above. Thus, even better control can be obtained. When the Cu rods are hotter than the Ge, the contrast in the two peak intensities is 16.1. In the opposite case, the contrast is 44.1.

The improved contrast in the Cu-Ge film occurs because $\rho(T_c, T_h)$ is smaller at higher energies. At T =500K, $\rho(T, T + 300)$ is less than 0.002 near 0.83 eV. As seen in Eq. (3.8), the intensity contrast should increase with decreasing $\rho(T_c, T_h)$. In addition, ε_I for Ge changes significantly between the two emission energies. It varies from 0.004 at

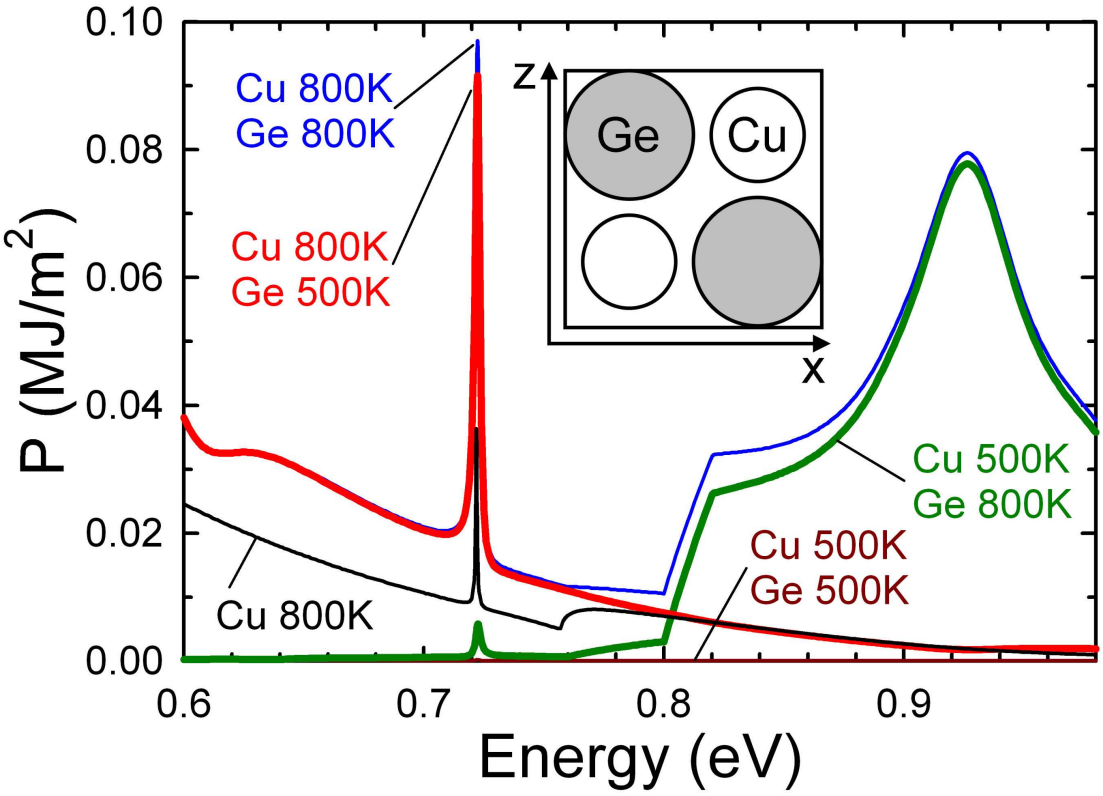

Figure 3.6: Thermal emission intensities, calculated as in Fig. 3.5, for a film of Cu and Ge rods with the cross section shown. This structure repeats in the x direction and is uniform in y. The Cu and Ge rods are 273 and 375 nm in diameter, respectively. The center-to-center distance of neighboring rods is 375 nm. The black curve is the emission without Ge rods; the Cu rod separation is increased by 118%. The kinks at 0.8 and 0.821 eV are due to changes in the Ge dielectric function; the kink at 0.757 eV is due to a Wood's anomaly.

0.722 eV to 0.63 at 0.926 eV. This affects the local absorptivity and consequently, the emission from the Ge rods is small at 0.722 eV and significant at 0.926 eV, leading to increased contrast.

As above, we also considered the film with the dielectric rods removed, in this case Ge. For this calculation, we increased the spacing of the Cu rods by 118% to maintain the energy of the emission peak at 0.722 eV. As seen in Fig. 3.6, the emission intensity at 800K for this peak is lower than for the Cu-Ge film. Indeed, the decrease is even more pronounced than for the W-Si film (Fig. 3.5). Because Ge has a larger dielectric constant than Si ($\sim$17 vs $\sim$11) and occupies more volume in our film, the presence of the Ge rods has a larger influence.

3.4 Discussion

We have seen that thermal emission can be controlled by selective heating if fluctuation-dissipation theorem can be assumed. However, two important issues remain: (i) whether such temperature differences can be achieved on a micrometer length scale and (ii) whether our assumption that the fluctuation-dissipation theorem is valid locally is reasonable. In the Appendix, we show that for our structures thermal conduction along the rods, rather than radiation between them, dominates heat transport. This indicates that if opposite ends of the different rods could be connected to heat reservoirs of different temperatures, the required temperature difference could be obtained. For example, an array of long rods could be fabricated that span a gap between two solid films. The W rods could be connected directly to the top film, but separated thermally from the bottom film by a section of insulating material. The Si rods could be connected oppositely. Thus, by setting the temperatures of the two films, a temperature difference could be achieved. Because thermal transport along the rods dominates, this also implies that local thermal equilibrium should be very nearly satisfied within each rod. In this case, applying the fluctuation-dissipation theorem locally is a reasonable

approximation. More generally, its validity will depend on the specifics of the system and the heating mechanism. If non-equilibrium processes become significant, corrections to the fluctuation-dissipation theorem would be required and our approach would not be justified.

3.5 Conclusion

We predict that thermal emission can be controlled by selective heating of periodic structures. We used the reciprocity theorem which implies that strongly absorbing parts will also strongly emit. In general, selective heating may find applications in active control of thermal light sources. The reverse process, selective absorption, could also lead to local temperature gradients. Thus, further study is required to clarify the full potential and implications of this effect.

APPENDIX

To control thermal emission by selective heating, it is necessary to maintain large temperature differences between structural objects (*e.g.*, rods) that are separated by micrometer-length scales. For a feasibility analysis, it is helpful to identify the dominant heat-transfer mechanism for these objects. In this section, we develop a general scaling argument that addresses heat transport at small length scales. Specifically, we begin by assuming that the fluctuation-dissipation theorem is valid. We then compare the heat transfer due to conduction and radiation and find that conduction dominates the thermal transport. This suggests that the temperature of one of our structural objects will be uniform if connected to a thermal reservoir. This justifies the assumption of the fluctuation-dissipation theorem at the beginning of this analysis. More importantly, it indicates that large temperature differences can indeed be maintained between two micrometer-scale structural objects that are connected to two different reservoirs. Finally, we discuss previously published experiments that verify these conclusions.

In our analysis, we consider for simplicity a structural object consisting of non-magnetic materials and neglect any frequency dependence to the dielectric function. (We return to the frequency dependence below.) We then treat the system at steady state where heat is transported both by radiation and conduction. The energy balance for this system is

$$\nabla \cdot (\sigma \nabla T) + \nabla \cdot \langle \boldsymbol{S} \rangle = 0, \tag{A-1}$$

where σ is the thermal conductivity and $\boldsymbol{S}$ is the Poynting vector. The first and the second terms of Eq. (A-1) are the net rate of heat input per unit volume by conduction and by radiation, respectively. The ensemble-averaged Poynting vector is related to its frequency component by [16]

$$\langle \boldsymbol{S} \rangle = 2 \int_0^\infty d\omega \, \langle \boldsymbol{S}_\omega \rangle \,, \tag{A-2}$$

where $\langle \boldsymbol{S}_\omega \rangle$ is given by

$$\langle \boldsymbol{S}_\omega \rangle \, \delta(\omega - \omega') = \frac{1}{2} \left\langle \boldsymbol{E}(\boldsymbol{r}, \omega) \times \boldsymbol{H}(\boldsymbol{r}, \omega') \right\rangle . \tag{A-3}$$

The $\boldsymbol{E}$ and the $\boldsymbol{H}$ fields are expressed in terms of Green's dyadics G and currents $\boldsymbol{j}$ by

$$\begin{aligned} \boldsymbol{E}(\boldsymbol{r}, \omega) &= i\omega\mu_0 \int d\boldsymbol{r}' G^E(\boldsymbol{r}, \boldsymbol{r}'; \omega) \cdot \boldsymbol{j}(\boldsymbol{r}', \omega) \\ \boldsymbol{H}(\boldsymbol{r}, \omega) &= \int d\boldsymbol{r}' G^H(\boldsymbol{r}, \boldsymbol{r}'; \omega) \cdot \boldsymbol{j}(\boldsymbol{r}', \omega), \end{aligned} \tag{A-4}$$

where μ_0 is the permeability of free space. We substitute Eq. (A-4) into Eq. (A-3) and use the fluctuation-dissipation theorem [11]

$$\left\langle {j_j}^*(\boldsymbol{r}', \omega, T) j_k(\boldsymbol{r}'', \omega', T) \right\rangle = \frac{\omega \Theta(\omega, T)}{\pi} \varepsilon_0 \varepsilon_I(\boldsymbol{r}', \omega) \delta_{jk} \delta(\boldsymbol{r}' - \boldsymbol{r}'') \delta(\omega - \omega'), \tag{A-5}$$

where ε_0 is the permittivity of free space, ε_I the imaginary part of the dielectric function, $i, j, k = x, y, z$, and $\Theta(\omega, T) = \frac{\hbar\omega}{e^{\hbar\omega/k_B T} - 1}$. We arrive at

$$\langle \boldsymbol{S}_\omega \rangle = \frac{\hat{\boldsymbol{r}}_i}{2} \int d\boldsymbol{r}' \epsilon_{ijk} G^{E*}_{jl}(\boldsymbol{r}, \boldsymbol{r}'; \omega) G^H_{kl}(\boldsymbol{r}, \boldsymbol{r}'; \omega) \varepsilon_I(\boldsymbol{r}', \omega) \frac{i\hbar}{\pi c^2} \frac{\omega^3}{e^{\hbar\omega/k_B T(\boldsymbol{r}')} - 1}, \tag{A-6}$$

where $\hat{\boldsymbol{r}}_i$ is the i-component unit vector ($i, j, k = x, y, z$) and ϵ_{ijk} is the permutation symbol. (The validity of our use of the fluctuation-dissipation theorem will be discussed further below.) Using Eq. (A-1), (A-2), and (A-6), we have for the net input thermal conduction rate

$$\begin{aligned} \nabla \cdot [\sigma(\boldsymbol{r}) \nabla T(\boldsymbol{r})] &= -\int_0^\infty d\omega \frac{i\hbar\omega^3}{\pi c^2} \frac{\partial}{\partial r_i} \int d\boldsymbol{r}' \epsilon_{ijk} G^{E*}_{jl}(\boldsymbol{r}, \boldsymbol{r}'; \omega) G^{H}_{kl}(\boldsymbol{r}, \boldsymbol{r}'; \omega) \\ &\times \varepsilon_I(\boldsymbol{r}', \omega) \frac{1}{e^{\hbar\omega/k_B T(\boldsymbol{r}')} - 1}. \end{aligned} \tag{A-7}$$

Now because we are assuming that the dielectric function is independent of the frequency, we can expand or compress the system linearly. For this, we define dimensionless variables using the characteristic length L as

$$\begin{aligned} \bar{\boldsymbol{r}} &\equiv \frac{\boldsymbol{r}}{L} \\ \bar{\nabla} &\equiv L\nabla \\ \bar{\omega} &\equiv \frac{L}{c}\omega. \end{aligned} \tag{A-8}$$

Using these variables in Maxwell's equations

$$\begin{aligned} &\nabla \cdot [\varepsilon(\boldsymbol{r}) \boldsymbol{E}(\boldsymbol{r}, \omega)] = -\frac{i}{\varepsilon_0 \omega} \nabla \cdot \boldsymbol{j}(\boldsymbol{r}, \omega) \\ &\nabla \times \boldsymbol{E}(\boldsymbol{r}, \omega) = i\omega\mu_0 \boldsymbol{H}(\boldsymbol{r}, \omega) \\ &\nabla \cdot \boldsymbol{H}(\boldsymbol{r}, \omega) = 0 \\ &\nabla \times \boldsymbol{H}(\boldsymbol{r}, \omega) = -\frac{i\omega}{\mu_0 c^2} \varepsilon(\boldsymbol{r}) \boldsymbol{E}(\boldsymbol{r}, \omega) + \boldsymbol{j}(\boldsymbol{r}, \omega), \end{aligned} \tag{A-9}$$

we have

$$\begin{aligned} &\bar{\nabla} \cdot [\tilde{\varepsilon}(\bar{\boldsymbol{r}}) \tilde{\boldsymbol{E}}(\bar{\boldsymbol{r}}, \bar{\omega})] = -\frac{i}{\varepsilon_0 \bar{\omega}} \bar{\nabla} \cdot \left[\frac{L}{c} \tilde{\boldsymbol{j}}(\bar{\boldsymbol{r}}, \bar{\omega}) \right] \\ &\bar{\nabla} \times \tilde{\boldsymbol{E}}(\bar{\boldsymbol{r}}, \bar{\omega}) = i\bar{\omega}\mu_0 [c\tilde{\boldsymbol{H}}(\bar{\boldsymbol{r}}, \bar{\omega})] \\ &\bar{\nabla} \cdot [c\tilde{\boldsymbol{H}}(\bar{\boldsymbol{r}}, \bar{\omega})] = 0 \\ &\bar{\nabla} \times [c\tilde{\boldsymbol{H}}(\bar{\boldsymbol{r}}, \bar{\omega})] = -\frac{i\bar{\omega}}{\mu_0 c^2} \tilde{\varepsilon}(\bar{\boldsymbol{r}}) \tilde{\boldsymbol{E}}(\bar{\boldsymbol{r}}, \bar{\omega}) + \left[\frac{L}{c} \tilde{\boldsymbol{j}}(\bar{\boldsymbol{r}}, \bar{\omega}) \right]. \end{aligned} \tag{A-10}$$

Here we used $\tilde{\Upsilon}(\bar{\boldsymbol{r}},\bar{\omega}) \equiv \Upsilon(L\bar{\boldsymbol{r}}, c\bar{\omega}/L)$ with $\Upsilon = \boldsymbol{E}$, $\boldsymbol{H}$, $\boldsymbol{j}$, and ε. By comparing Eqs. (A-9) and (A-10) we find that they are equivalent in form when $\boldsymbol{j}$ and $\boldsymbol{H}$ are replaced by $L\tilde{\boldsymbol{j}}/c$ and $c\tilde{\boldsymbol{H}}$, respectively. Thus, the equivalent form of Eq. (A-4) can be written as

$$\begin{aligned} \tilde{\boldsymbol{E}}(\bar{\boldsymbol{r}},\bar{\omega}) &= i\bar{\omega}\mu_0 \int d\bar{\boldsymbol{r}}' G^E(\bar{\boldsymbol{r}},\bar{\boldsymbol{r}}';\bar{\omega}) \cdot \frac{L}{c}\tilde{\boldsymbol{j}}(\bar{\boldsymbol{r}}',\bar{\omega}) \\ c\tilde{\boldsymbol{H}}(\bar{\boldsymbol{r}},\bar{\omega}) &= \int d\bar{\boldsymbol{r}}' G^H(\bar{\boldsymbol{r}},\bar{\boldsymbol{r}}';\bar{\omega}) \cdot \frac{L}{c}\tilde{\boldsymbol{j}}(\bar{\boldsymbol{r}}',\bar{\omega}), \end{aligned} \tag{A-11}$$

where $G^{E/H}(\bar{\boldsymbol{r}},\bar{\boldsymbol{r}}';\bar{\omega})$ is independent of L as its arguments indicate. Using Eq. (A-8) in Eq. (A-4), we obtain

$$\begin{aligned} \tilde{\boldsymbol{E}}(\bar{\boldsymbol{r}},\bar{\omega}) &= i\bar{\omega}\mu_0 \int d\bar{\boldsymbol{r}}' c^2 L G^E(\boldsymbol{r},\boldsymbol{r}';\omega) \cdot \frac{L}{c}\tilde{\boldsymbol{j}}(\bar{\boldsymbol{r}}',\bar{\omega}) \\ c\tilde{\boldsymbol{H}}(\bar{\boldsymbol{r}},\bar{\omega}) &= \int d\bar{\boldsymbol{r}}' c^2 L^2 G^H(\boldsymbol{r},\boldsymbol{r}';\omega) \cdot \frac{L}{c}\tilde{\boldsymbol{j}}(\bar{\boldsymbol{r}}',\bar{\omega}). \end{aligned} \tag{A-12}$$

From Eq. (A-11) and Eq. (A-12), we have

$$\begin{aligned} G^E(\bar{\boldsymbol{r}},\bar{\boldsymbol{r}}';\bar{\omega}) &= c^2 L G^E(\boldsymbol{r},\boldsymbol{r}';\omega) \\ G^H(\bar{\boldsymbol{r}},\bar{\boldsymbol{r}}';\bar{\omega}) &= c^2 L^2 G^H(\boldsymbol{r},\boldsymbol{r}';\omega). \end{aligned} \tag{A-13}$$

If we define the dimensionless quantities for Green's dyadic as

$$\begin{aligned} \bar{G}^E(\bar{\boldsymbol{r}},\bar{\boldsymbol{r}}';\bar{\omega}) &\equiv L G^E(\boldsymbol{r},\boldsymbol{r}';\omega) \\ \bar{G}^H(\bar{\boldsymbol{r}},\bar{\boldsymbol{r}}';\bar{\omega}) &\equiv L^2 G^H(\boldsymbol{r},\boldsymbol{r}';\omega), \end{aligned} \tag{A-14}$$

they are independent of L. Using Eq. (A-8) and (A-14), Eq. (A-7) can be expressed in terms of the dimensionless variables as

$$\begin{aligned} &\bar{\nabla} \cdot [\tilde{\sigma}(\bar{\boldsymbol{r}})\bar{\nabla}\tilde{T}(\bar{\boldsymbol{r}})] \\ &= -\frac{i\hbar c^2}{\pi L^3} \int_0^\infty d\bar{\omega} \frac{\partial}{\partial \bar{r}_i} \int d\bar{\boldsymbol{r}}' \epsilon_{ijk} \bar{G}^{E*}_{jl}(\bar{\boldsymbol{r}},\bar{\boldsymbol{r}}';\bar{\omega}) \bar{G}^H_{kl}(\bar{\boldsymbol{r}},\bar{\boldsymbol{r}}';\bar{\omega}) \frac{\tilde{\varepsilon}_I(\bar{\boldsymbol{r}}')\bar{\omega}^3}{e^{\hbar c\bar{\omega}/Lk_B\tilde{T}(\bar{\boldsymbol{r}}')} - 1}, \end{aligned} \tag{A-15}$$

where we used $\tilde{\Omega}(\bar{\boldsymbol{r}}) \equiv \Omega(L\bar{\boldsymbol{r}})$ with $\Omega = \sigma$, T, and ε_I. These quantities are independent of the characteristic length L and are appropriate for linear expansion or compression

of a system. In Eq. (A-15), we expand $\epsilon_{ijk}\bar{G}^{E*}_{jl}(\bar{\boldsymbol{r}},\bar{\boldsymbol{r}}';\bar{\omega})\bar{G}^{H}_{kl}(\bar{\boldsymbol{r}},\bar{\boldsymbol{r}}';\bar{\omega})$ in a Taylor series as

$$\epsilon_{ijk}\bar{G}^{E*}_{jl}(\bar{\boldsymbol{r}},\bar{\boldsymbol{r}}';\bar{\omega})\bar{G}^{H}_{kl}(\bar{\boldsymbol{r}},\bar{\boldsymbol{r}}';\bar{\omega}) = \sum_{n=0}^{\infty} a_{in}(\bar{\boldsymbol{r}},\bar{\boldsymbol{r}}')\bar{\omega}^n \tag{A-16}$$

and obtain

$$\begin{aligned} & \bar{\nabla}\cdot[\tilde{\sigma}(\bar{\boldsymbol{r}})\bar{\nabla}\tilde{T}(\bar{\boldsymbol{r}})] \\ = \; & -\frac{i\hbar c^2}{\pi L^3}\frac{\partial}{\partial\bar{r}_i}\int d\bar{\boldsymbol{r}}'\sum_{n=0}^{\infty} a_{in}(\bar{\boldsymbol{r}},\bar{\boldsymbol{r}}')\tilde{\varepsilon}_I(\bar{\boldsymbol{r}}')\int_0^{\infty} d\bar{\omega}\frac{\bar{\omega}^{n+3}}{e^{\hbar c\bar{\omega}/Lk_B\tilde{T}(\bar{\boldsymbol{r}}')}-1}. \end{aligned} \tag{A-17}$$

The integral over $\bar{\omega}$ in Eq. (A-17) can be evaluated [16] using

$$\int_0^{\infty} dz\frac{z^{x-1}}{e^z-1} = \Gamma(x)\zeta(x) \tag{A-18}$$

for $x>1$, where $\Gamma(x)$ and $\zeta(x)$ are the Gamma function and the Riemann zeta function, respectively, defined by

$$\begin{aligned} \Gamma(x) &= \int_0^{\infty} dt\, t^{x-1}e^{-t} \\ \zeta(x) &= \sum_{n=1}^{\infty}\frac{1}{n^x}. \end{aligned} \tag{A-19}$$

After the evaluation, Eq. (A-17) becomes

$$\begin{aligned} & \bar{\nabla}\cdot[\tilde{\sigma}(\bar{\boldsymbol{r}})\bar{\nabla}\tilde{T}(\bar{\boldsymbol{r}})] \\ = \; & -\frac{i\hbar c^2}{\pi L^3}\frac{\partial}{\partial\bar{r}_i}\int d\bar{\boldsymbol{r}}'\sum_{n=0}^{\infty} a_{in}(\bar{\boldsymbol{r}},\bar{\boldsymbol{r}}')\tilde{\varepsilon}_I(\bar{\boldsymbol{r}}')\left(\frac{Lk_B\tilde{T}(\bar{\boldsymbol{r}}')}{\hbar c}\right)^{n+4}\Gamma(n+4)\zeta(n+4). \end{aligned} \tag{A-20}$$

We see that the right hand side of Eq. (A-20) will decrease as the characteristic length L decreases. If it vanishes, we have

$$\bar{\nabla}\cdot[\tilde{\sigma}(\bar{\boldsymbol{r}})\bar{\nabla}\tilde{T}(\bar{\boldsymbol{r}})] \simeq 0, \tag{A-21}$$

which is the heat transport equation when the radiation is negligible.

Now, it is important for us to realize that even for macroscopic systems it is common practice in heat-transport analyses to neglect radiation because it is typically negligible in comparison to conduction, convection, and diffusion [17]. For example, if we fully analyze two macroscopic rods in vacuum that are separated by a macroscopic distance while being connected to two separate heat reservoirs at different temperatures, we will find that heat transport is dominated by conduction along the rods. According to Eq. (A-20), if this macroscopic system is scaled down linearly to microscopic scale, heat conduction will become even more dominant. In this case, the condition for Eq. (A-21) will be well satisfied. Therefore, we can safely conclude that conduction becomes dominant over the radiation term for micrometer-scale structural objects. Further, this suggests that the temperature will be uniform within each object and temperature differences between objects can be maintained if they are each connected to different thermal reservoirs. Finally, we note that because we find that the temperature should be uniform within each object, our initial assumption in Eq. (A-6) of the fluctuation-dissipation theorem can be justified.

This general scaling argument is strictly valid when the dielectric function of the object is constant. If metals that have frequency-dependent dielectric functions are involved, the considerations become more complicated. However, the large conductivity of metals would also contribute to the dominance of the conduction term. In addition, if the structure is designed such that the Green's dyadic is small, the heat transfer by radiation can also become negligible. Therefore, in general, a more detailed analysis would be required.

Despite the above results, one may question the applicability of the fluctuation-dissipation theorem in analyzing thermal transport between closely spaced micrometer-scale objects. However, this approach is not unique to our work. Indeed, the fluctuation-dissipation theorem has been employed in many theoretical studies of this type [18, 19, 20, 21, 22, 23, 24, 25, 26, 27, 28, 29]. Moreover, the use of the fluctuation-dissipation

theorem in such systems has been validated experimentally [30]. Temperature gradients have been measured in metal tips that were placed above cooled planar substrates. When a gold tip at 300 K was held 100 nm above a gold substrate at 100 K, the temperature difference across the tip was only 0.0054 K. Thus, the temperature gradient inside the tip was negligible and heat conduction dominated over radiation. Furthermore, the measured radiation flux from the tip to the substrate matched theoretical predictions based on the fluctuation-dissipation theorem down to ∼10 nm separations. This suggests not only that the fluctuation-dissipation theorem is a reasonable assumption, but that temperature differences between objects can be maintained even when separated by sub-micrometer length scales.

If instead of a gold tip at 300 K, we consider a tungsten tip at 800 K, in analogy to the tungsten rods in this chapter, then radiation will be more significant. However, we can estimate the radiation flux for this system using the simple theoretical model from Ref. [18]. (This is the same model that matched the gold-tip results from Ref. [30].) For simplicity, the frequency dependence of the Green's dyadic is neglected. Then, the radiation flux from tip to substrate can be expressed by

$$\mathcal{P} \propto \int_0^\infty d\omega \frac{\omega^4}{c^4} \varepsilon_I(\omega) \alpha_I(\omega) \Theta(\omega, T), \tag{A-22}$$

where α_I is the imaginary part of the polarizability of the tip given by

$$\alpha(\omega) \propto \frac{\varepsilon(\omega) - 1}{\varepsilon(\omega) + 2}. \tag{A-23}$$

The ratio of radiation flux between the high temperature tungsten tip and the low temperature gold tip is given by

$$\frac{\mathcal{P}_W}{\mathcal{P}_{Au}} = \frac{\int_0^\infty d\omega \omega^4 \varepsilon_{I,W}(\omega) \alpha_{I,W}(\omega) \Theta(\omega, T = 800K)}{\int_0^\infty d\omega \omega^4 \varepsilon_{I,Au}(\omega) \alpha_{I,Au}(\omega) \Theta(\omega, T = 300K)}, \tag{A-24}$$

where the subscripts W and Au denote tungsten and gold, respectively. This ratio is evaluated to be 230. Moreover, the thermal conductivity of tungsten at 800 K (1.25 W/cm K) is smaller than that of gold at 300 K (3.17 W/cm K) [31]. Both effects together

can contribute to a roughly 580-fold increase in the temperature difference across the tip. This follows from Eq. (A-1) which states that the temperature difference is

$$\Delta T \propto \frac{\mathcal{P}}{\sigma}. \tag{A-25}$$

Considering that a temperature gradient of only 0.0054 K was observed for the gold tip at 300 K, the temperature gradient for the tungsten tip at 800 K separated by 100 nm is estimated to be ~ 3 K. Furthermore, for our rod structures where the separation is 300 nm, the temperature difference is estimated to be ~ 0.1 K based on the same considerations. Therefore, we conclude that the tungsten rods will still be essentially uniform in temperature.

References

[1] P. J. Hesketh, J. N. Zemel, and B. Gebhart, "Organ pipe radiant modes of periodic micromachined silicon surfaces," Nature (London) **324**, 549-551 (1986).

[2] A. Heinzel, V. Boerner, A. Gombert, B. Blasi, V. Wittwer, and J. Luther, "Radiation filters and emitters for the NIR based on periodically structured metal surfaces," J. Mod. Opt. **47**, 2399-2419 (2000).

[3] J. J. Greffet, R. Carminati, K. Joulain, J. P. Mulet, S. Mainguy, and Y. Chen, "Coherent emission of light by thermal sources," Nature (London) **416**, 61-64 (2002).

[4] C. M. Cornelius and J. P. Dowling, "Modification of Planck blackbody radiation by photonic band-gap structures," Phys. Rev. A **59**, 4736-4746 (1999).

[5] J. G. Fleming, S.-Y. Lin, I. El-Kady, R. Biswas, and K. M. Ho, "All-metallic three-dimensional photonic crystals with a large infrared bandgap," Nature (London) **417**, 52-55 (2002).

[6] S. E. Han, A. Stein, and D. J. Norris, "Tailoring self-assembled metallic photonic crystals for modified thermal emission," Phys. Rev. Lett. **99**, 053906 (2007).

[7] S.-Y. Lin, J. Moreno, and J. G. Fleming, "Three-dimensional photonic-crystal emitter for thermal photovoltaic power generation," Appl. Phys. Lett. **83**, 380-382 (2003).

[8] P. Nagpal, S. E. Han, A. Stein, and D. J. Norris, "Efficient low-temperature thermophotovoltaic emitters from metallic photonic crystals," Nano Lett. **8**, 3238-3243 (2008).

[9] J. D. Joannopoulos, R. D. Meade, and J. N. Winn, *Photonic crystals: Molding the flow of light* (Princeton Univ. Press, New York, 1995).

[10] L. D. Landau and E. M. Lifshitz, *Electrodynamics of continuous media* (Pergamon, Oxford, 1984).

[11] S. M. Rytov, Y. A. Kravtsov, and V. I. Tatarskii, *Principles of statistical radiophysics, Vol. 3: Elements of random fields* (Springer-Verlag, Berlin, 1989).

[12] R. Sprik, B. A. van Tiggelen, and A. Lagendijk, "Optical emission in periodic dielectrics," Europhys. Lett. **35**, 265-270 (1996).

[13] P. Lodahl, A. F. van Driel, I. S. Nikolaev, A. Irman, K. Overgaag, D. Vanmaekelbergh, and W. L. Vos, "Controlling the dynamics of spontaneous emission from quantum dots by photonic crystals," Nature **430**, 654-657 (2004).

[14] Throughout this chapter, we used the transfer matrix formalism and the unit cell was discretized by a 96×96 mesh.

[15] D. W. Lynch and W. R. Hunter, in *Handbook of optical constants of solids*, edited by E. D. Palik (Academic Press, Orlando, 1985).

[16] L. D. Landau and E. M. Lifshitz, *Statistical physics, Part 1* (Pergamon, Oxford, 1984).

[17] R. B. Bird, W. E. Stewart, and E. N. Lightfoot, *Transport phenomena* (John Wiley & Sons, 1960).

[18] J.-P. Mulet, K. Joulain, R. Carminati, and J.-J. Greffet, Appl. Phys. Lett. "Nanoscale radiative heat transfer between a small particle and a plane surface," **78**, 2931-2933 (2001).

[19] J. J. Loomis and H. J. Maris, "Theory of heat transfer by evanescent electromagnetic waves," Phys. Rev. B **50**, 18517-18524 (1994).

[20] J. L. Pan, "Radiative transfer over small distances from a heated metal," Opt. Lett. **25**, 369-371 (2000).

[21] A. I. Volokitin and B. N. J. Persson, "Radiative heat transfer between nanostructures," Phys. Rev. B **63**, 205404 (2001).

[22] M. D. Whale and E. G. Cravalho, "Modeling and performance of microscale thermophotovoltaic energy conversion devices," IEEE Trans. Energy Convers. **17**, 130-142 (2002).

[23] A. Narayanaswamy and G. Chen, "Surface modes for near field thermophotovoltaics," Appl. Phys. Lett. **82**, 3544-3546 (2003).

[24] M. Janowicz, D. Reddig, and M. Holthaus, "Quantum approach to electromagnetic energy transfer between two dielectric bodies," Phys. Rev. A **68**, 043823 (2003).

[25] S. K. Lamoreaux, "The Casimir force: background, experiments, and applications," Rep. Prog. Phys. **68**, 201-236 (2005).

[26] M. Laroche, R. Carminati, and J.-J. Greffet, "Near-field thermophotovoltaic energy conversion," J. Appl. Phys. **100**, 063704 (2006).

[27] B. J. Lee, K. Park, and Z. M. Zhang, "Energy pathways in nanoscale thermal radiation," Appl. Phys. Lett. **91**, 153101 (2007).

[28] S. A. Biehs, "Thermal heat radiation, near-field energy density and near-field radiative heat transfer of coated materials," Eur. Phys. J. B **58**, 423-431 (2007).

[29] P.-O. Chapuis, S. Volz, C. Henkel, K. Joulain, and J.-J. Greffet, "Effects of spatial dispersion in near-field radiative heat transfer between two parallel metallic surfaces," Phys. Rev. B **77**, 035431 (2008).

[30] A. Kittel, W. Müller-Hirsch, J. Parisi, S.-A. Biehs, D. Reddig, and M. Holthaus, "Near-field feat transfer in a scanning thermal microscope," Phys. Rev. Lett. **95**, 224301 (2005).

[31] D. R. Lide, *CRC handbook of chemistry and physics*, (CRC Press, 1978).

Chapter 4

Tailoring Inverse Opals for Modified Thermal Emission*

"Physics is essentially an intuitive and concrete science."

Albert Einstein

4.1 Introduction

A photonic crystal is a structure that is periodic on an optical length scale [1]. This periodicity can affect not only the optical transmission and reflection of the material, but also its thermal emission [2]. For example, a specific photonic crystal, the tungsten woodpile structure, has exhibited modified thermal emission when heated [3, 4, 5, 6, 7, 8]. This arises because the photonic density of states is altered in the crystal. Even though

* Much of Chapter 4 has appeared in print:
S. E. Han, A. Stein, and D. J. Norris, Phys. Rev. Lett. **99**, 053906 (2007).
Around the time of these publications, an interesting similar work was also reported:
X. Yu, Y.-J. Lee, R. Furstenberg, J. O. White, and P. V. Braun, Adv. Mater. **19**, 1689-1692 (2007).

a previous experiment [4] reportedly observed an emission exceeding Planck's blackbody limit, this is not plausible on theoretical grounds [9, 10, 11, 12, 13]. A complete theoretical proof for this is given in Chapter 2. Recent experiments also confirm these theoretical results [3, 14, 15]. However, the potential for these crystals to suppress emission at certain wavelengths (e.g., unwanted heat) is clear. They may allow more efficient emission sources and thermophotovoltaic systems to be obtained.

Unfortunately, the woodpile structure (see inset in Fig. 4.1) requires a complex fabrication process, which has limited its use in the study of thermal emission. A simpler approach would be to use self-assembly. Micrometer-scale colloidal spheres can be organized as a thin face-centered cubic (fcc) crystal on a substrate [16]. The crystal can then be infiltrated and the spheres removed to obtain a structure, known as an inverse opal, in which an fcc array of air-spheres is embedded in a film [17, 18, 19, 20]. Indeed, tungsten inverse opals have recently been made [21, 22], and these could be used to study thermal emission. However, experiments on these crystals revealed that they suffer from extremely strong optical absorption. Essentially, propagating light is absorbed before it senses the periodic structure, eliminating any influence of the photonic crystal. While Kirchhoff's law states that absorption is needed for thermal emission, clearly the absorption should not be severe. If it is, modification of thermal emission by the photonic crystal will not occur. Thus, previous work suggested that inverse opals were ill-suited for studying thermal emission.

In this chapter, we re-examine the physics of inverse opals for thermal emission. In particular, we seek to understand the severe absorption in these structures, and to determine if it is intrinsic or can be moderated. For thermal emission modification, the absorption should be significant, but not so strong that the periodicity does not play a role. Previously, thermal emission was treated theoretically for silicon inverse opals [23]. Here, as in the woodpile studies, we begin with tungsten. Because of its extremely high melting temperature (3414 °C), tungsten structures allow thermal emission to be studied over a broad temperature range. We then consider other refractory metals such as

molybdenum and tantalum. Surprisingly, we find that small, experimentally realizable changes in metallic inverse opals can lead to optical properties that are very similar to or even better than the tungsten woodpile. Thus, this new inverse opal structure, which is easily prepared, has great potential for both thermal emission studies and applications.

4.2 Theoretical Analysis

To determine how tungsten inverse opals can exhibit modified thermal emission, we need physical intuition about the origin of the absorption. Then, perhaps we can increase the spatial decay length via small structural changes. Following Krokhin and Halevi [24], we consider an infinite photonic crystal composed of a weakly dissipating material, m, and air, a. The complex magnetic field in the nth photonic band takes the Bloch form

$$\boldsymbol{H_k}^{(n)}(\boldsymbol{r}) = \sum_{\boldsymbol{G}} \boldsymbol{h_k}^{(n)}(\boldsymbol{G}) e^{i(\boldsymbol{k}+\boldsymbol{G})\cdot\boldsymbol{r}} \ , \tag{4.1}$$

where $\boldsymbol{k}$ is the wavevector, $\boldsymbol{G}$ is the reciprocal lattice vector, and $\boldsymbol{h}$ is the complex orthonormal basis vector,

$$\sum_{\boldsymbol{G}} \boldsymbol{h_k}^{*(n)}(\boldsymbol{G}) \cdot \boldsymbol{h_k}^{(n')}(\boldsymbol{G}) = \delta_{n,n'} \ . \tag{4.2}$$

If we express the dielectric function of the material in complex form as $\varepsilon'_m + i\varepsilon''_m$ and the angular frequency as $\omega' + i\omega''$, then the temporal decay rate, ω'', is

$$\omega''_n(\boldsymbol{k}) = \frac{\varepsilon''_m}{2\varepsilon'_m(\varepsilon'_m - 1)} \left[1 - \frac{c^2}{\omega'^2_n(\boldsymbol{k})} \sum_{\boldsymbol{G}} |\boldsymbol{k}+\boldsymbol{G}|^2 |\boldsymbol{h_k}^{(n)}(\boldsymbol{G})|^2 \right] \omega'_n(\boldsymbol{k}), \tag{4.3}$$

with c as the velocity of light [24]. It is useful to rewrite Eq. (4.3) in terms of the field in real space by using Parseval's theorem and Maxwell's equations such that

$$\frac{\omega''_n(\boldsymbol{k})}{\omega'_n(\boldsymbol{k})} = \frac{\varepsilon''_m}{2\varepsilon'_m(\varepsilon'_m - 1)} \left[1 - \frac{\int_{V_c} |\boldsymbol{D_k}^{(n)}(\boldsymbol{r})|^2 d\boldsymbol{r}}{\int_{V_c} |\boldsymbol{H_k}^{(n)}(\boldsymbol{r})|^2 d\boldsymbol{r}} \right], \tag{4.4}$$

where V_c is the volume of the unit cell and $\boldsymbol{D}$ is the complex displacement field, defined as in Eq. (4.1). Now, we assume that material m is a metal with a magnetic permeability

of 1 and $\varepsilon'_m \ll 0$. Moreover, the thickness and radius of curvature of the structured metal are always much greater than the skin depth, δ. Then, on separating the unit cell into metal and air parts with volumes V_m and V_a, Eq. (4.4) becomes approximately

$$\omega''_n(\boldsymbol{k}) \approx -\frac{\varepsilon''_m}{2}\left[\frac{\int_{V_m}|\boldsymbol{E_k}^{(n)}(\boldsymbol{r})|^2 d\boldsymbol{r}}{\int_{V_a}|\boldsymbol{E_k}^{(n)}(\boldsymbol{r})|^2 d\boldsymbol{r}}\right]\omega'_n(\boldsymbol{k}), \tag{4.5}$$

where $\boldsymbol{E}$ is the complex electric field, as in Eq. (4.1). So far, $\boldsymbol{k}$ has been treated as a real quantity. If we now regard $\boldsymbol{k}$ as complex, $\boldsymbol{k}' + i\boldsymbol{k}''$, the spatial decay length is inversely proportional to $\boldsymbol{k}''$ and, in the limit of weak dissipation, $\boldsymbol{k}'' = -\omega''/\boldsymbol{v}_g$, where $\boldsymbol{v}_g$ is the group velocity [24]. Thus, to increase the spatial decay length, we need to increase the group velocity and/or decrease ω''. Equation (4.5) allows ω'' to be quantified from the distribution of the field. Physically, it states that ω'' is related to the ratio of the field intensity in the metal to that in the air, which, in turn, is roughly proportional to $S_m\delta/V_a$, where S_m is the surface area of the metal in the unit cell. Thus, we need to decrease S_m/V_a by altering the inverse opal structure.

4.3 Numerical Calculations

Before tailoring the inverse opal, we consider the photonic band diagram and optical spectra for the tungsten woodpile. The calculations of these were done using the transfer matrix formalism combined with the multiple scattering technique [25]. The latter was added to ensure numerical stability. The results, shown in Fig. 4.1, were obtained for the structure reported previously [5], except our crystal is 10 layers thick. Unless stated otherwise, we used the actual complex dielectric function of all metals in this work [26] however the imaginary part was set to zero in all band structure calculations. From the band diagram (Fig. 4.1a) we can identify two groups of bands, one below 0.6 and the other above 0.64 eV. The two peaks in absorption (Fig. 4.1b) correspond to these two groups. Previous thermal emission experiments [5] utilized the upper frequency peak, which is stronger. In this frequency range, transmission is appreciable, suggesting that

light is not severely damped but rather interacting with the periodic structure.

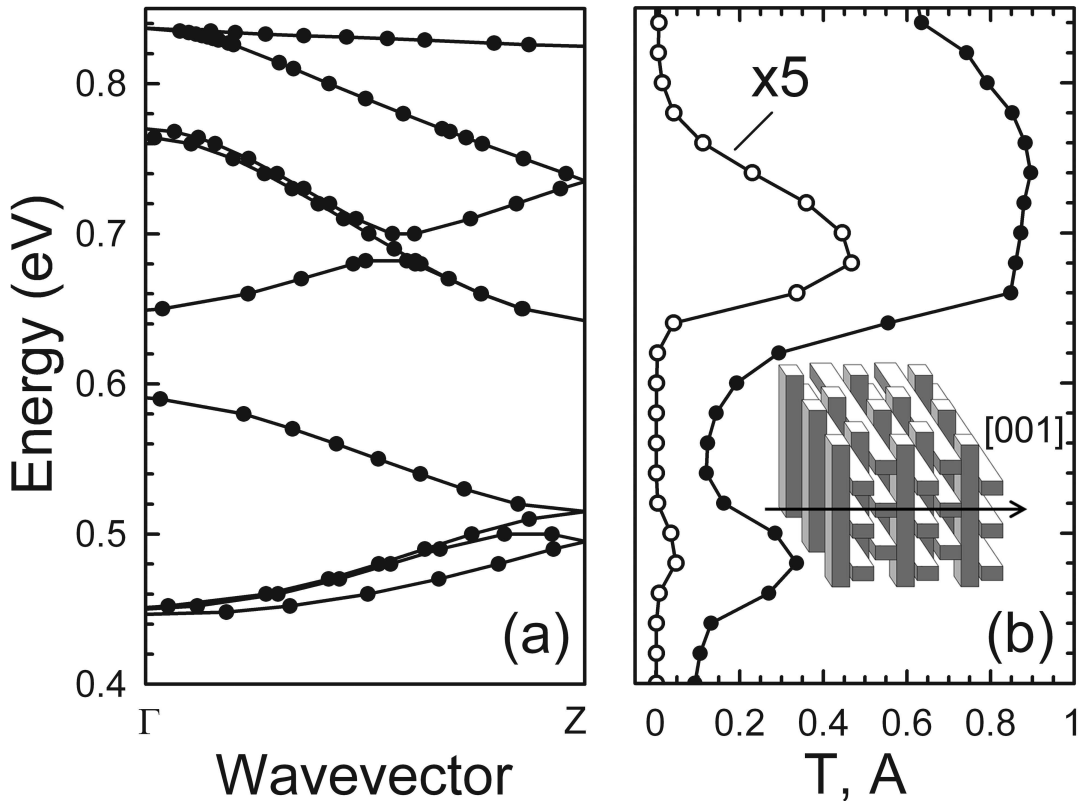

Figure 4.1: Calculated (a) photonic band structure and (b) transmittance, T (open circles), and absorptance, A (solid circles), along [001] for a 10-layer tungsten woodpile (see inset). The rod width, height, and spacing are 0.5, 0.75, and 1.5 μm, respectively, so that the total thickness is 7.5 μm. No bands exist below 0.4 eV. T values are scaled by a factor of 5.

Based on the analysis in the previous section, we now want to discuss how we can tailor the inverse opal. We considered several simple alterations to the inverse opal. The most promising involves the insertion of air-cylinders into the structure at the contact points between the air-spheres. The cylinders are oriented along the lines connecting the centers of the spheres. Outside of these spheres and cylinders, the structure is filled with metal. This alteration is advantageous for three reasons. First, the cylinders decrease S_m/V_a. For example, when the cylinder diameter, d, is half of the sphere diameter, D,

S_m/V_a is 52% of its value without the cylinders. Second, the cylinders allow the air-spheres to interact, resulting in band broadening and an increase in the group velocity [27]. Finally, and perhaps most importantly, experimental techniques already exist to add such cylinders to inverse opals [22, 28].

Figure 4.2 describes how the optical properties of the metallic inverse opals vary with air-cylinder diameter. Specifically, it describes how v_g/c and k'' vary for inverse opals as a function of d/D in the limit of weak absorption. To obtain these plots we assumed a constant dielectric function with weak absorption ($\varepsilon_m = -100 + 0.01i$) and determined the band diagram for the ΓL direction (*i.e.*, [111]) for a range of cylinder diameters. More specifically, we calculated how k' and k'' vary with frequency. From these band diagrams, two groups of bands (lower and upper) could be identified, as in Fig. 4.1a. For each group, we extracted the minimum value of k''/ε_m'' and v_g/c at the same frequency. Note that because $\varepsilon_m'' \ll |\varepsilon_m'|$, v_g still has meaning. Also, because a constant ε_m was used, the frequency is scalable, and values for the woodpile structure could be compared. The resulting plots are useful for two reasons. First, recalling that the spatial decay length is inversely proportional to k'', Fig. 4.2b shows that the spatial decay length increases with cylinder diameter. As k'' is, in turn, inversely proportional to v_g, Fig. 4.2a indicates that this increase is due in part to an increase in the group velocity. Because our goal is to lengthen the spatial decay, these plots suggest that we should use a cylinder with the largest possible diameter. However, the inverse opal becomes disconnected when $d/D > 0.577$. Thus, to ensure mechanical stability we use $d/D = 0.5$ below, corresponding to a reasonable metal filling fraction of 15%. Such a structure is depicted in Fig. 4.3. Second, the plots in Fig. 4.2 were constructed to allow comparison with values for the woodpile, shown as horizontal lines. For $d/D = 0.5$, Fig. 4.2b shows that the spatial decay length in the inverse opal should be only slightly shorter than in the woodpile for the upper group of bands. Moreover, it should actually be longer for the lower group of bands. Thus, this plot indicates that absorption in inverse opals can be moderated by inserting air cylinders. This decrease in absorption is not due

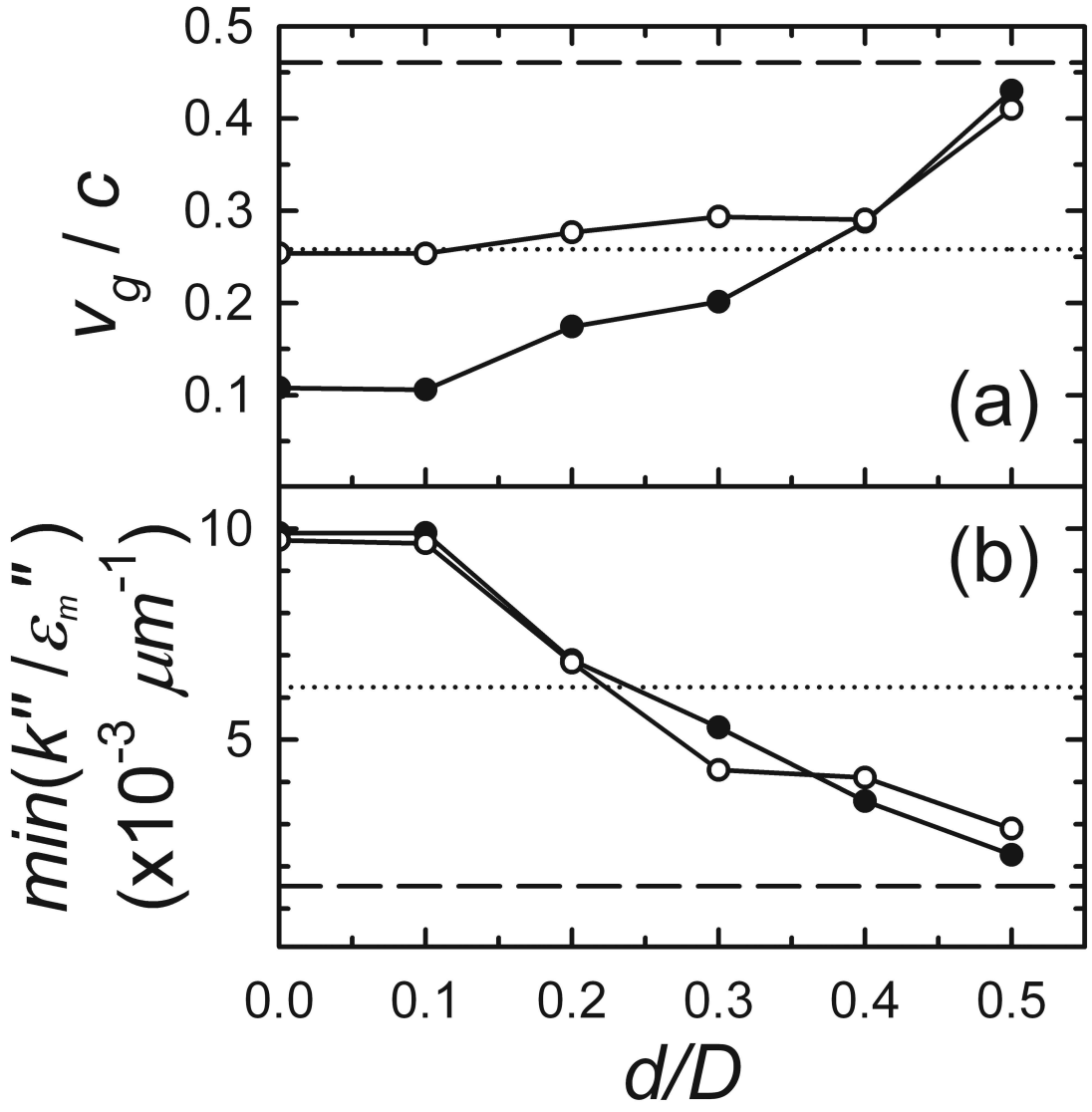

Figure 4.2: (a) Normalized group velocity and (b) the minimum of k''/ε''_m vs. d/D along [111] for the inverse opal. These values are extracted from the frequency dependence of k' and k'' in the limit of vanishing ε''_m. Results are plotted for the lowest frequency group of bands (solid circles) and the next group of bands (open circles). For comparison, values for the lowest group of bands (dotted line) and the second group of bands (dashed line) for the woodpile are also shown. A constant $\varepsilon_m = -100 + 0.01i$ was used.

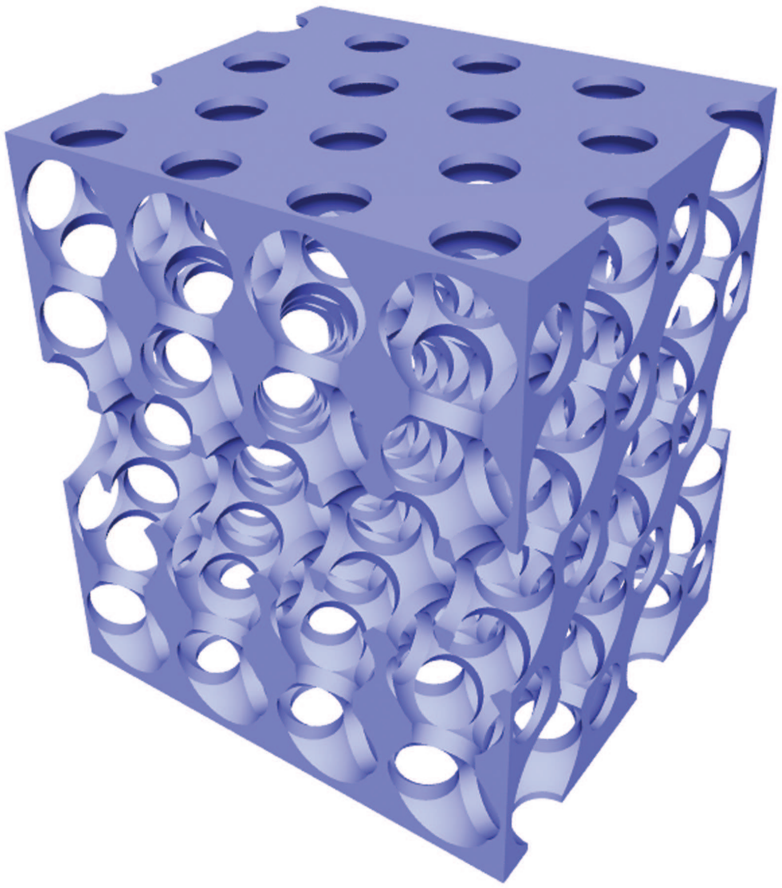

Figure 4.3: A computer generated image of a tailored 5-layer inverse opal. Air-cylinders are inserted along the lines between the center of the air-spheres. The diameter of the air-cylinders is half of the sphere diameter. The outer surfaces of the structure are chosen to be (111) planes, as observed in experiment. Due to the infiltration process that would be used during fabrication, these outer surfaces would be thin metal films perforated by a hexagonal array of cylindrical holes, as shown.

simply to a lower filling fraction of the metal. Without air-cylinders, the absorption increased with decreasing filling fraction. Further, the tailored structure may exhibit optical behavior comparable to the woodpile, at least at certain frequencies.

Before testing this, we must first consider how light in the structure couples to the external field. This coupling, which also affects the optical properties of the crystal, is determined by both the symmetry of the eigenmodes and the surface geometry. For thin self-assembled colloidal crystals, the external surfaces are typically hexagonally close-packed sheets of spheres that are perpendicular to the ΓL direction. If such a crystal is grown between two substrates and then processed to obtain a free-standing inverse opal, the air-cylinders discussed above will also arise at the contact points between the substrates and the outer spheres. Thus, the two external surfaces will be flat metal interfaces perforated by a hexagonal array of cylindrical holes with diameter d. This surface geometry is similar to the metal hole arrays that have been investigated for extraordinary optical transmission [29, 30]. In that case, enhanced transmission occurs near the frequencies of surface plasmons. For normal incidence, the plasmon frequency of a hexagonal hole array is given by

$$\frac{\omega D}{2\pi c} = 2\sqrt{\frac{(i^2+ij+j^2)(\varepsilon'_m+1)}{3\varepsilon'_m}}, \tag{4.6}$$

where i and j are integers. The transmission peaks will be located where $\omega D/2\pi c$ is near 1, corresponding to the lowest surface plasmon frequency modes given by $(i,j) = (\pm 1, 0), (0, \pm 1), (1, -1)$, and $(-1, 1)$.

As in previous studies on two-dimensional photonic crystals [31], we examined how this surface influences the optical properties. The calculated reflectance for the outermost half-layer of the structure, including the air-cylinders, is shown in Fig. 4.4a for $\varepsilon_m = -100+27i$. A reflectance dip (or transmission peak) occurs near the frequency predicted by Eq. (4.6). For comparison, Fig. 4.4b shows the calculated band diagram for a tailored inverse opal assuming $\varepsilon_m = -100$. Because the reflection dip of the surface (Fig. 4.4a) overlaps with the upper group of bands, *i.e.*, above $\omega D/2\pi c = 0.8$, one

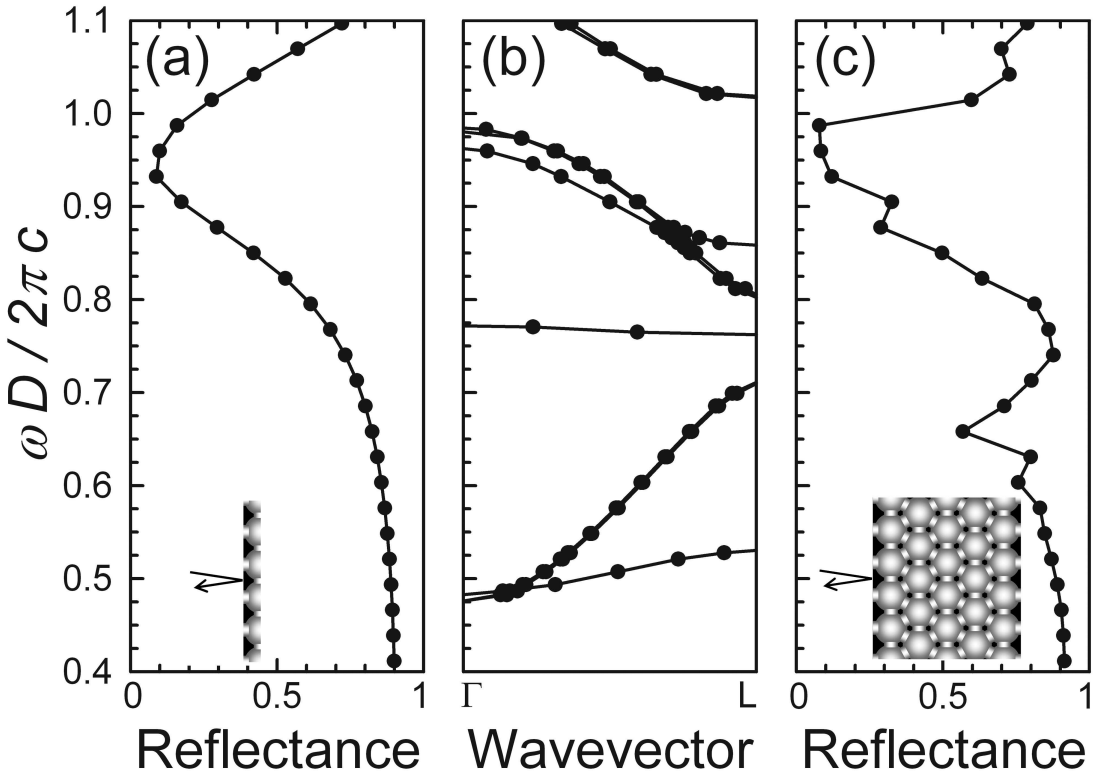

Figure 4.4: (a) Calculated reflectance for normal incidence on the top half-layer of the inverse opal with air-cylinders, using $\varepsilon_m = -100 + 27i$ and $d/D = 0.5$. (b) Photonic band structure along [111] for an inverse opal with air-cylinders, using $\varepsilon_m = -100$ and $d/D = 0.5$. No bands exist below 0.4. (c) Calculated reflectance for normal incidence along [111] for a 5-layer inverse opal as in (b) except $\varepsilon_m = -100 + 27i$. The insets show schematic side views of the structures.

might expect to see the best coupling to the external field in this region for a tailored 5-layer inverse opal. Figure 4.4c shows the calculated reflectance for such a structure with ε_m=−100+27i. Indeed, the reflectance dip for the lower group of bands (*i.e.*, at $\omega D/2\pi c = 0.66$) is weaker than one would expect based solely on the spatial decay length discussed above. The surface is effectively blocking the incident light at these frequencies. Thus, below we utilize the upper group of bands, which couple to the external field strongly, even though the spatial decay here is slightly shorter than in the woodpile.

We can then adjust the lattice constant of the crystal to locate the absorption peak in the near-infrared region to compare with the woodpile results. As Fig. 4.4c suggests that the absorption peak in the inverse opal should occur around $\omega D/2\pi c = D/\lambda = 1$, we choose $D = 1.7\mu m$ to place the peak near this wavelength. Figures 4.5a and b show results for a tailored 5-layer tungsten inverse opal in Fig. 4.3 along the ΓL direction. The absorption peak (Fig. 4.5b) occurs at 0.68 eV or $\lambda = 1.82\mu m$. Comparison with Fig. 4.1b reveals that the optical spectra of the tailored tungsten inverse opal are quite similar to those of the tungsten woodpile. The absorption peak of the inverse opal is even narrower, which may be advantageous for some applications. The maximum transmittance is 0.03 for the tungsten inverse opal, which has a thickness of $7.25\mu m$, compared to 0.09 for the tungsten woodpile in Fig. 4.1, which is $7.5\mu m$ thick. The difference in transmittance can be explained by Fig. 4.2b, which indicates that the spatial decay length is longer in the tungsten woodpile than the tailored inverse opal for the upper group of bands.

To test further our tailored structure, we performed several additional calculations. First, Fig. 4.6 shows the calculated band structure and optical properties for another orientation of the crystal. Figure 4.6a shows the calculated band structure and Fig. 4.6b shows the optical spectra for the ΓX direction (*i.e.*, [001]). These results are quite similar to those for the ΓL direction (Fig. 4.5b), indicating that thermal emission from several external facets of the crystal should act similarly. Second, Figs. 4.5c and d

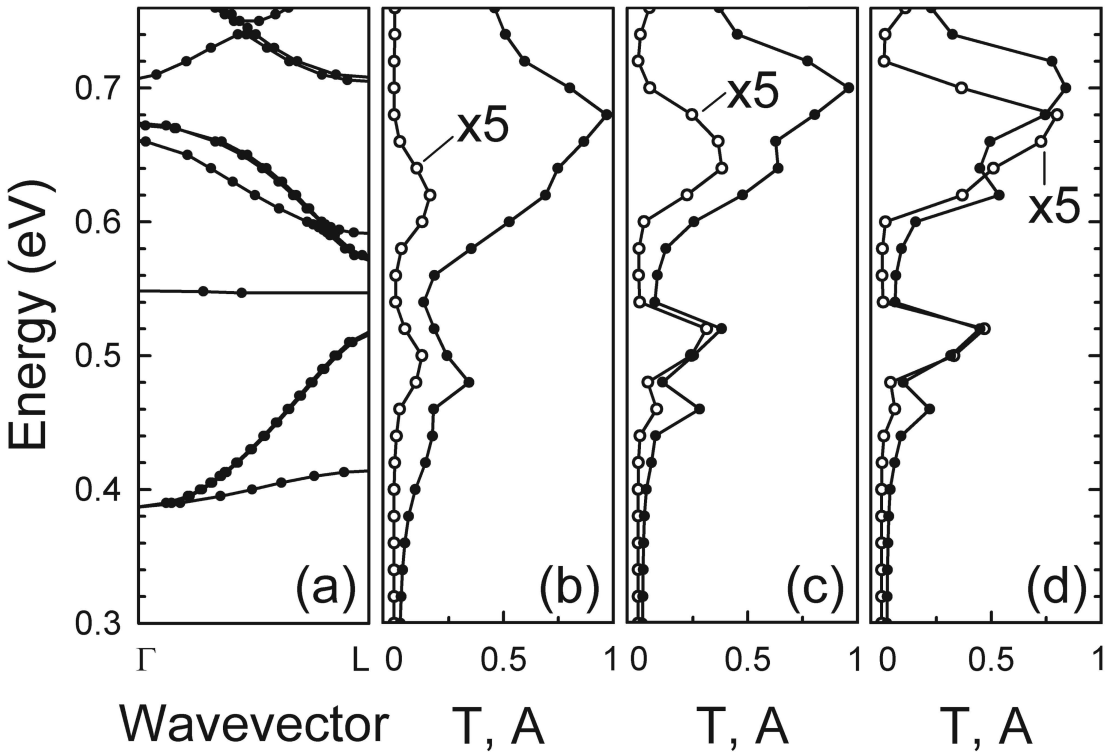

Figure 4.5: (a) Calculated photonic band structure and (b) optical transmittance, T (open circles), and absorptance, A (solid circles), along [111] for a 5-layer tungsten inverse opal with air-cylinders. (c) and (d) show calculations for analogous structures from molybdenum and tantalum, respectively. For all, we used $D = 1.7\mu m$, $d/D = 0.5$. T values are scaled by a factor of 5. In (a) no bands exist below 0.3 eV.

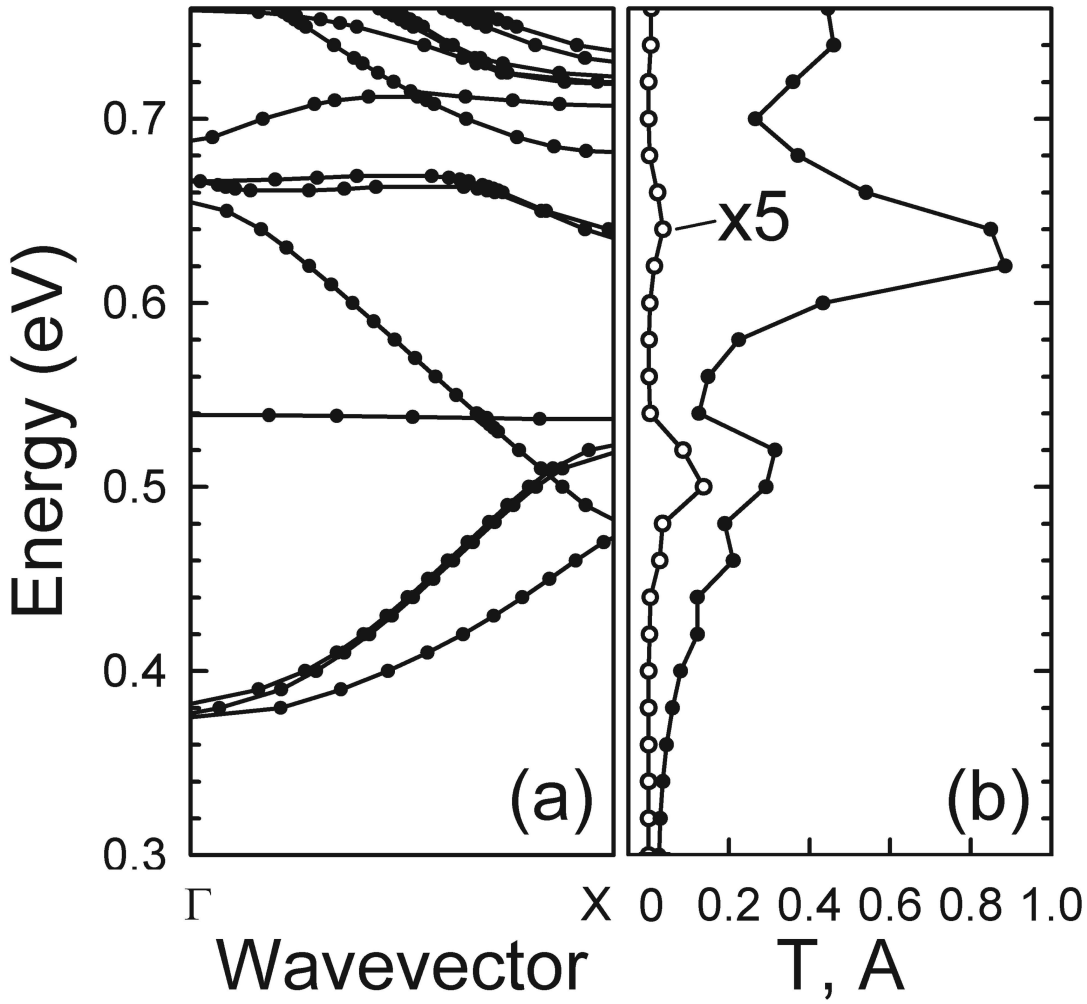

Figure 4.6: (a) The calculated photonic band structure along [001] for a 5-layer tungsten inverse opal with air-cylinders. (b) Calculated optical transmittance, T (open circles), and absorptance, A (solid circles), along [001] for a 5-layer tungsten inverse opals with air-cylinders. We used $D = 1.7\mu m$, $d/D = 0.5$, and the actual dielectric function of tungsten. However, the imaginary component of the dielectric function was set to zero in (a). Transmittance values are scaled by a factor of 5. In (a), no bands exist below 0.3 eV.

present optical spectra along the ΓL direction for our tailored inverse opal made from Mo and Ta, respectively. These spectra show that the transmission can be even higher than the tungsten woodpile. Thus, by compromising slightly on the melting temperature of the metal (2622 and 3007 °C for Mo and Ta, respectively), even better properties may be possible.

The choice of materials was based on their melting points and their absorptance for a flat surface in the normal direction at $\lambda = 1.5\mu m$ (see Table 4.1). The normal absorptance was used as a rough measure of the expected absorptive properties of the inverse opal. For example, when the absorptance is low, we expect that the inverse opals made from the material will also exhibit low absorption. Table 4.1 lists the normal absorptance of the elements which have melting points above 2000 °C. From this, we expect that Ta, Nb, and Mo may be useful as a material for inverse opals. However, it should be noted that factors other than the melting point should also be considered such as the vapor pressure and the susceptibility to grain coarsening, and recrystallization of the materials. Moreover, as the structural dimensions are reduced from macroscopic size to several hundred nanometers, the structures can become less stable at high temperatures. Progress in increasing the high temperature stability of tungsten inverse opals has been recently demonstrated by using alloys of tungsten and molybdenum [32].

Table 4.1: The melting point and absorptance of elements whose melting point is above 2000 °C. The absorptance is for a flat surface illuminated in the normal direction at $\lambda = 1.5\mu m$.

element†	W	Re	Os	Ta	Mo	Nb	Ir	Ru	Hf
Melting point (°C)	3414	3186	3033	3007	2622	2477	2446	2333	2233
Absorptance	.302	.156	.193	.050	.110	.079	.144	.209	.488

† Technetium (Tc) is not included due to the absence of available optical data.

4.4 Conclusion

We predict that metallic inverse opals can be tailored to have optical properties similar to or even better than the tungsten woodpile. By inserting air-cylinders and considering the coupling to the external field, these inverse opals should exhibit optical absorption that, while still significant, is sufficiently moderated that the periodicity of the photonic crystal will have an effect. Because Kirchhoff's law relates thermal emission directly to absorption, such structures should exhibit modified thermal emission. Moreover, these inverse opals are experimentally realizable and have external surfaces, *i.e.*, flat with an array of cylindrical holes, that are convenient for predicting coupling to the external field. Thus, these self-assembled photonic crystals have great potential for experimental studies and applications of modified thermal emission.

References

[1] J. D. Joannopoulos, P. R. Villeneuve, and S. Fan, "Photonic crystals: Putting a new twist on light," Nature **386**, 143-149 (1997).

[2] C. M. Cornelius and J. P. Dowling, "Modification of Planck blackbody radiation by photonic band-gap structures," Phys. Rev. A **59**, 4736-4746 (1999).

[3] J. G. Fleming, S.-Y. Lin, I. El-Kady, R. Biswas, and K. M. Ho, "All-metallic three-dimensional photonic crystals with a large infrared bandgap," Nature **417**, 52-55 (2002).

[4] S.-Y. Lin, J. G. Fleming, E. Chow, J. Bur, K. K. Choi, and A. Goldberg, "Three-dimensional photonic-crystal emitter for thermal photovoltaic power generation," Phys. Rev. B **62**, R2243-R2246 (2000).

[5] S.-Y. Lin, J. Moreno, and J. G. Fleming, "Three-dimensional photonic-crystal emitter for thermal photovoltaic power generation," Appl. Phys. Lett. **83**, 380-382 (2003).

[6] S.-Y. Lin, J. G. Fleming, and I. El-Kady, "Experimental observation of photonic-crystal emission near a photonic band edge," Appl. Phys. Lett. **83**, 593-595 (2003).

[7] S.-Y. Lin, J. G. Fleming, and I. El-Kady, "Highly efficient light emission at $\lambda = 1.5$ μm by a three-dimensional tungsten photonic crystal," Opt. Lett. **28**, 1683-1685 (2003).

[8] S.-Y. Lin, J. G. Fleming, Z. Y. Li, I. El-Kady, R. Biswas, and K. M. Ho, "Origin of absorption enhancement in a tungsten, three-dimensional photonic crystal," J. Opt. Soc. Am. B **20**, 1538-1541 (2003).

[9] T. Trupke, P. Wurfel, and M. A. Green, "Comment on "Three-dimensional photonic-crystal emitter for thermal photovoltaic power generation" [Appl. Phys. Lett. 83, 380 (2003)]" Appl. Phys. Lett. **84**, 1997-1998 (2004).

[10] C. Luo, A. Narayanaswamy, G. Chen, and J. D. Joannopoulos, "Thermal radiation from photonic crystals: A direct calculation," Phys. Rev. Lett. **93**, 213905 (2004).

[11] W. W. Chow, "Theory of emission from an active photonic lattice," Phys. Rev. A **73**, 013821 (2006).

[12] W. W. Chow and I. Waldmueller, "Active photonic lattices: Is greater than blackbody intensity possible?" J. Mod. Opt. **53**, 2371-2376 (2006).

[13] I. El-Kady, W. W. Chow, and J. G. Fleming, "Emission from an active photonic crystal," Phys. Rev. B **72**, 195110 (2005).

[14] J. G. Fleming, "Addendum: "Three-dimensional photonic-crystal emitter for thermal photovoltaic power generation" [Appl. Phys. Lett. 83, 380 (2003)]" Appl. Phys. Lett. **86**, 249902 (2005).

[15] C. H. Seager, M. B. Sinclair, and J. G. Fleming, "Accurate measurements of thermal radiation from a tungsten photonic lattice," Appl. Phys. Lett. **86**, 244105 (2005).

[16] P. Jiang, J. F. Bertone, K. S. Hwang, and V. L. Colvin, "Single-crystal colloidal multilayers of controlled thickness," Chem. Mater. **11**, 2132-2140 (1999).

[17] B. T. Holland, C. F. Blanford, and A. Stein, "Synthesis of macroporous minerals with highly ordered three-dimensional arrays of spheroidal voids," Science **281**, 538-540 (1998).

[18] J. E. G. J. Wijnhoven and W. L. Vos, "Preparation of photonic crystals made of air spheres in titania," Science **281**, 802 (1998).

[19] A. Blanco, E. Chomski, S. Grabtchak, M. Ibisate, S. John, S. W. Leonard, C. López, F. Meseguer, H. Míguez, J. P. Mondia, G. A. Ozin, O. Toader, and H. M. van Driel, "Large-scale synthesis of a silicon photonic crystal with a complete three-dimensional bandgap near 1.5 micrometres," Nature **405**, 437-440 (2000).

[20] Y. A. Vlasov, X. Z. Bo, J. C. Sturm, and D. J. Norris, "On-chip natural assembly of silicon photonic bandgap crystals," Nature **414**, 289-293 (2001).

[21] G. von Freymann, S. John, M. Schulz-Dobrick, E. Vekris, N. Tetreault, S. Wong, V. Kitaev, and G. A. Ozin, "Tungsten inverse opals: The influence of absorption on the photonic band structure in the visible spectral region," Appl. Phys. Lett. **84**, 224-226 (2004).

[22] N. R. Denny, S. Han, R. T. Turgeon, J. C. Lytle, D. J. Norris, and A. Stein, "Synthetic approaches toward tungsten photonic crystals for thermal emission," SPIE Proc. **6005**, 60050501 (2005).

[23] M. Florescu, H. Lee, A. J. Stimpson, and J. Dowling, "Thermal emission and absorption of radiation in finite inverted-opal photonic crystals," Phys. Rev. A **72**, 033821 (2005).

[24] A. A. Krokhin and P. Halevi, "Influence of weak dissipation on the photonic band structure of periodic composites," Phys. Rev. B **53**, 1205-1214 (1996).

[25] P. M. Bell, J. B. Pendry, L. Martin-Moreno, and A. J. Ward, "A program for calculating photonic band structures and transmission coefficients of complex structures," Comput. Phys. Commun. **85**, 306 (1995).

[26] D. W. Lynch and W. R. Hunter, in *Handbook of optical constants of solids*, edited by E. D. Palik (Academic Press, Orlando, 1985).

[27] A. L. Pokrovsky, V. Kamaev, C. Y. Li, Z. V. Vardeny, A. L. Efros, D. A. Kurdyukov, V. G. Golubev, "Theoretical and experimental studies of metal-infiltrated opals," Phys. Rev. B **71**, 165114 (2005).

[28] J. S. King, D. P. Gaillot, E. Graugnard, and C. J. Summers, "Conformally back-filled, non-close-packed inverse-opal photonic crystals," Adv. Mater. **18**, 1063-1067 (2006).

[29] T. W. Ebbesen, H. J. Lezec, H. F. Ghaemi, T. Thio, and P. A. Wolff, "Extraordinary optical transmission through sub-wavelength hole arrays," Nature **391**, 667-669 (1998).

[30] H. F. Ghaemi, T. Thio, D. E. Grupp, T. W. Ebbesen, and H. J. Lezec, "Surface plasmons enhance optical transmission through subwavelength holes," Phys. Rev. B **58**, 6779-6782 (1998).

[31] R. Biswas, C. G. Ding, I. Puscasu, M. Pralle, M. McNeal, J. Daly, A. Greenwald, and E. Johnson, "Theory of subwavelength hole arrays coupled with photonic crystals for extraordinary thermal emission," Phys. Rev. B **74**, 045107 (2006).

[32] N. R. Denny, S. E. Han, D. J. Norris, and A. Stein, "Structural effects of thermal emission on monolithic tungsten and tungsten alloy photonic crystals," Chem. Mater. **19**, 4563-4569 (2007).

Chapter 5

Beaming Thermal Emission from Metallic Bull's Eyes*

"Their wings were joined one to another;
they turned not when they went;
they went every one straight forward."

Ezekiel 1:9

5.1 Introduction

Electromagnetic waves known as surface plasmons polaritons (SPPs) can be excited at the surface of a metal [1]. These waves propagate at the interface with an intensity that decays both in the bulk metal and the surrounding medium. Because they can occur at optical frequencies, they allow interesting interactions with light. In particular, when light is coupled to SPPs, the optical field can be concentrated in extremely small volumes. This has implications for applications from sensors to solar energy [2]. Earlier,

* Much of Chapter 5 will appear in print: S. E. Han, P. Nagpal, and D. J. Norris, Phys. Rev. Lett. (submitted).

this effect was mostly applied in spectroscopic techniques such as surface enhanced raman spectroscopy, where intense local fields can provide high sensitivity. More recently, the ability to couple light to SPPs has been examined for reducing optical circuit elements (waveguides, switches, *etc.*) to sizes smaller than the optical wavelength [3, 4]. As a result, the field of plasmonics has arisen to study how man-made metallic structures can control the generation and manipulation of SPPs.

This was encouraged in part by the unexpected observation of extraordinary optical transmission through thin metal films perforated with an array of sub-wavelength holes [5]. Because the holes are periodically spaced, diffraction can excite SPPs when one side of the film is illuminated. The SPPs can then transmit energy through the holes and re-radiate on the opposite side of the film. This can lead to transmission much higher than would be expected for sub-wavelength holes. More recently, the same effect was observed when a single hole in a metal film was surrounded by circular concentric grooves patterned on both sides of the film [6]. In this structure, referred to as a bull's eye, the SPPs interact with the grooves to couple in and out of the film. More importantly, even with a sub-wavelength hole, the bull's eye produces an output beam that is directional [7], a useful property.

However, in these experiments light was utilized to create the SPPs. Indeed, most of plasmonics uses an optical source. An alternative that has only begun to be explored in these devices is thermal excitation of SPPs [8]. For example, SPPs could be produced electrically by heating either the entire structure or a specific location within it. Because plasmonic devices can be small, very low power would be required. Through proper design, the resulting SPPs could be launched with specific properties. Additional flexibility and new phenomena could result.

As one example, here we study thermal emission from metallic bull's eyes. Our structures (see Fig. 5.1) are similar to those in Ref. [6] except we patterned a tungsten film on only one side and without the central hole. We find that when such a bull's eye is heated an amazingly directional monochromatic beam can be emitted in the normal

direction. Thus, a simple thermal process can provide a laser-like source of infrared radiation.

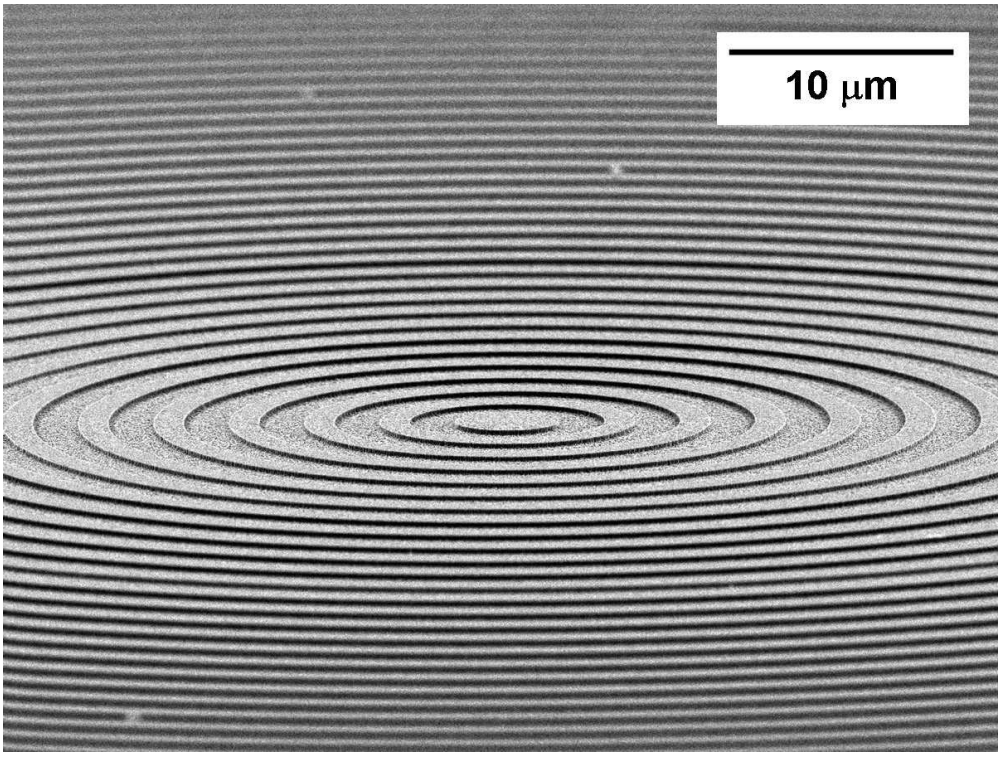

Figure 5.1: Electron micrograph of a bull's eye pattern on a tungsten film. It contains 300 circular, concentric grooves that are 170 nm deep, 2.19 μm wide, and with a period of 3.50 μm.

Prior work has considered the ability of patterned surfaces [9, 10, 11, 12, 13] or periodically structured solids [14, 15, 16, 17, 18, 19] to modify the emissivity of a material. Most efforts have aimed to obtain emission features that are sharper than the broad black-body-like spectrum expected for unstructured solids. Indeed, narrow spectra have been reported, particularly for simple surface gratings. For example, one-dimensionally (1D) periodic grooves in a metal film can lead to a sharp emission peak. However, its

wavelength depends on the propagation direction of the emission [11]. Thus, the angle-integrated spectrum is neither narrow nor directional. Highly directional monochromatic beams of thermal emission have not been obtained.

5.2 Origin of Nearly Monochromatic Beaming of Thermal Emission

To consider if a bull's eye can provide such a beam, we begin with a theoretical examination. This can be helpful since, as seen in simple gratings [9, 10], the exact structure of the grooves can strongly influence the emission properties. However, because the bull's eye lacks translational symmetry, standard techniques for electromagnetic simulations of periodic structures are inefficient. Thus, such techniques have only been applied to bull's eyes with a small number of circular grooves [20]. For a more thorough study, we assumed the opposite limit — that our bull's eyes are very large, much larger than the SPP coherence length. In this case, we can neglect contributions from the boundary and center of the bull's eye and approximate the structure with a series of linear gratings oriented around the center. The optical properties can then be determined by averaging the response of linear gratings evenly distributed in all directions in the plane. Specifically, we will average the absorptivity, as it is equivalent to emissivity according to Kirchhoff's law.

We can visualize this with Fig. 5.2, which plots the in-plane wavevectors for which absorption will occur for a 1D tungsten grating [21]. Contour plots of the actual absorptivity are shown in Fig. 5.3. The grating is ruled along y and periodic in x with period $a = 3.5\,\mu$m. Absorption will occur when the incident light satisfies the momentum matching condition for coupling to SPPs [22], that is, when the incident light gains just enough parallel momentum from the grating to propagate parallel to the surface. The curves in Fig. 5.2 show when this condition is satisfied. When shifted by an integer multiple of the reciprocal lattice vector of the grating ($2\pi/a$), these curves lie on the

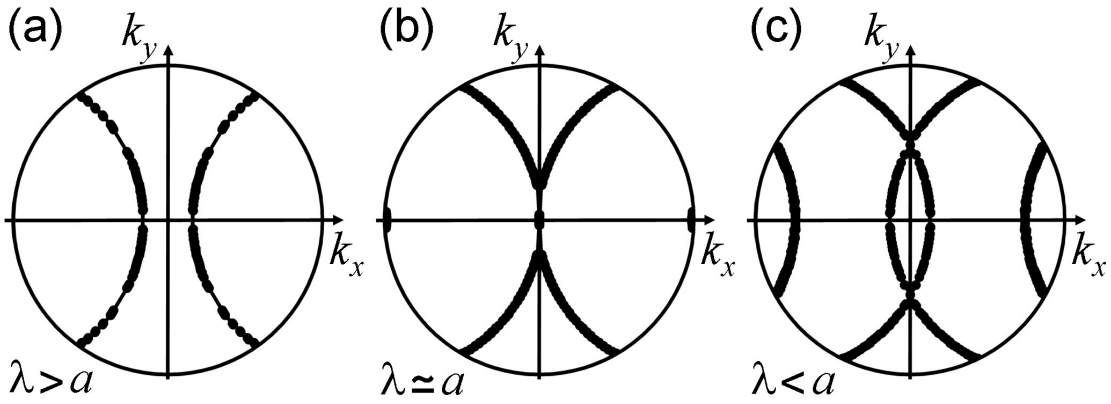

Figure 5.2: Calculated in-plane wavevectors (dots) for which unpolarized light will be absorbed at λ of (a) 4.078, (b) 3.502, and (c) 3.069 μm for a tungsten 1D grating ruled along y and periodic in x with $a = 3.5\,\mu$m. The circular plot boundary is $k_{\|} = 2\pi/\lambda$. The cross-section of the grooves is rectangular with a depth of 165 nm and a width of 2.625 μm.

circular boundary of the plot. The boundary represents light with $k_{\|} = 2\pi/\lambda$, where $k_{\|}$ is the wavevector parallel to the xy-plane and λ is the optical wavelength. Three cases are shown in Fig. 5.2: (a) $\lambda > a$, (b) $\lambda \simeq a$, and (c) $\lambda < a$. When λ is very close to a, the plot has two dots at $k_x = \pm 2\pi/a$ and two arcs meeting at the origin.

Using absorptivity vs. wavevector plots for 1D gratings, we can determine the absorptivity due to SPPs for large bull's eyes by averaging around a circle with radius $k_{\|} = (k_x^2 + k_y^2)^{1/2}$. Since $k_{\|}$ can be converted to an angle θ from the surface normal through $k_{\|} = 2\pi \sin\theta/\lambda$, we can extract the angular dependence of the absorptivity by considering a series of $k_{\|}$ circles that increase in radius from zero to the plot boundary. From Fig. 5.2, we see that for $\lambda > a$ and $\lambda < a$ the absorptivity will be negligible when the $k_{\|}$ circle is very near the origin as no absorption curves exist there. As $k_{\|}$ increases, the circle will eventually intersect the curves that lie closest to the origin. This will lead to a feature in the absorptivity at a given θ. However, because we average around the entire circumference of the $k_{\|}$ circle, such a feature will be weak. Further, it should become weaker as the $k_{\|}$ circle increases in radius. Similarly, because the first intersection between the circle and the absorption curve moves away from the origin

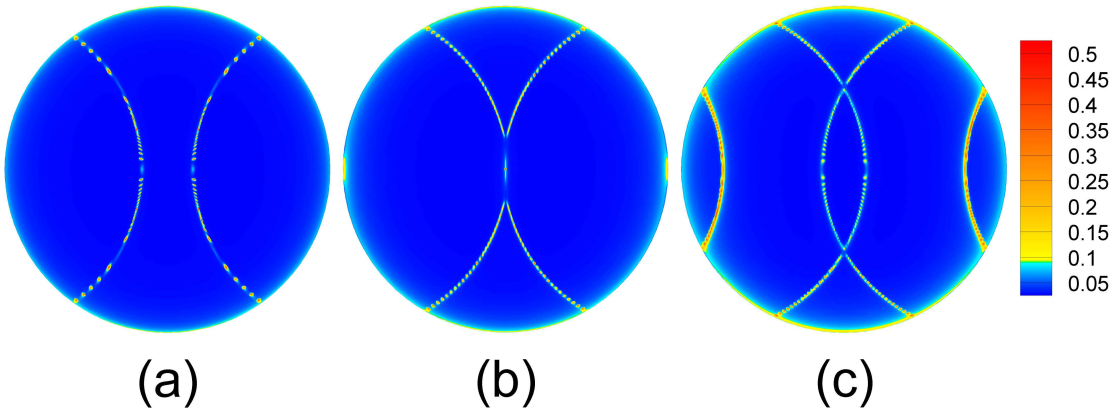

Figure 5.3: A contour plot of the absorptivity versus in-plane wavevector for unpolarized incident light and for the same 1D grating shown in Fig. 5.2. The coordinate system is also the same as in Fig. 5.2.

as λ diverges from a, the contribution to the absorptivity will also decrease away from the $\lambda \simeq a$ resonance condition. For the special case of resonance (Fig. 5.2b), the two absorption curves cross at the origin. Thus, averaging over a very small $k_{\|}$ circle near the origin will lead to a large contribution to the absorptivity. Consequently, on resonance the bull's eye should exhibit an intense peak near $\theta = 0$ and will be small otherwise. This qualitative analysis suggests that the absorptivity due to SPPs in the bull's eye will decrease as: (i) θ increases and (ii) λ diverges from a. Moreover, a sharp absorption peak should be observed when the surface is illuminated near normal incidence at $\lambda \simeq a$. Due to Kirchhoff's law, this implies a highly directional monochromatic beam will be emitted in the normal direction when the bull's eye is heated. The maximum intensity of this beam will be approximately half that of a black body at the same temperature because SPPs couple only to p-polarized light. We also note that this beaming behavior arises from the circular structure of the bull's eye and does not occur in linear gratings.

5.3 Numerical Calculation and Experiment for Shallow Grooves

Following this approach, we calculated the expected emissivity for large tungsten bull's eyes with $a = 3.5\,\mu$m. We varied the width and depth of the rectangular-shaped grooves to minimize the spectral width of the emission feature while keeping the emissivity above 0.5. We restricted the groove depth to be less than 250 nm for fabrication reasons. The groove parameters listed in Fig. 5.2 lead to our best results. By averaging over $k_{\|}$ circles we obtained spectra for this structure for various angles, as shown in Fig. 5.4a. As predicted, the calculated emissivity for $\theta \neq 0$ exhibits weak features both above and below $\lambda = a$ that increase in separation with increasing angle. More importantly, for $\theta = 0$ a sharp peak appears for $\lambda \simeq a$ with a spectral width at half maximum of less than 1 nm (Fig. 5.4a inset), which represents a quality factor, $Q = \lambda/\Delta\lambda$, of 5130. Figure 5.4b shows the calculated angular dependence of the emissivity at the peak wavelength $\lambda = 3.502\,\mu$m. The angular width at half maximum is only 0.021°, which is about seven times narrower than that reported for a 1D tungsten grating emitting near $4\,\mu$m [12]. Previously, it was noted that this 1D result is already comparable to the angular width of a typical He-Ne laser of 0.12° at $\lambda = 3.39\,\mu$m [12]. However, such a comparison is actually better justified for the bull's eye. Its emission should exhibit a single highly directional beam instead of the more complex emission pattern from the 1D grating.

The small angular width of our beam implies a long spatial coherence on a source plane [23]. This coherence is caused by the SPPs and their coupling to the propagating beam [11, 12]. The coherence length L_{SPP} of the SPPs for our structure is estimated to be $\lambda/\Delta\theta = 2692\lambda$ which would be the largest SPP coherence length reported for this wavelength region. Indeed, this is longer than L_{SPP} for a flat surface, $1/\mathrm{Im}(k_{\|}) = 312\lambda$. Recently, it was discussed how L_{SPP} of a grating can be larger than that for a flat surface [24, 25, 26]. We also caution that other radiating modes unrelated to the SPPs can contribute and decrease the coherence length of the overall field.

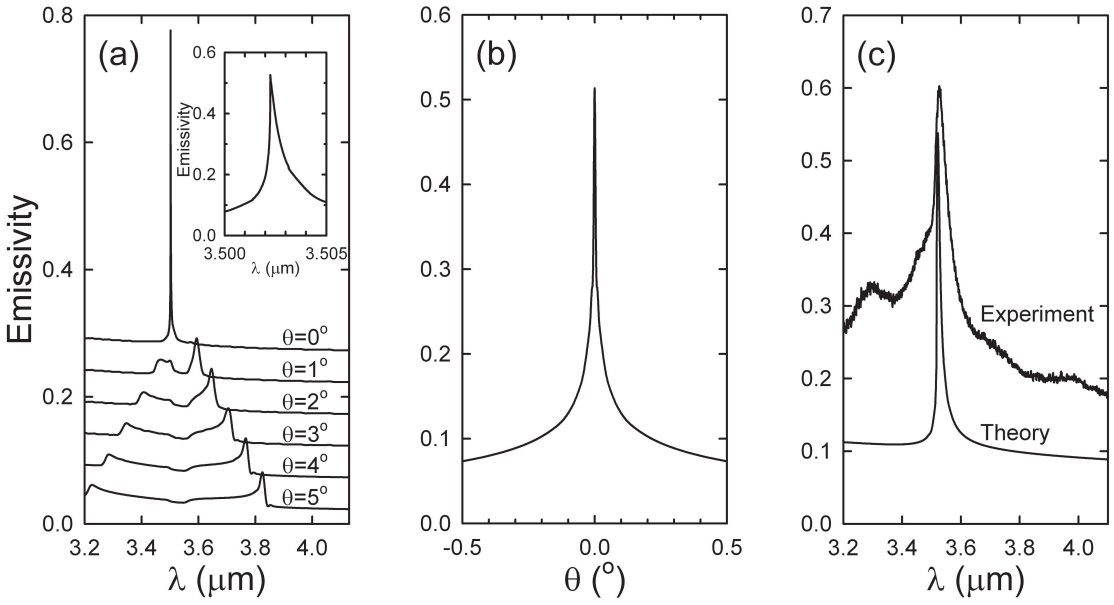

Figure 5.4: Calculated (a) emissivity spectra at various angles θ from the surface normal and (b) angular dependence of emissivity at the peak maximum $\lambda = 3.502\,\mu m$ for a tungsten bull's eye structure with groove parameters as in Fig. 5.2. The dielectric function for 25 °C was used. The spectrum at $\theta = 0$ is enlarged in the inset of (a). (c) Measured and calculated emissivity spectrum for the bull's eye in Fig. 5.1. The light collection angle in experiment was 0.1° around the surface normal and the sample temperature was 900 °C. Thermal expansion and the temperature dependence of the dielectric function were included in the calculation. A carbon black pellet was used as a black body for calibration.

To test if a directional beam is observed in experiment, we fabricated a bull's eye with a period of 3.50 μm. We first sputtered a 500 nm thick tungsten film onto a clean Si wafer. A bull's eye pattern was formed in photoresist via photolithography and then transferred into the tungsten with reactive ion etching with SF_6. To fabricate the bull's eye structures, the following procedure was used. Shipley 1805 positive tone resist was spin coated at 3500 rpm on a clean silicon substrate that had been sputtered with a 500 nm thick film of tungsten. Using standard photolithographic techniques, a bull's eye pattern was exposed through a Karl Suss Mask aligner using a chrome on glass mask. The exposed wafers were then developed in Microposit 351 developer (Rohm

and Haas) for 30 seconds, rinsed with deionized water, and dried with nitrogen. The pattern was transferred into the tungsten by reactive ion etching with SF_6 and argon at 40 mtorr and 50 watts, using the photoresist as a protective layer. After transferring the pattern into the tungsten, the photoresist was removed by rinsing thoroughly in acetone, followed by immersion in Shipley 165 stripper at 65 °C for more than two hours. The wafers were then rinsed with water and acetone, and dried in nitrogen. The obtained structure (Fig. 5.1) had 300 grooves 170 nm deep and 2.19 μm wide, which differs slightly from the target parameters listed in Fig. 5.2. This structure was heated under vacuum on a stage (Linkam TS 1500) to 900 °C and the emission was detected with a cooled InSb photodiode attached to a Fourier transform infrared spectrometer. Two apertures defined a collection angle of 0.1°. As shown in Fig. 5.4c, a peak at 3.526 μm was observed. This feature appeared only when the apparatus was extremely well aligned to collect at $\theta = 0$. Thus, experiments confirmed a highly directional beam of emission in the normal direction.

Figure 5.4c also shows a calculation for the experimental structure, in which we included thermal expansion [27] and the temperature dependence of the dielectric function [28]. At 25 °C the predicted peak is at 3.507 μm, but at 900 °C shifts to 3.522 μm, in excellent agreement with experiment. This shift is due to thermal expansion rather than the dielectric function. Regarding the spectral width, we would expect the emission to be broader than the predictions in Fig. 5.4a due to differences from the optimized structure that can strongly effect the emission behavior. However, the experimental peak with $Q = 70$ is broader than even the calculation for the same structure (Fig. 5.4c). The origin of this difference is not known, but surface roughness and other structural disorder may play a role. For the experimental structure, the predicted angular width at 900 °C is 1.4°. From this, we can estimate L_{SPP} to be $41\lambda = 144\,\mu m$. The actual coherence length should be even smaller because of structural imperfections. Thus, because the diameter of our experimental bull's eye (2.1 mm) is much larger, this justifies our large bull's eye assumption.

For the optimized structure, Fig. 5.5 shows the expected peak wavelength, quality factor Q, and angular width versus temperature. The peak wavelength λ_{max} increases with temperature due to thermal expansion. The total shift is about 40 nm between 25 and 2000 °C, which indicates that fine temperature tuning of λ_{max} should be possible. The quality factor of the beam decreases with increasing temperature due to changes in the dielectric function, which shortens the SPP life time. However, even at 2000 °C, Q should still be ~ 1000.

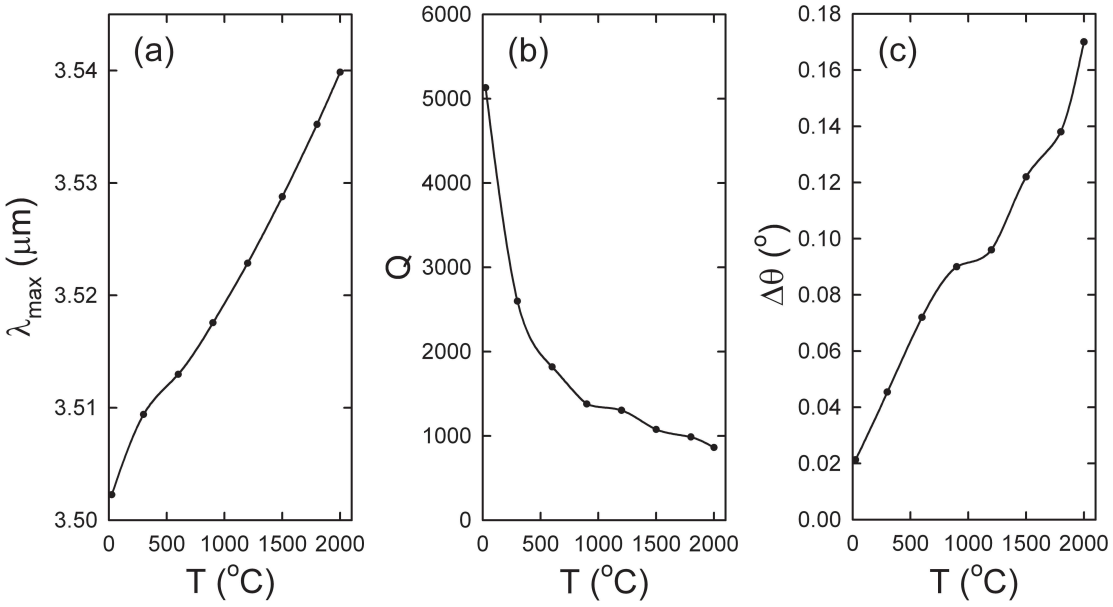

Figure 5.5: Calculated temperature dependence of (a) the peak wavelength λ_{max}, (b) the quality factor Q, and (c) the angular width $\Delta\theta$ for the tungsten bull's eye structure with groove parameters as in Fig. 5.2. (a) and (b) are for the surface normal direction and (c) is at λ_{max}.

5.4 Deep Grooves and Optical Beams

For the grating discussed in the previous section, we observe several points that are different from conventional lasers. First, while lasers are typically linearly polarized, the emission from the bull's eyes is unpolarized as will be discussed in section 5.5.

Second, pulsed operation is difficult for thermal emission. Third, the peak intensity is weaker for thermal sources due to the black-body limit. This is due to the condition of thermal equilibrium in the grating. To break this limit, we would need to use a non-equilibrium emission such as luminescence as discussed in Chapter 1. Fourth, emission from wavelengths other than the peak wavelength are not totally absent. For example, the background emission in Fig. 5.4 is almost the same as for a flat film. This means the background wavelengths are not as efficiently recycled into the peak as in a conventional lasers. Fifth, in Fig. 5.4a, we observe small peaks that appear at off-normal directions. These have been weakened by averaging over a circle in wavevector space, as explained in section 5.2, but are not completely removed. Sixth, the possible range of wavelengths for thermal emission has not been demonstrated. For long wavelengths such as far-infrared, thermal emission intensity will always be very low. However, the possibility of operation in the near-infrared and visible range, where the intensity of thermal emission can be higher, needs to be explored. In this section, we wish to deal with the last two points.

Recently, it was discussed that the coherence length of SPPs can be larger than the SPPs on a flat surface [24, 25, 26]. A way to achieve this is to couple the resonant cavities in gratings to each other [24, 25]. For the cavity mode, the depth of the groove is about $\sim \lambda/2$ which is much deeper than the groove in Fig. 5.2. At the cavity resonance frequency, the cavities are coherently coupled by the delocalized SPPs which can have a coherence length larger than on a flat surface. This leads to a narrow angular width of emission in the plane (xz) perpendicular to the 1D grating (y). However, at other frequencies, the cavity modes are not excited. Consequently, the thermal emission of a narrow frequency band is emitted in a narrow angle in the xz-plane.

The absorptivity on the in-plane wavevector space will be different from Fig. 5.3. In particular, the intensities along the arcs in Fig. 5.3 will be smaller for the coupled cavities. In addition, an appreciable absorptivity may be possible at wavevectors not along the arcs. However, due to the cavity mode, the absorptivity at $\lambda \simeq a$ will be

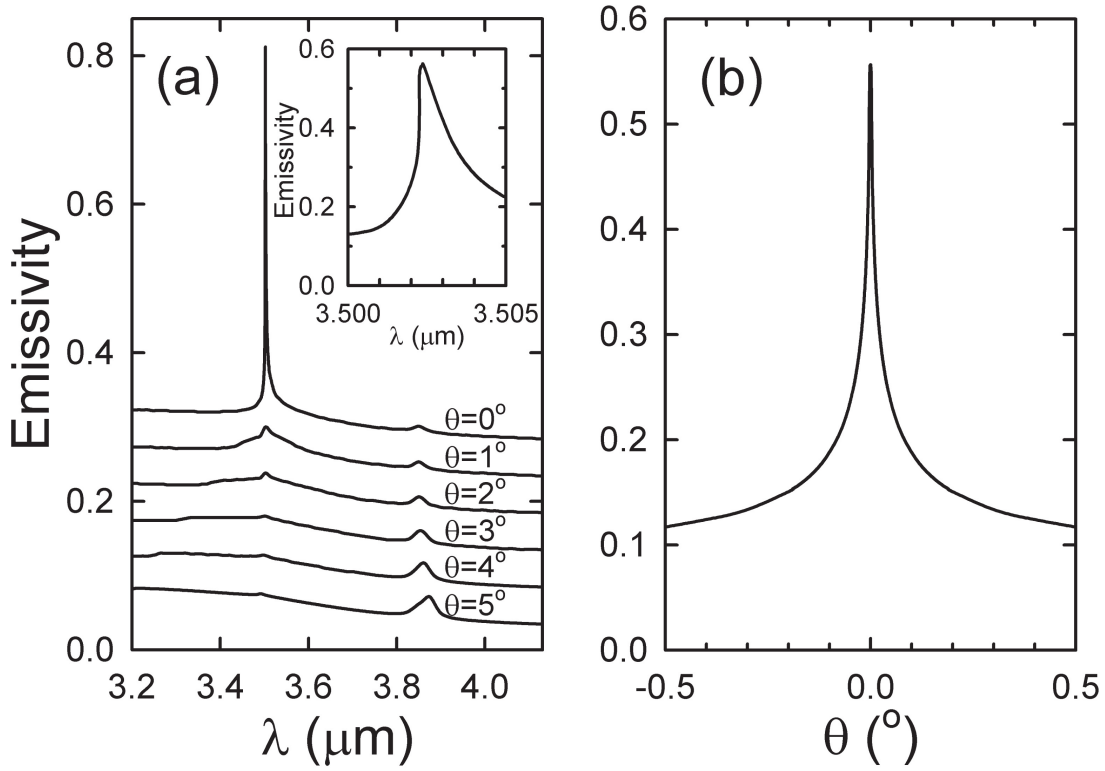

Figure 5.6: Calculated (a) emissivity spectra at various angles θ from the surface normal and (b) angular dependence of emissivity at the peak maximum $\lambda = 3.502\,\mu m$ for a tungsten bull's eye structure supporting a coupled cavity resonance. The cross-section of the groove is rectangular and the period, depth, and width of the groove are 3.5 μm, 1.825 μm, and 1.925 μm, respectively.

strong. Therefore, when the absorptivity is averaged around the $k_{\|}$ circles, the behavior will be different from the shallow gratings discussed in the previous section. Figure 5.6 shows the calculated emissivity for large tungsten bull's eyes with the period, depth, and width of the groove being 3.5 μm, 1.825 μm, and 1.925 μm, respectively. The groove parameters were optimized as before to minimize the spectral width while keeping the emissivity above 0.5. An optical behavior similar to Fig. 5.4 is obtained. In this case, the peak at $\lambda = 3.502$ μm for $\theta = 0$ is slightly broader ($Q = 2270$) as well as the angular width at half maximum ($\Delta\theta = 0.036°$). However, the small peaks observed at off-normal

directions in Fig. 5.4 have disappeared. Even though a small peak at $\lambda = 3.85$ μm is growing as the angle increases, the background emission is in general smoother than for the deep grooves. This is the consequence of using the cavity mode that couples to the normal direction. As the groove becomes deep, the interaction between the light and the groove can increase as the surface area increases. This can lead to a higher absorptivity and emissivity. Figure 5.7 compares the angular dependence of the emissivity for the deep and the shallow grooves. Even though both show a highly narrow peak in the normal direction, the background emissivity is about twice higher for the deep grooves. This is not specifically due to the p-polarization. For the shallow groove, the emissivity far from the the surface normal is very close to a flat tungsten film because of the similar surface area.

The emissivity peak can be shifted to shorter wavelengths if the grating period of a bull's eye structure is reduced. However, tungsten bull's eyes absorb light significantly in the near-infrared or shorter wavelengths. This will shorten the SPP propagation length resulting in a broader spectral and angular peak. For an emissivity peak at $\lambda = 1.5$ μm, we may consider tantalum structures because absorption at this wavelength is not significant. Also its melting point (3007 °C) is not far from tungsten (3414 °C). We optimized for tantalum the groove parameters as in section 5.3. Figure 5.8 shows the spectral and angular dependence of the emissivity of the large tantalum bull's eye. A sharp peak is obtained ($Q = 1029$) at $\lambda = 1.502$ μm in the normal direction and the angular width is narrow ($\Delta\theta = 0.12^\circ$) at this wavelength. The spectral and angular peak width is about 5-6 times larger than Fig. 5.4a and b. This is partly because the intrinsic absorption of tantalum at this wavelength is stronger than tungsten at $\lambda = 3.502$ μm. For example, the SPP propagation length of a flat tantalum surface is $1/\mathrm{Im}(k_{\|}) = 101\lambda$, while that of tungsten is 312λ.

To have a laser-like beam in the visible wavelengths, noble metals are advantageous in terms of optical properties due to their small absorption. Silver is particularly useful in the visible range. For a period of 550 nm, we optimized the grating parameters of a

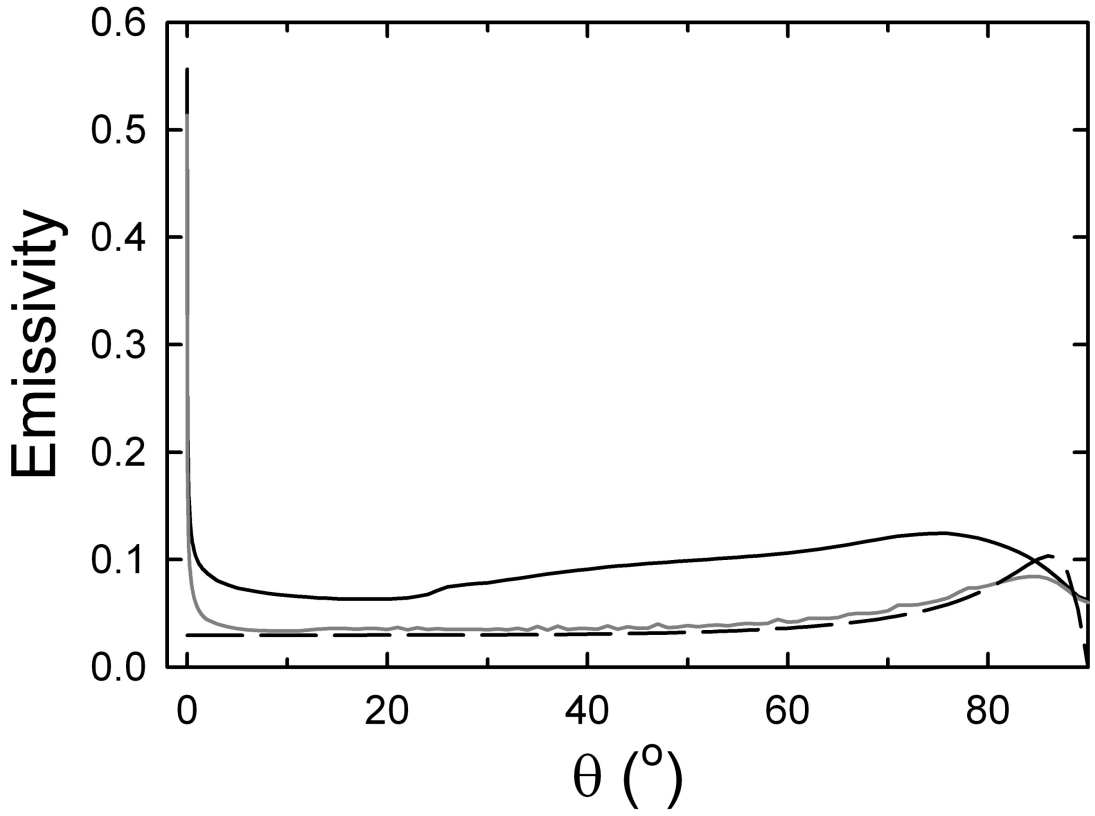

Figure 5.7: Calculated angular dependence of emissivity at the peak maximum $\lambda = 3.502\,\mu m$ for tungsten bull's eye structures with groove parameters as in Fig. 5.6 (solid black line) and Fig. 5.2 (gray black line). The dashed black line represents emissivity for a flat tungsten surface.

silver grating to have a narrow spectral width and the emissivity above 0.5 for coupled cavity modes. The calculated emissivity for the large silver bull's eye is shown in Fig. 5.9. Even though a peak narrow both in spectrum and angle appears, Fig. 5.9 shows $Q = 70$ and $\Delta\theta = 1.7^\circ$ which are much broader in comparison to the previous tungsten and tantalum structures. The SPP propagation length is estimated to be $\lambda/\Delta\theta = 34\lambda$ which is comparable to that of a flat film of $1/\mathrm{Im}(k_{\|}) = 45\lambda$ at $\lambda = 557$ nm. This shows that the coupled cavity mode does not necessarily lead to a coherence length much larger than a flat surface. Moreover, for off-normal directions, the spectra show a

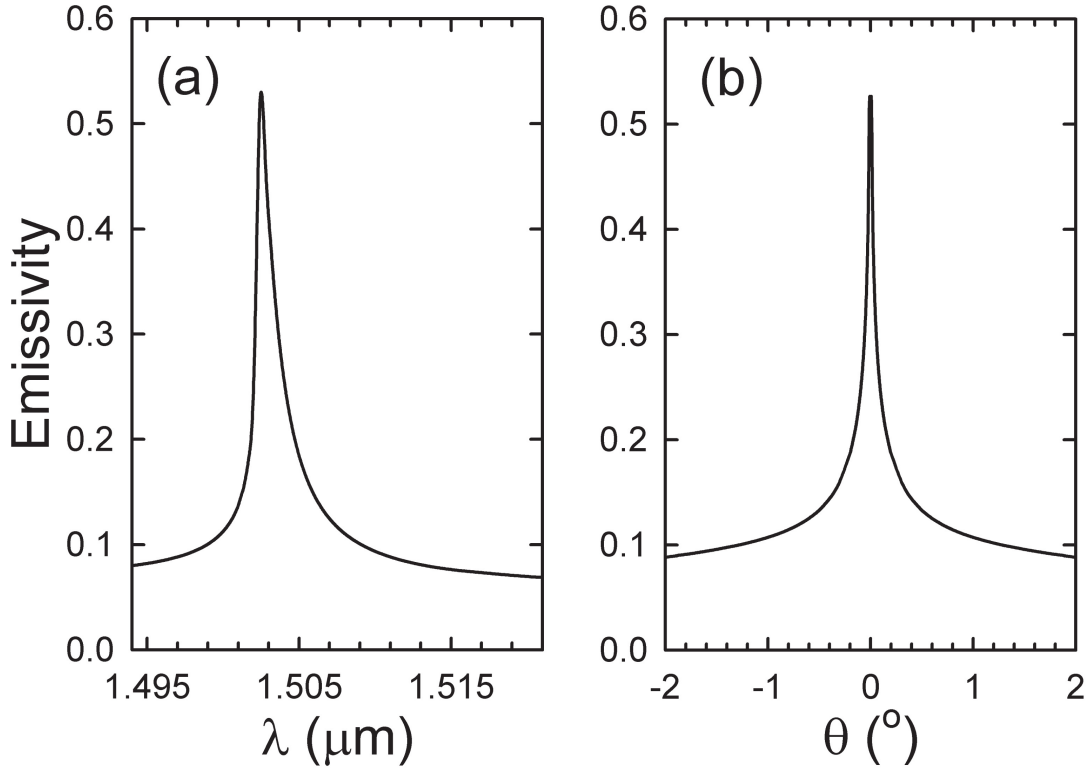

Figure 5.8: Calculated (a) emissivity spectra in the surface normal direction and (b) angular dependence of the emissivity at the peak maximum $\lambda = 1.502\,\mu m$ for a tantalum bull's eye structure. The cross-section of the groove is rectangular and the period, depth, and width of the groove are 1.5 μm, 165 nm, and 1.275 μm, respectively.

small peak that shifts to the blue as the angle increases. This feature is almost absent in Fig. 5.6 for the tungsten structure. Therefore the realization of a quasimonochromatic thermal beam at a visible wavelength is challenging. It should also be noted that the melting point of silver is only 962 °C which limits the intensity of the beam.

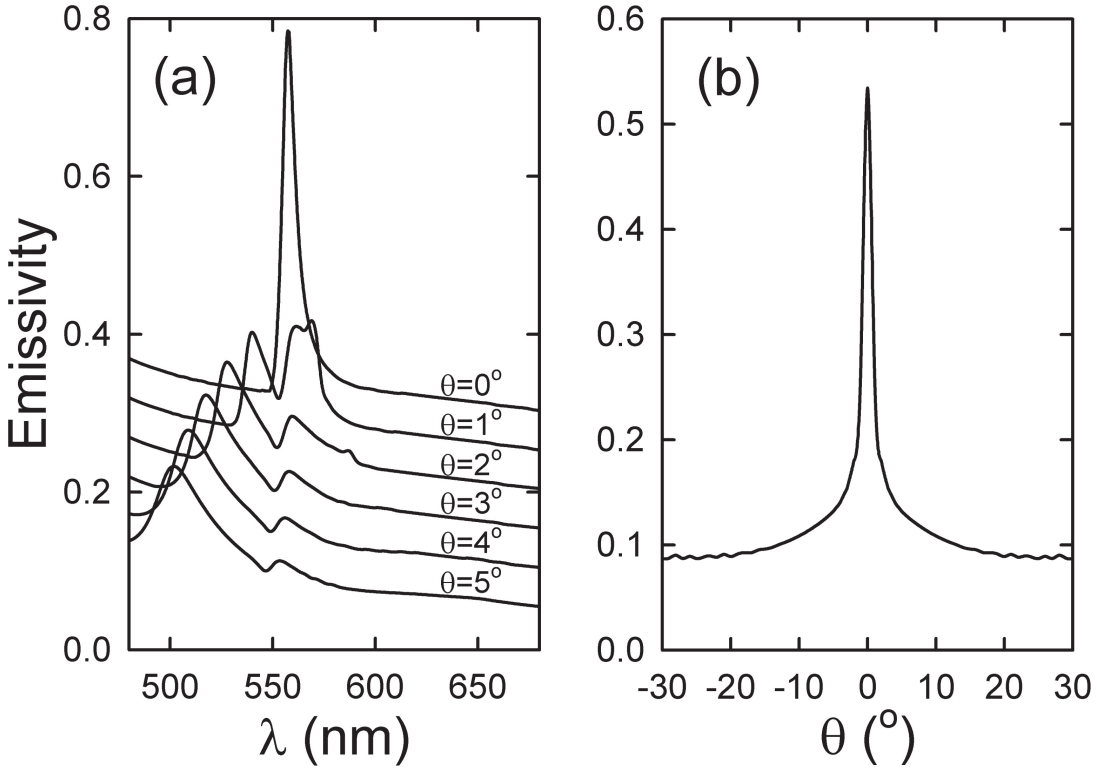

Figure 5.9: Calculated (a) emissivity spectra at various angles θ from the surface normal and (b) angular dependence of the emissivity at the peak maximum ($\lambda = 557$ nm) for a silver bull's eye structure supporting a coupled cavity resonance. The cross-section of the groove is rectangular and the period, depth, and width of the groove are 550 nm, 280 nm, and 358 nm, respectively.

5.5 Discussion

The underlying physics here can be compared with that of several related systems. First, while our structures appear similar to bull's eyes studied for enhanced transmission [6], in that case the central hole plays a key role in the physics. In contrast, the central region could be completely neglected in our model for thermal beaming. Indeed, effects that arise in finite size bull's eyes due to the center or boundary should be an interesting area of future study. Second, our bull's eyes appear similar to distributed feedback lasers made from concentric circular gratings. These devices also generate

monochromatic beams [29]. However, they combine a gain medium with conventional dielectric cavity modes instead of a thermal process with SPPs. Moreover, the laser output is an azimuthally polarized Bessel beam [30], which has a finite propagation distance [30, 31]. In contrast, our beams are not limited in their propagation length. Also, heated bull's eyes produce unpolarized light due to the random nature of thermal currents. Specifically, thermal fluctuations at two different points are completely uncorrelated as described by the fluctuation-dissipation theorem [32]. The Fourier components of the currents oscillating in different directions are also uncorrelated. Thus, SPPs propagating in different directions on the bull's eye structure are uncorrelated, leading to unpolarized light emission.

5.6 Conclusion

We have shown that thermal excitation of SPPs on bull's eyes can lead to spectrally narrow beams of infrared light with small angular divergence. These beams arise due to the interaction of SPPs with the circular symmetry of the structure. Although the emission intensity is less than conventional lasers due to the limitation imposed by Planck's radiation law, such beams can still provide useful sources as they have other laser-like qualities. Tungsten structures should allow very high quality factors ($Q \sim 1000$) and angular widths less than 0.2° when heated up to 2000 °C. This effect is not limited to tungsten, but occurs in other metals, such as Ta or Ag, which can decrease the emission wavelength. More broadly, by understanding the physics of heated plasmonic structures, a variety of interesting optical phenomena should be possible.

References

[1] H. Raether, *Surface plasmons* (Springer-Verlag, Berlin, 1988).

[2] A. Polman, "Plasmonics applied," Science **322**, 868-869 (2008).

[3] W. L. Barnes, A. Dereux, and T. W. Ebbesen, "Surface plasmon subwavelength optics," Nature **424**, 824-830 (2003).

[4] E. Ozbay, "Plasmonics: Merging photonics and electronics at nanoscale dimensions," Science **311**, 189-193 (2006).

[5] T. W. Ebbesen, H. J. Lezec, H. F. Ghaemi, T. Thio, and P. A. Wolff, "Extraordinary optical transmission through sub-wavelength hole arrays," Nature **391**, 667-669 (1998).

[6] H. J. Lezec, A. Degiron, E. Devaux, R. A. Linke, L. Martin-Moreno, F. J. García-Vidal, and T. W. Ebbesen, "Beaming light from a subwavelength aperture," Science **297**, 820-822 (2002).

[7] L. Martín-Moreno, F. J. García-Vidal, H. J. Lezec, A. Degiron, and T. W. Ebbesen, "Theory of highly directional emission from a single subwavelength aperture surrounded by surface corrugations," Phys. Rev. Lett. **90**, 167401 (2003).

[8] Y. De Wilde, F. Formanek, R. Carminati, B. Gralak, P. A. Lemoine, K. Joulain, J. P. Mulet, Y. Chen, and J. J. Greffet, "Thermal radiation scanning tunnelling microscopy," Nature **444**, 740-743 (2006).

[9] P. J. Hesketh, J. N. Zemel, and B. Gebhart, "Organ pipe radiant modes of periodic micromachined silicon surfaces," Nature (London) **324**, 549-551 (1986).

[10] A. Heinzel, V. Boerner, A. Gombert, B. Blasi, V. Wittwer, and J. Luther, "Radiation filters and emitters for the NIR based on periodically structured metal surfaces," J. Mod. Opt. **47**, 2399-2419 (2000).

[11] J. J. Greffet, R. Carminati, K. Joulain, J. P. Mulet, S. Mainguy, and Y. Chen, "Coherent emission of light by thermal sources," Nature (London) **416**, 61-64 (2002).

[12] M. Laroche, C. Arnold, F. Marquier, R. Carminati, J. J. Greffet, S. Collin, N. Bardou, and J. L. Pelouard, "Highly directional radiation generated by a tungsten thermal source," Opt. Lett. **30**, 2623-2625 (2005).

[13] Y. T. Chang, Y. H. Ye, D. C. Tzuang, Y. T. Wu, C. H. Yang, C. F. Chan, Y. W. Jiang, and S. C. Lee, "Localized surface plasmons in Al/Si structure and Ag/SiO_2/Ag emitter with different concentric metal rings," Appl. Phys. Lett. **92**, 233109 (2008).

[14] C. M. Cornelius and J. P. Dowling, "Modification of Planck blackbody radiation by photonic band-gap structures," Phys. Rev. A **59**, 4736-4746 (1999).

[15] J. G. Fleming, S.-Y. Lin, I. El-Kady, R. Biswas, and K. M. Ho, "All-metallic three-dimensional photonic crystals with a large infrared bandgap," Nature (London) **417**, 52-55 (2002).

[16] M. U. Pralle, N. Moelders, M. P. McNeal, I. Puscasu, A. C. Greenwald, J. T. Daly, E. A. Johnson, T. George, D. S. Choi, I. El-Kady, and R. Biswas, "Photonic crystal enhanced narrow-band infrared emitters," Appl. Phys. Lett. **81**, 4685-4867 (2002).

[17] I. Celanovic, D. Perreault, and J. Kassakian, "Resonant-cavity enhanced thermal emission," Phys. Rev. B **72**, 075127 (2005).

[18] S. E. Han, A. Stein, and D. J. Norris, "Tailoring self-assembled metallic photonic crystals for modified thermal emission," Phys. Rev. Lett. **99**, 053906 (2007).

[19] X. D. Yu, Y. J. Lee, R. Furstenberg, J. O. White, and P. V. Braun, "Filling fraction dependent properties of inverse opal metallic photonic crystals," Adv. Mater. **19**, 1689-1692 (2007).

[20] H. Caglayan, I. Bulu, and E. Ozbay, "Extraordinary grating-coupled microwave transmission through a subwavelength annular aperture," Opt. Express **13**, 1666-1671 (2005).

[21] We used the transfer matrix formalism with a unit cell discretized by a 80×80 mesh. For 25 °C, we used the dielectric function for tungsten from D. W. Lynch and W. R. Hunter, in *Handbook of optical constants of solids*, edited by E. D. Palik (Academic Press, Orlando, 1985).

[22] F. Marquier, C. Arnold, M. Laroche, J. J. Greffet, and Y. Chen, "Degree of polarization of thermal light emitted by gratings supporting surface waves," Opt. Express **16**, 5305-5313 (2008).

[23] L. Mandel and E. Wolf, *Optical coherence and quantum optics* (Cambridge University Press, 1995).

[24] N. Dahan, A. Niv, G. Biener, Y. Gorodetski, V. Kleiner, and E. Hasman, "Enhanced coherency of thermal emission: Beyond the limitation imposed by delocalized surface waves," Phys. Rev. B **76**, 045427 (2007).

[25] N. Dahan, A. Niv, G. Biener, Y. Gorodetski, V. Kleiner, and E. Hasman, "Extraordinary coherent thermal emission from SiC due to coupled resonant cavities," J. Heat Transfer, **130**, 112401 (2008).

[26] G. Biener, N. Dahan, A. Niv, V. Kleiner, and E. Hasman, "Highly coherent thermal emission obtained by plasmonic bandgap structures," Appl. Phys. Lett. **92**, 081913 (2008).

[27] A. P. Miiler and A. Cezairliyan, "Thermal expansion of tungsten in the range 15003600 K by a transient interferometric technique," Int. J. Thermophys. **11**, 619-628 (1990).

[28] L. N. Aksyutov and A. K. Pavlyukov, "Temperature dependence of the optical constants of tungsten and gold," Zh. Prikl. Spektrosk. **26**, 914-918 (1977).

[29] T. Erdogan and D. G. Hall, "Circularly symmetric distributed feedback semiconductor laser: An analysis," J. Appl. Phys. **68**, 1435-1444 (1990).

[30] R. H. Jordan and D. G. Hall, "Free-space azimuthal paraxial wave equation: the azimuthal Bessel-Gauss beam solution," Opt. Lett. **19**, 427-429 (1994).

[31] J. Durnin, J. J. Miceli, Jr, and J. H. Eberly, "Diffraction-free beams," Phys. Rev. Lett. **58**, 1499-1501 (1987).

[32] S. M. Rytov, Y. A. Kravtsov, and V. I. Tatarskii, *Principles of statistical radiophysics, Vol. 3: Elements of random fields* (Springer-Verlag, Berlin, 1989).

Bibliography

P. C. Sorcar, *Energy saving lighting systems* (Van Nostrand Reinhold, New York, 1982).

E. Yablonovitch, "Inhibited spontaneous emission in solid-state physics and electronics," Phys. Rev. Lett. **58**, 2059-2062 (1987).

J. D. Joannopoulos, *Photonic crystals : Molding the flow of light* (Princeton University Press, Princeton, 2008).

J. -M. Lourtioz, H. Benisty, V. Berger, J. -M Gérard, D. Maystre, and A. Tchelnokov, *Photonic crystals : Towards nanoscale photonic devices* (Springer, Berlin, 2005).

K. Sakoda, *Optical properties of photonic crystals* (Springer, Berlin, 2001).

K. Busch, *Photonic crystals : Advances in design, fabrication, and characterization* (Wiley-VCH, Weinheim, 2004).

C. M. Cornelius and J. P. Dowling, "Modification of planck blackbody radiation by photonic band-gap structures," Phys. Rev. A **59**, 4736-4746 (1999).

S. Y. Lin, J. G. Fleming, E. Chow, J. Bur, K. K. Choi, and A. Goldberg, "Enhancement and suppression of thermal emission by a three-dimensional photonic crystal," Phys. Rev. B **62**, R2243-R2246 (2000).

S. Y. Lin, J. Moreno, and J. G. Fleming, "Three-dimensional photonic-crystal emitter for thermal photovoltaic power generation," Appl. Phys. Lett. **83**, 380-382

(2003).

S. Y. Lin, J. G. Fleming, and I. El-Kady, "Experimental observation of photonic crystal emission near a photonic band edge," Appl. Phys. Lett. **83**, 593-595 (2003).

S. Y. Lin, J. G. Fleming, and I. El-Kady, "Highly efficient light emission at $\lambda = 1.5$ μm by a three-dimensional tungsten photonic crystal," Opt. Lett. **28**, 1683-1685 (2003).

S. John and R. Wang, "Metallic photonic-band-gap filament architectures for optimized incandescent lighting," Phys. Rev. A **78**, 043809 (2008).

P. Nagpal, S. E. Han, A. Stein, and D. J. Norris, "Efficient low-temperature thermophotovoltaic emitters from metallic photonic crystals," Nano Lett. **8**, 3238-3243 (2008).

M. Laroche, R. Carminati, and J.-J. Greffet, "Coherent thermal antenna using a photonic crystal slab," Phys. Rev. Lett. **96**, 123903 (2006).

C. Kittel, *Introduction to solid state physics* (Wiley, New York, 1966).

N. W. Ashcroft, *Solid state physics* (Brooks Cole, 1976).

Z.-Y. Li, L.-L. Lin, and Z.-Q. Zhang, "Spontaneous emission from photonic crystals: Full vectorial calculations," Phys. Rev. Lett. **84**, 4341-4344 (2000).

K. Busch and S. John, "Photonic band gap formation in certain self-organizing systems," Phys. Rev. E **58**, 3896-3908 (1998).

L. D. Landau and E. M. Lifshitz, *Statistical physics*, 3rd ed. Part 1 (Reed Educational and Professional Publishing, Oxford, 1980).

F. Reif, *Fundamentals of statistical and thermal physics* (McGraw-Hill, New York, 1965).

M. A. Ordal, R. J. Bell, Jr R. W. Alexander, L. L. Long, and M. R. Querry, "Optical properties of fourteen metals in the infrared and far infrared: Al, Co, Cu, Au, Fe, Pb, Mo, Ni, Pd, Pt, Ag, Ti, V, and W," Appl. Opt. **24**, 4493-4499 (1985).

V. Kuzmiak and A. A. Maradudin, "Photonic band structures of one- and two-dimensional periodic systems with metallic components in the presence of dissipation" Phys. Rev. B **55**, 7427-7444 (1997).

A. A. Krokhin and P. Halevi, "Influence of weak dissipation on the photonic band structure of periodic composites," Phys. Rev. B **53**, 1205-1214 (1996).

J. B. Pendry, A. J. Holden, W. J. Stewart, and I. Youngs, "Extremely low frequency plasmons in metallic mesostructures," Phys. Rev. Lett. **76**, 4773-4776 (1996).

S. A. Mikhailov, "Comment on 'Extremely low frequency plasmons in metallic mesostructures,' " Phys. Rev. Lett. **78**, 4135 (1997).

J. B. Pendry, A. J. Holden, W. J. Stewart, and I. Youngs, "Pendry *et al.* Reply:" Phys. Rev. Lett. **78**, 4136 (1997).

R. M. Walser, A. P. Valanju, and P. M. Valanju, "Comment on 'Extremely low frequency plasmons in metallic mesostructures,' " Phys. Rev. Lett. **87**, 119701 (2001).

J. B. Pendry, A. J. Holden, D. J. Robbins, and W. J. Stewart, "Low frequency plasmons in thin-wire structures," J. Phys.: Condens. Matter **10**, 4785-4809 (1998).

A. L. Pokrovsky, "Analytical and numerical studies of wire-mesh metallic photonic crystals," Phys. Rev. B **69**, 195108 (2004).

E. Özbay, B. Temelkuran, M. Sigalas, G. Tuttle, C. M. Soukoulis, and K. M. Ho, "Defect structures in metallic photonic crystals," Appl. Phys. Lett. **69**, 3797-3799 (1996).

A. Moroz, "Three-dimensional complete photonic-band-gap structures in the visible," Phys. Rev. Lett. **83**, 5274-5277 (1999).

J. G. Fleming, S. Y. Lin, I. El-Kady, R. Biswas, and K. M. Ho, "All-metallic three-dimensional photonic crystals with a large infrared bandgap," Nature **417**, 52-55 (2002).

Z.-Y. Li, I. El-Kady, K.-M. Ho, S. Y. Lin, and J. G. Fleming, "Photonic band gap effect in layer-by-layer metallic photonic crystals," J. Appl. Phys. **93**, 38-42 (2003).

Surface polaritons: Electromagnetic waves at surfaces and interfaces edited by V. M. Agranovich and D. L. Mills (North-Holland, Amsterdam, 1982).

C. F. Bohren and D. R. Huffman, *Absorption and scattering of light by small particles* (Wiley, New York, 1998).

H. Raether, *Surface plasmons on smooth and rough surfaces and on gratings* (Springer-Verlag, Berlin, 1988).

W. L. Barnes, A. Dereux, and T. W. Ebbesen, "Surface plasmon subwavelength optics," Nature **424**, 824-830 (2003).

C. Kittel, *Thermal physics* (W. H. Freeman, San Francisco, 1980).

S. M. Rytov, Yu. A. Kravtsov, and V. I. Tatarskii, *Principles of statistical radiophysics vol. 3: Elements of random fields* (Springer-Verlag, Berlin, 1989).

P. Pringsheim, *Luminescence of liquids and solids and its practical applications* (Interscience publishers, New York, 1943).

H. P. Baltes, "On the validity of Kirchhoff's law of heat radiation for a body in a nonequilibriumm environment," Prog. Opt. **13**, 1-25 (1976).

A. Kittel, W. Müller-Hirsch, J. Parisi, S.-A. Biehs, D. Reddig, and M. Holthaus, "Near-field heat transfer in a scanning thermal microscope," Phys. Rev. Lett. **95**, 224301 (2005).

L. Mandel and E. Wolf, *Optical coherence and quantum optics* (Cambridge University Press, Cambridge, 1995).

M. Born and E. Wolf, *Principles of optics : Electromagnetic theory of propagation, interference and diffraction of light* (Pergamon Press, Oxford, 1965).

Y. De Wilde, F. Formanek, R. Carminati, B. Gralak, P. A. Lemoine, K. Joulain, J. P. Mulet, Y. Chen, and J. J. Greffet, "Thermal radiation scanning tunnelling microscopy," Nature **444**, 740-743 (2006).

S. E. Han, A. Stein, and D. J. Norris, "Tailoring self-assembled metallic photonic crystals for modified thermal emission," Phys. Rev. Lett. **99**, 053906 (2007).

J. D. Joannopoulos, P. R. Villeneuve, and S. Fan, "Photonic crystals: Putting a new twist on light," Nature **386**, 143-149 (1997).

T. Trupke, P. Wurfel, and M. A. Green, "Comment on 'Three-dimensional photonic-crystal emitter for thermal photovoltaic power generation' [Appl. Phys. Lett. 83, 380 (2003)]," Appl. Phys. Lett. **84**, 1997-1998 (2004).

S.-Y. Lin, J. Moreno, and J. G. Fleming, "Response to 'Comment on 'Three-dimensional photonic-crystal emitter for thermal photovoltaic power generation' '[Appl. Phys. Lett. **84**, 1997 (2004)]," Appl. Phys. Lett. **84**, 1999 (2004).

I. El-Kady, W. W. Chow, and J. G. Fleming, "Emission from an active photonic crystal," Phys. Rev. B **72**, 195110 (2005).

W. W. Chow, "Theory of emission from an active photonic lattice," Phys. Rev. A **73**, 013821 (2006).

C. Luo, A. Narayanaswamy, G. Chen, and J. D. Joannopoulos, "Thermal radiation from photonic crystals: A direct calculation," Phys. Rev. Lett. **93**, 213905 (2004).

J. G. Fleming, "Addendum: 'Three-dimensional photonic-crystal emitter for thermal photovoltaic power generation' [Appl. Phys. Lett. 83, 380 (2003)]," Appl. Phys. Lett. **86**, 249902 (2005).

C. H. Seager, M. B. Sinclair, and J. G. Fleming, "Accurate measurements of thermal radiation from a tungsten photonic lattice," Appl. Phys. Lett. **86**, 244105 (2005).

C. Henkel, K. Joulain, R. Carminati, and J.-J. Greffet, "Spatial coherence of thermal near fields," Opt. Commun. **186**, 57-67 (2000).

C. T. Tai, *Dyadic green functions in electromagnetic theory*, 2nd ed. (IEEE Press, New York, 1994), Section 4-5.

L. D. Landau and E. M. Lifshitz, *Electrodynamics of continuous media*, 2nd ed. (Pergamon, Oxford, 1984).

J. E. Sipe, "New Green-function formalism for surface optics," J. Opt. Soc. Am. B **4**, 481-489 (1987).

S. E. Han and D. J. Norris, "Control of thermal emission by selective heating of periodic structures," Phys. Rev. Lett. (submitted).

C. L. Mehta and E. Wolf, "Coherence properties of blackbody radiation. III. Cross-spectral tensors," Phys. Rev. **161**, 1328-1334 (1967).

J. B. Pendry and A. MacKinnon, "Calculation of photon dispersion relations," Phys. Rev. Lett. **69**, 2772-2775 (1992).

J.-J. Greffet, R. Carminati, K. Joulain, J. P. Mulet, S. Mainguy, and Y. Chen, "Coherent emission of light by thermal sources," Nature (London) **416**, 61-64 (2002).

F. Marquier, K. Joulain, J.-P. Mulet, R. Carminati, and J.-J. Greffet, "Coherent spontaneous emission of light by thermal sources," Phys. Rev. B **69**, 155412 (2004).

F. Marquier, C. Arnold, M. Laroche, J.-J. Greffet, and Y. Chen, "Degree of polarization of thermal light emitted by gratings supporting surface waves," Opt. Express **16**, 5305-5313 (2008).

S. E. Han, P. Nagpal, and D. J. Norris, "Beaming thermal emission from hot metallic bull's eyes," Phys. Rev. Lett. (submitted).

P. J. Hesketh, J. N. Zemel, and B. Gebhart, "Organ pipe radiant modes of periodic micromachined silicon surfaces," Nature (London) **324**, 549-551 (1986).

A. Heinzel, V. Boerner, A. Gombert, B. Blasi, V. Wittwer, and J. Luther, "Radiation filters and emitters for the NIR based on periodically structured metal surfaces," J. Mod. Opt. **47**, 2399-2419 (2000).

R. Sprik, B. A. van Tiggelen, and A. Lagendijk, "Optical emission in periodic dielectrics," Europhys. Lett. **35**, 265-270 (1996).

P. Lodahl, A. F. van Driel, I. S. Nikolaev, A. Irman, K. Overgaag, D. Vanmaekelbergh, and W. L. Vos, "Controlling the dynamics of spontaneous emission from quantum dots by photonic crystals," Nature **430**, 654-657 (2004).

D. W. Lynch and W. R. Hunter, in *Handbook of optical constants of solids*, edited by E. D. Palik (Academic Press, Orlando, 1985).

R. B. Bird, W. E. Stewart, and E. N. Lightfoot, *Transport phenomena* (John Wiley & Sons, 1960).

J.-P. Mulet, K. Joulain, R. Carminati, and J.-J. Greffet, Appl. Phys. Lett. "Nanoscale radiative heat transfer between a small particle and a plane surface," **78**, 2931-2933 (2001).

J. J. Loomis and H. J. Maris, "Theory of heat transfer by evanescent electromagnetic waves," Phys. Rev. B **50**, 18517-18524 (1994).

J. L. Pan, "Radiative transfer over small distances from a heated metal," Opt. Lett. **25**, 369-371 (2000).

A. I. Volokitin and B. N. J. Persson, "Radiative heat transfer between nanostructures," Phys. Rev. B **63**, 205404 (2001).

M. D. Whale and E. G. Cravalho, "Modeling and performance of microscale thermophotovoltaic energy conversion devices," IEEE Trans. Energy Convers. **17**, 130-142 (2002).

A. Narayanaswamy and G. Chen, "Surface modes for near field thermophotovoltaics," Appl. Phys. Lett. **82**, 3544-3546 (2003).

M. Janowicz, D. Reddig, and M. Holthaus, "Quantum approach to electromagnetic energy transfer between two dielectric bodies," Phys. Rev. A **68**, 043823 (2003).

S. K. Lamoreaux, "The Casimir force: background, experiments, and applications," Rep. Prog. Phys. **68**, 201-236 (2005).

M. Laroche, R. Carminati, and J.-J. Greffet, "Near-field thermophotovoltaic energy conversion," J. Appl. Phys. **100**, 063704 (2006).

B. J. Lee, K. Park, and Z. M. Zhang, "Energy pathways in nanoscale thermal radiation," Appl. Phys. Lett. **91**, 153101 (2007).

S. A. Biehs, "Thermal heat radiation, near-field energy density and near-field radiative heat transfer of coated materials," Eur. Phys. J. B **58**, 423-431 (2007).

P.-O. Chapuis, S. Volz, C. Henkel, K. Joulain, and J.-J. Greffet, "Effects of spatial dispersion in near-field radiative heat transfer between two parallel metallic surfaces," Phys. Rev. B **77**, 035431 (2008).

D. R. Lide, *CRC handbook of chemistry and physics*, (CRC Press, 1978).

S.-Y. Lin, J. G. Fleming, Z. Y. Li, I. El-Kady, R. Biswas, and K. M. Ho, "Origin of absorption enhancement in a tungsten, three-dimensional photonic crystal," J. Opt. Soc. Am. B **20**, 1538-1541 (2003).

W. W. Chow and I. Waldmueller, "Active photonic lattices: Is greater than blackbody intensity possible?" J. Mod. Opt. **53**, 2371-2376 (2006).

P. Jiang, J. F. Bertone, K. S. Hwang, and V. L. Colvin, "Single-crystal colloidal multilayers of controlled thickness," Chem. Mater. **11**, 2132-2140 (1999).

B. T. Holland, C. F. Blanford, and A. Stein, "Synthesis of macroporous minerals with highly ordered three-dimensional arrays of spheroidal voids," Science **281**, 538-540 (1998).

J. E. G. J. Wijnhoven and W. L. Vos, "Preparation of photonic crystals made of air spheres in titania," Science **281**, 802 (1998).

A. Blanco, E. Chomski, S. Grabtchak, M. Ibisate, S. John, S. W. Leonard, C. López, F. Meseguer, H. Míguez, J. P. Mondia, G. A. Ozin, O. Toader, and H. M. van Driel, "Large-scale synthesis of a silicon photonic crystal with a complete three-dimensional bandgap near 1.5 micrometres," Nature **405**, 437-440 (2000).

Y. A. Vlasov, X. Z. Bo, J. C. Sturm, and D. J. Norris, "On-chip natural assembly of silicon photonic bandgap crystals," Nature **414**, 289-293 (2001).

G. von Freymann, S. John, M. Schulz-Dobrick, E. Vekris, N. Tetreault, S. Wong, V. Kitaev, and G. A. Ozin, "Tungsten inverse opals: The influence of absorption on the photonic band structure in the visible spectral region," Appl. Phys. Lett. **84**, 224-226 (2004).

N. R. Denny, S. Han, R. T. Turgeon, J. C. Lytle, D. J. Norris, and A. Stein, "Synthetic approaches toward tungsten photonic crystals for thermal emission," SPIE Proc. **6005**, 60050501 (2005).

M. Florescu, H. Lee, A. J. Stimpson, and J. Dowling, "Thermal emission and absorption of radiation in finite inverted-opal photonic crystals," Phys. Rev. A **72**, 033821 (2005).

P. M. Bell, J. B. Pendry, L. Martin-Moreno, and A. J. Ward, "A program for calculating photonic band structures and transmission coefficients of complex structures," Comput. Phys. Commun. **85**, 306 (1995).

A. L. Pokrovsky, V. Kamaev, C. Y. Li, Z. V. Vardeny, A. L. Efros, D. A. Kurdyukov, V. G. Golubev, "Theoretical and experimental studies of metal-infiltrated opals," Phys. Rev. B **71**, 165114 (2005).

J. S. King, D. P. Gaillot, E. Graugnard, and C. J. Summers, "Conformally back-filled, non-close-packed inverse-opal photonic crystals," Adv. Mater. **18**, 1063-1067 (2006).

T. W. Ebbesen, H. J. Lezec, H. F. Ghaemi, T. Thio, and P. A. Wolff, "Extraordinary optical transmission through sub-wavelength hole arrays," Nature **391**, 667-669 (1998).

H. F. Ghaemi, T. Thio, D. E. Grupp, T. W. Ebbesen, and H. J. Lezec, "Surface plasmons enhance optical transmission through subwavelength holes," Phys. Rev. B **58**, 6779-6782 (1998).

R. Biswas, C. G. Ding, I. Puscasu, M. Pralle, M. McNeal, J. Daly, A. Greenwald, and E. Johnson, "Theory of subwavelength hole arrays coupled with photonic crystals for extraordinary thermal emission," Phys. Rev. B **74**, 045107 (2006).

N. R. Denny, S. E. Han, D. J. Norris, and A. Stein, "Structural effects of thermal emission on monolithic tungsten and tungsten alloy photonic crystals," Chem. Mater. **19**, 4563-4569 (2007).

A. Polman, "Plasmonics applied," Science **322**, 868-869 (2008).

E. Ozbay, "Plasmonics: Merging photonics and electronics at nanoscale dimensions," Science **311**, 189-193 (2006).

H. J. Lezec, A. Degiron, E. Devaux, R. A. Linke, L. Martin-Moreno, F. J. García-Vidal, and T. W. Ebbesen, "Beaming light from a subwavelength aperture," Science **297**, 820-822 (2002).

L. Martín-Moreno, F. J. García-Vidal, H. J. Lezec, A. Degiron, and T. W. Ebbesen, "Theory of highly directional emission from a single subwavelength aperture surrounded by surface corrugations," Phys. Rev. Lett. **90**, 167401 (2003).

M. Laroche, C. Arnold, F. Marquier, R. Carminati, J. J. Greffet, S. Collin, N. Bardou, and J. L. Pelouard, "Highly directional radiation generated by a tungsten thermal source," Opt. Lett. **30**, 2623-2625 (2005).

Y. T. Chang, Y. H. Ye, D. C. Tzuang, Y. T. Wu, C. H. Yang, C. F. Chan, Y. W. Jiang, and S. C. Lee, "Localized surface plasmons in Al/Si structure and Ag/SiO_2/Ag emitter with different concentric metal rings," Appl. Phys. Lett. **92**, 233109 (2008).

M. U. Pralle, N. Moelders, M. P. McNeal, I. Puscasu, A. C. Greenwald, J. T. Daly, E. A. Johnson, T. George, D. S. Choi, I. El-Kady, and R. Biswas, "Photonic crystal enhanced narrow-band infrared emitters," Appl. Phys. Lett. **81**, 4685-4867 (2002).

I. Celanovic, D. Perreault, and J. Kassakian, "Resonant-cavity enhanced thermal emission," Phys. Rev. B **72**, 075127 (2005).

X. D. Yu, Y. J. Lee, R. Furstenberg, J. O. White, and P. V. Braun, "Filling fraction dependent properties of inverse opal metallic photonic crystals," Adv. Mater. **19**, 1689-1692 (2007).

H. Caglayan, I. Bulu, and E. Ozbay, "Extraordinary grating-coupled microwave transmission through a subwavelength annular aperture," Opt. Express **13**, 1666-1671 (2005).

N. Dahan, A. Niv, G. Biener, Y. Gorodetski, V. Kleiner, and E. Hasman, "Enhanced coherency of thermal emission: Beyond the limitation imposed by delocalized surface waves," Phys. Rev. B **76**, 045427 (2007).

N. Dahan, A. Niv, G. Biener, Y. Gorodetski, V. Kleiner, and E. Hasman, "Extraordinary coherent thermal emission from SiC due to coupled resonant cavities," J. Heat Transfer, **130**, 112401 (2008).

G. Biener, N. Dahan, A. Niv, V. Kleiner, and E. Hasman, "Highly coherent thermal emission obtained by plasmonic bandgap structures," Appl. Phys. Lett. **92**, 081913 (2008).

A. P. Miiler and A. Cezairliyan, "Thermal expansion of tungsten in the range 15003600 K by a transient interferometric technique," Int. J. Thermophys. **11**, 619-628 (1990).

L. N. Aksyutov and A. K. Pavlyukov, "Temperature dependence of the optical constants of tungsten and gold," Zh. Prikl. Spektrosk. **26**, 914-918 (1977).

T. Erdogan and D. G. Hall, "Circularly symmetric distributed feedback semiconductor laser: An analysis," J. Appl. Phys. **68**, 1435-1444 (1990).

R. H. Jordan and D. G. Hall, "Free-space azimuthal paraxial wave equation: the azimuthal Bessel-Gauss beam solution," Opt. Lett. **19**, 427-429 (1994).

J. Durnin, J. J. Miceli, Jr, and J. H. Eberly, "Diffraction-free beams," Phys. Rev. Lett. **58**, 1499-1501 (1987).

List of Publications

1. S. E. Han, A. Stein, and D. J. Norris, "Tailoring self-assembled metallic photonic crystals for modified thermal emission," Phys. Rev. Lett. **99**, 053906 (2007).

   [Selected for Virtual Journal of Nanoscale Science & Technology **16**, Issue 7, August 13 (2007)]

2. N. R. Denny, S. E. Han, D. J. Norris, and A. Stein, "Effects of thermal processes on the structure of monolithic tungsten and tungsten alloy photonic crystals," Chem. Mater. **19**, 4563 (2007).

3. S. E. Han and D. J. Norris, "Control of thermal emission by selective heating of periodic structures," Phys. Rev. Lett. (submitted).

4. P. Nagpal, S. E. Han, A. Stein, and D. J. Norris, "Efficient low-temperature thermophotovoltaic emitters from metallic photonic crystals," Nano Lett. **8**, 3238 (2008).

5. S. E. Han, P. Nagpal, and D. J. Norris, "Beaming thermal emission from hot metallic bull's eyes," Phys. Rev. Lett. (submitted).

6. D. J. Norris, S. E. Han, P. Nagpal, and A. Bahn, "Creation of light and/or surface plasmons with heated metallic films," U.S. Patent (submitted).

7. H. Wei, D. F. Underwood, D. A. Blank, S. E. Han, and D. J. Norris, "The role of

stress in the time-dependent optical response of silicon photonic band gap crystals," Appl. Phys. Lett., (submitted).

8. Y. Jun, S. E. Han, S. Han, and D. J. Norris, "Crack-free close-packed and non-close-packed inverse opal films from preheated silica spheres," Adv. Funct. Mater., (to be submitted).

9. S. E. Han, "Theory of thermal emission from periodic structures," Phys. Rev. B, (to be submitted).